EFFECT OF TEMPERATURE ON CREEP PROPERTIES OF ORGANIC-RICH SHALES

A Thesis

by

PRASHANT SHARMA

Submitted to the Office of Graduate and Professional Studies of
Texas A&M University
in partial fulfillment of the requirements for the degree of

MASTER OF SCIENCE

Chair of Committee,	Sara Abedi
Committee Members,	Eduardo Gildin
	Arash Noshadravan
Head of Department,	Alfred D. Hill

May 2017

Major Subject: Petroleum Engineering

ABSTRACT

Understanding the creep properties of gas shales at elevated temperatures is critical for accurately predicting reservoir performance and assessing the effect of viscous behavior on closure rate, production rate, and conductivity loss. In order to better understand creep properties at in-situ conditions, a quantitative relationship between temperature, mechanical properties, and complex chemo-physical mechanisms that causes thermal alteration needs to be obtained. In this study, elastic, strength, and creep properties of organic-rich shales are investigated by a combination of nanoindentation, energy dispersive x-ray spectroscopy, and micromechanical modeling over a range of temperatures (23-350^{o}C). In particular, elastic and strength properties are extracted through nanoindentation between temperatures of 23-350^{o}C and creep properties are measured similarly between temperatures of 23-300^{o}C. Within the allotted temperature range, the elastic and strength properties of the porous clay/kerogen phase remains unchanged due to the highly mature organic matter and low water content present within the matrix. A similar behavior is noticed in the creep modulus from temperatures 23-200^{o}C where it remains relatively unchanged and shows an isotropic characteristic. However, the creep modulus of the clay phase increases at 300^{o}C in both parallel and perpendicular directions to the bedding plane. In addition, the indentation modulus and hardness increase at 300^{o}C are a result of the enhancement of particle sliding and compaction of clay particles due to the transformation of organic matter to hydrocarbons. Analysis of the creep data obtained in this experimental effort sheds light on the dictating role of organic

matter and porosity on creep properties of organic-rich shales and emphasizes the pivotal role of organic matter in the time-dependent response. Specifically, the isotropic increase also suggests that the isotropic phases, which are organic matter and porosity, play an important role in driving creep properties in shales. Evaluation of the probability density functions (PDF) of the contact creep modulus suggests that a bimodal distribution occurs between temperatures of 23-200^{o}C which corresponds to two different modes: the clay/kerogen mode (mode I) and the porous clay mode (mode II). However, at 300^{o}C, a unimodal trend exists that aligns closely with mode II, indicating that it is only linked to the porous clay phase rather than the clay/kerogen mode.

DEDICATION

This thesis is dedicated to my parents, Praveen and Neeta, for their unconditional love and support. To my sister and brother-in-law, Priyanka and Nikhil, for pushing me to reach higher limits. To my baby nephew, Yash, for putting a smile on my face during the toughest of times; your energy carries healing powers that cannot be measured. To my aunts, uncles, cousins, and friends near and afar for the continuous positivity and entertainment; without you, my journey at Texas A&M would not have been the same. Finally, this thesis is dedicated to myself for being strong and courageous when faced with difficult circumstances in both my personal and professional life.

ACKNOWLEDGEMENTS

I would like to thank my committee chair, Dr. Sara Abedi, for her guidance and support throughout the course of this research and for providing the financial support for this experimental work. I would also like to thank my committee members, Dr. Noshadravan and Dr. Gildin, for evaluating my thesis and being a part of my master's defense.

Thanks to Dr. Maggard for giving me the chance to be a Teaching Assistant for PETE 665: Reservoir Engineering for two semesters; your support helped me both academically and financially and I thank you very much for believing in me.

Thanks to the Petroleum Engineering department for admitting me into the program and exposing me to the various facets of our industry. A special thanks to Dr. Akkutlu for making learning fun and exciting and for continually giving me useful feedback throughout my academic career at Texas A&M.

I would like to thank Dr. Wilson Serem, for his technical support on the Nanoindenter and for his considerable feedback in my experimental efforts. I would also like to thank to Dr. Andrew Mott for his assistance on the Electron Microprobe and sample preparations.

Thanks to my best friends Shawn Muttreja, Laura Pelaez-Soni, Purnik Amin, Sravya Kandulapati, and Nisha Choksi-Remus for their patience, faith, and encouragement in helping me finish my master's degree.

NOMENCLATURE

$\dot{A}$	Angstroms
A_c	Projected Contact Area
A_1	Constant 1
A_2	Constant 2
A_u	Projected Contact radius
β	Shales relaxation/retardation constant
B	Empirical Constant/Compliance Constant
BIC	Bayesian Information Criteria
C	Celsius
C_i	Contact Creep Modulus
C_u	Uniaxial Creep Modulus
C^{hom}	Homogenized Stiffness Tensor
EDX	Energy Dispersive X-ray Spectroscopy
ε	Geometric Constant
E	Elastic young's modulus of the material (same as E_o)
ε^c	Creep Strain
E_o	Elastic young's modulus of the material
E_1	Magnitude of time-dependent penetration
E_i	Indentation Elastic Modulus (diamond)
E_r	Reduced Modulus

f_k	Overall Fraction of Kerogen
f_c	Overall Fraction of Clay
G	Shear Modulus
h	Displacement
h_c	Contact height
h_{max}	Maximum height
H	Indentation Hardness
$\dot{h}(t)$	Rate of Penetration of Tip during Creep Phase
$\Delta h(t)$	Penetration depth After Creep Phase
J(t)	Contact Creep Compliance
k	Material constant
K	Bulk Modulus
$\dot{L}(t)$	Contact Creep Compliance Rate
M_{eq}/g	Cation Exchange Capacity (milli-equivalents per gram)
m^2/g	Specific surface area of 1 gram of clay in m^2
M	Indentation Modulus
M_o	Indentation Modulus
n	Material constant/Power-law Exponent
η_c	Volume Fraction of Clay
η_k	Volume Fraction of Kerogen
p	Material constant
P	Load

ϕ	Porosity (Level II)
ϕ_{k+c}	Porosity of Kerogen and Clay
φ	Porosity (Level I)
P_{max}	Average Pressure Applied onto probe
ρ_{TOC}	Density of TOC
ρ_{BULK}	Bulk Density of Sample
S	Contact Stiffness
SEM	Scanning Electron Microscope
σ	Stress
SSA	Specific Surface Area
TOC	Total Organic Content
τ_i	Characteristic Time from Indentation Testing
τ_u	Characteristic Time from Uniaxial Testing
υ	Poisson's Ratio (material)
υ_i	Poisson's Ratio (diamond)
XRD	X-ray Diffraction Spectroscopy

CONTRIBUTORS AND FUNDING SOURCES

Contributors

This work was supported by a thesis committee consisting of Professors Sara Abedi and Eduardo Gildin of the Department of Petroleum Engineering and Professor Arash Noshadravan of the Department of Civil Engineering.

All work for the thesis was completed by the student, in collaboration with Professor Sara Abedi of the Department of Petroleum Engineering.

Funding Sources

This work was made possible in part by the Harold Vance Department of Petroleum Engineering, Texas A&M University.

TABLE OF CONTENTS

Page

LIST OF FIGURES

Page

LIST OF TABLES

Page

CHAPTER I

INTRODUCTION

This chapter is a summary of the research project. The chapter begins with a brief overview of shales and their importance to petroleum engineers as well as the benefits, challenges, and possibilities of studying creep in shales. Next, the objectives of this research are summarized as well as the scientific and industrial benefits of this work. Finally, an outline of the thesis is provided including the main contents covered of each chapter.

1.1 Shales in petroleum engineering

Naturally occurring rocks are composed of one mineral (homogeneous) or several minerals (heterogeneous). Traditionally, rocks are classified into three categories: sedimentary, metamorphic, and igneous (Blatt et. al., 1996). Sedimentary rocks are of highest importance to petroleum engineers. Typically, conventional oil and gas is produced from formations in which there is adequate reservoir pressure and flow, resulting in a cost effective drilling program. Unconventional oil and gas, however, refers to reservoirs with low permeability and porosity where the hydrocarbons do not flow as easily as those in conventional reservoirs. As defined by Holditch (2003), "An unconventional reservoir is one that cannot be produced at economic flow rates without assistance from massive stimulation treatments or special recovery processes and technologies. Typical unconventional reservoirs are tight gas sands, coalbed methane, heavy oil and gas shales." To maximize the recovery of the residual hydrocarbons,

secondary (water drive) and tertiary (liquid petroleum gas flooding, carbon dioxide flooding, or surfactant flooding) recovery methods are needed (Dake, 1978). Shale is a sedimentary rock covering 75% of the earth's crust. As a result, production from shales has continued to increase over the last several years due to an increase in the world's energy demands and technological developments in economically extracting hydrocarbons from the tight pore spaces of the rock matrix.

1.2 Creep of shales

Shales have an extremely low permeability which makes enhanced recovery an essential process in the production of hydrocarbons. Many factors cause the loss of fracture conductivity, which results in low recovery and inefficient production. One of the main factors affecting fracture conductivity is the creep of the rock. Creep is the time-dependent deformation of the material under constant stress (Findley, 1989). Failure to characterize the time-dependent behavior of these source rocks may result in errors in estimating reservoir performance during depletion.

1.3 The challenges of measuring creep in shales

Organic-rich shales are extremely heterogeneous sedimentary rocks composed mainly of clay particles, organic-matter, silt-size inclusions such as quartz and feldspar, and trace amounts of other minerals. Furthermore, shales contain different types of clays, varying levels of maturity of organic-matter, and have different porosity values, all of which are dependent on the depositional environment and depth the rock was extracted

from; the mechanical response of shales also vary based on the formation temperature and the formation temperature and largely affects the creep response of shales. Lastly, measuring creep at the macroscopic level using experimental methods (compression tests) can take large amounts of time and measurements at this level do not capture the effect of heterogeneity (the contribution of each individual constituent) on the creep properties of shales. These are a few factors that make measuring and obtaining creep properties expensive and a challenge for researchers to understand the controlling factors of creep in shales.

1.4 The possibilities of creep measurements using nanoindentation

Nanoindentation has been proven as a well suited technique in measuring the mechanical properties of organic-rich shales (Abedi et al., 2015; Slim et al., 2017). These properties include indentation modulus, hardness, and, more recently, creep. Moreover, recent developments have enabled the ability to perform instrumented nanoindentation at elevated temperatures with the use of temperature control stages. This serves as a pathway for determining the behavior of shales at in-situ conditions and the factors that control it.

1.5 Scope of the work and its novelty

Numerous experimental and theoretical studies have dealt with obtaining creep properties of organic-rich source rocks under ambient conditions (Sone and Zoback, 2013; Li and Ghassemi, 2012; Rassouli and Zoback 2016). However, these conditions do not capture the in-situ behavior of many source rocks. Moreover, recent progress in thermal

recovery of shale gas requires an enhanced understanding of reservoir properties at elevated temperatures. In this regard, a quantitative relation between temperature, mechanical properties, and complex chemo-physical mechanisms that cause the thermal alteration needs to be obtained.

There are three main objectives of this research:

1. To determine whether high temperatures affect the mechanical response of shales; these mechanical properties include elasticity (indentation modulus), strength (indentation hardness), and creep. Evaluation of the results is performed using a chemo-mechanical assessment validated by Abedi et al., (2015).
2. To determine the main factors that influence the creep response of shales.
3. To use an existing logarithmic model to obtain quantitative contact creep modulus values from results obtained through nanoindentation experiments to analyze the creep behavior of the porous clay/kerogen phase at higher temperatures.

There are three scientific and industrial benefits to this research:

1. Short indentation tests can be performed to obtain the long-term creep properties of organic-rich shales at high temperatures.
2. An understanding of the mechanisms that drive creep properties in organic-rich shales.

3. A well-suited logarithmic model that assesses the creep behavior of the porous clay/kerogen phase at high temperatures.

1.6 Outline of this thesis

There are four main parts to this thesis. The first part (chapter II) includes a literature review of the theoretical and experimental studies performed on creep. The second part (chapter III) provides information on the sample used in this study including sample preparation procedures and various ways to measure porosity. Furthermore, explanation of thermogravimetry settings and the equipment used, particularly nanoindentation and Energy Dispersive X-ray Spectroscopy (EDX), in order to complete the study are included within. The chapter ends with an explanation of the coupling and statistical based clustering techniques used to analyze the experimental results. The third part (chapter IV) includes the final results and is supported with discussions. The final phase (chapter V) includes the final conclusions, where the main findings and limitations from this study are summarized.

CHAPTER II

LITERATURE REVIEW

This chapter begins with a discussion of the multi-scale structure thought model used to differentiate between the various scales of shales and a detailed summary of the types of clays present in shales including the major differences between each of them. Next, a review of the theory of creep is included, literature review of the types of experiments completed and results obtained at both the macroscale and the microscale levels are provided, and miscellaneous experimental methods used to measure the mechanical (time-independent) properties of shales are summarized. Finally, the chapter ends with a list of temperatures for three separate formations. This chapter provides the preliminary background needed to understand the concept of creep and the applications of it.

2.1 Multi-scale structure thought model

Shales are heterogeneous multiphase composite materials and are composed of porous clay and various silt-size inclusions. When performing experiments at the macroscale, researchers have used triaxial testing and acoustic testing to determine the strength properties of shales. At the microscale level, however, the heterogeneity of shales can be explained through a revised multi-scale structure thought model proposed by Abedi et al., (2016). This thought model is useful in determining the mechanical properties at the different length scales. These levels are as follows: elementary particles (Level 0), porous organic/clay composite (Level 1), and porous solid-silt inclusion composite (Level 2).

Through the use of nanoindentation, a high-resolution technique, the mechanical properties can be measured at the level 1 scale. The next section discusses the three-level thought-model (**Fig. 1**) for shales in greater detail.

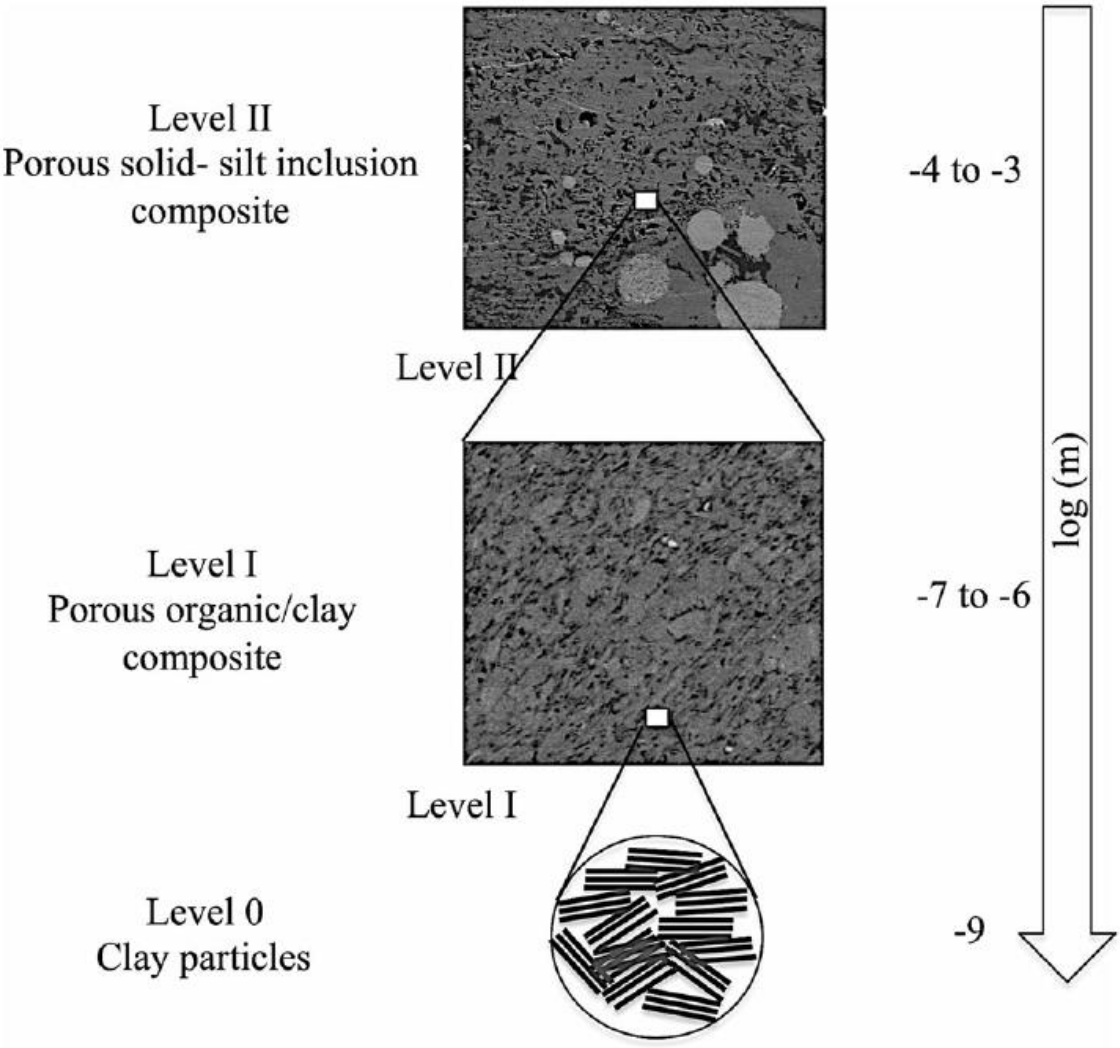

Figure 1 – Multiscale thought model proposed by Abedi et al., (2016) where Level 0 corresponds to the clay minerals (10^{-9} to 10^{-8}), Level 1 corresponds to the porous organic/clay composite (10^{-7} to 10^{-6}), and Level II corresponds to the porous solid-silt inclusion composite (10^{-4} to 10^{-3}) (Abedi, et al., 2015).

2.1.1 Level 0: Elementary clay particles

Level 0 is one of the three length scales proposed by Abedi et al., (2016). This level is composed of the clay particle phase in shale, and it is considered the fundamental scale of clay mineralogy. The level is observed at the nanometer scale with a length scale on the order of 10^{-9} to 10^{-8}m. Images of the clay phase at this scale are obtained through Scanning Electron Microscopy or Transmission Electron Microscopes (TEM) and are shown in **Fig. 2A-C**. Clay minerals have an aspect ratio of 1/20. **Fig. 2A** is an image taken under the TEM and shows the nanostructure of smectite fabric. Shale is transversely isotropic and as can be seen from **Fig. 2B**, can be visually interpreted by the bedding plane visible under an SEM; the clay particles and pores align in a single direction, giving it an obvious bedding plane. **Fig. 2C** shows the platy clay structure at level 0.

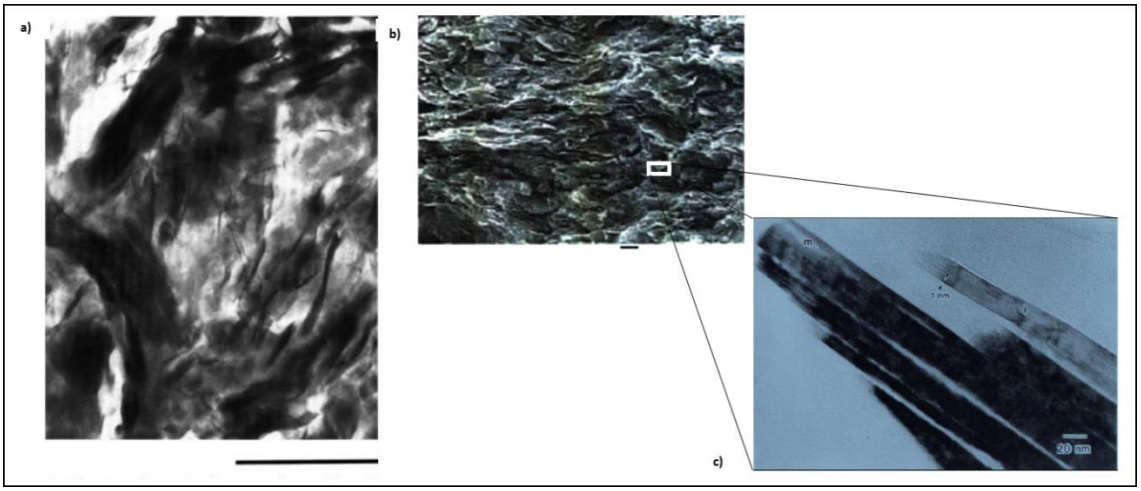

Figure 2 – A) TEM image of smectite fabric; scale bar = 1µm (Byrant, et al., 1990). B) Level I image obtained under a SEM (Ortega, et al., 2009) and C) Level 0 image obtained under a TEM (Deirieh, et al., 2011).

2.1.2 Level I: Porous organic/clay composite

Level I is the second length scale described in the think-model and has a scale length of 10^{-7} to 10^{-6}m. This level, generally referred to as the porous clay composite, is a combination of the fundamental scale of clay (Level 0) and the porosity of the shale sample. It is proposed that the mechanical behavior of shales is a function of the packing of clay conglomerates which is of particular importance in this study of shale's mechanical properties since it is the driver of macroscopic properties. Through nanoindentation, an experimental technique commonly used to study the mechanical properties of materials at the micro scale, the probe indents the shale sample at this particular length scale and provides the reduced modulus and hardness properties of the various phases present. The stiffness value measured at this particular level is one order of magnitude smaller than the clay mineral due to the deformation of the pore space. In addition, the measured values prove that a small amount of anisotropy exists at this level. An example of the shale surface at Level I is shown in **Fig. 2B**. At this particular level, the direction of bedding place (X1 or X3) are typically visible in most shale samples.

2.1.3 Level II: Textured clay layer composite

Level II is representative of the macroscopic length scale in that it includes the various constituents present in the shale matrix, specifically, clays and silt-size grains (mainly quartz and feldspar inclusions). The length scale of level II is 10^{-4} to 10^{-3} m. The difference between level I and II, besides length scale, is that the shale fabric is more

obvious at a smaller magnification, making the sample appear more homogenous at this level.

Fig. 3 is an example of an elemental overlay showing the different minerals present in Haynesville shale obtained perpendicular to the bedding plane using a Cameca Electron Microprobe. Elements such as dolomite, pyrite, quartz, feldspar, apatite, carbonate, and kerogen are present in the sample. Clay, kerogen, and porosity are interspersed in between these elements where clay serves as the binding-phase of the whole sample.

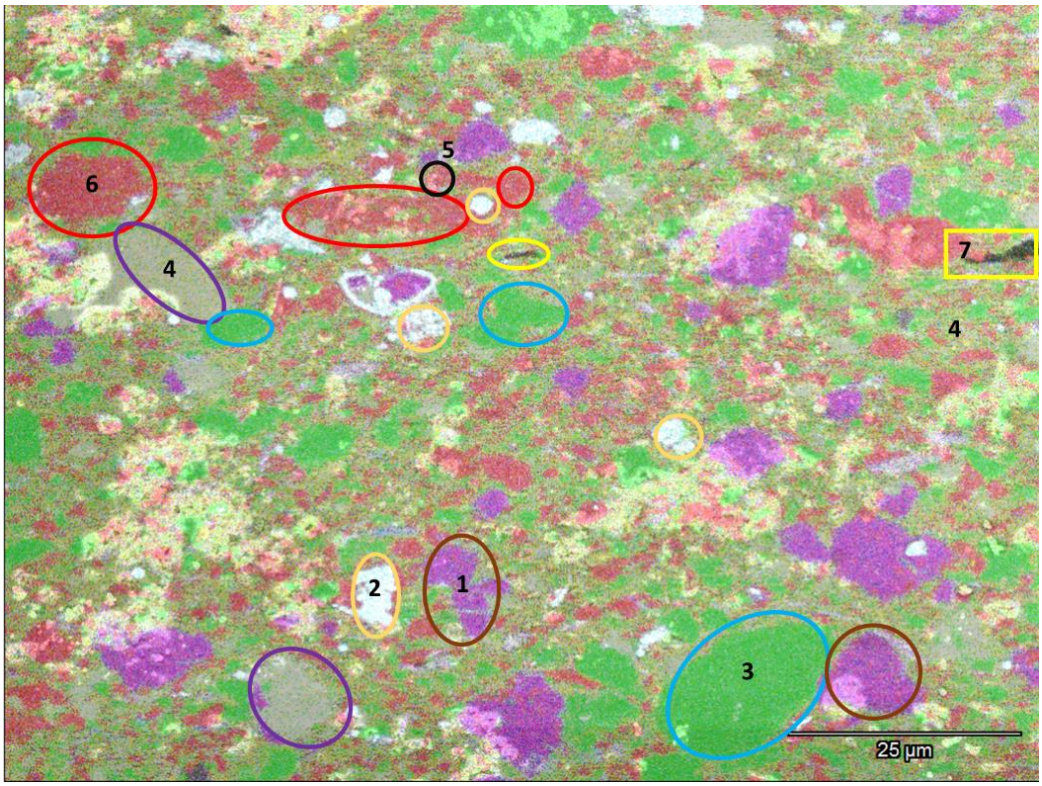

Figure 3 – Backscattered Electron (BSE) image of Haynesville shale (X1-direction, 23C) taken on a Cameca SX Five Electron Microprobe; 1 = Dolomite (Mg+Ca), 2 = Pyrite (Fe+S), 3 = Quartz (Si), 4 = Feldspar (Si+Al+Na), 5 = Apatite (P+Ca), 6 = Carbonate (Ca), and 7 = Kerogen.

2.2 Description of clays present within shales

In order to understand the mechanical properties of clays in shales, it is necessary to study the chemical structure of clays and differentiate between the types of clay.

Clays are phyllosilicates that form sheet structures composed of a tetrahedral sheet of silicon and oxygen and an octahedral sheet of aluminum, oxygen, and hydroxyl atoms (Bassiouni, 1994). Each type of clay mineral is determined by the arrangement of these layers as well as the accessory cations that lie within the platelet structure.

The tetrahedral sheet (or silica sheet) is composed of tetrahedrons connected by oxygen atoms. There are four oxygen atoms and one silicon atom in each molecule. Oxygen (O^{-2}) is an anion, which means that the oxygen atom has a "negative" charge; Silicon (Si^{+4}) is a cation, meaning that silicon atoms have a "positive" charge. **Figs. 4 and 5** show a diagram of the structure of the four oxygen atoms and silicon atom as well as the connection of each molecule by oxygen atoms that is more commonly referred to as the tetrahedral sheet. An excess of negative charge in the structure exists because of the eight oxygen anions and four silicon cations. For simplicity, a trapezoid is used to represent the tetrahedral sheet, as shown in **Fig. 6**. The oxygen atom at the base is connected to the next tetrahedron and two tetrahedrons can share only one oxygen atom.

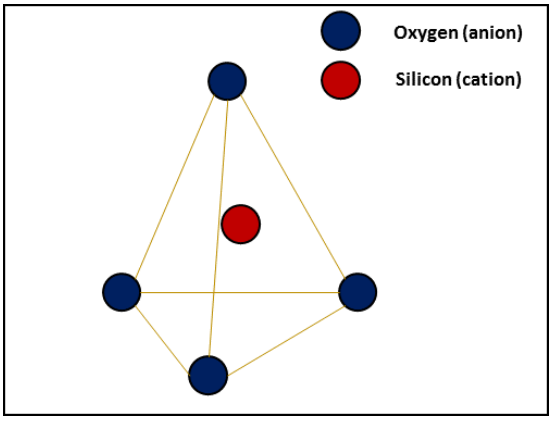

Figure 4 – Schematic of a single tetrahedral sheet composed of four oxygen atoms (anions) and one silicon atom (cation).

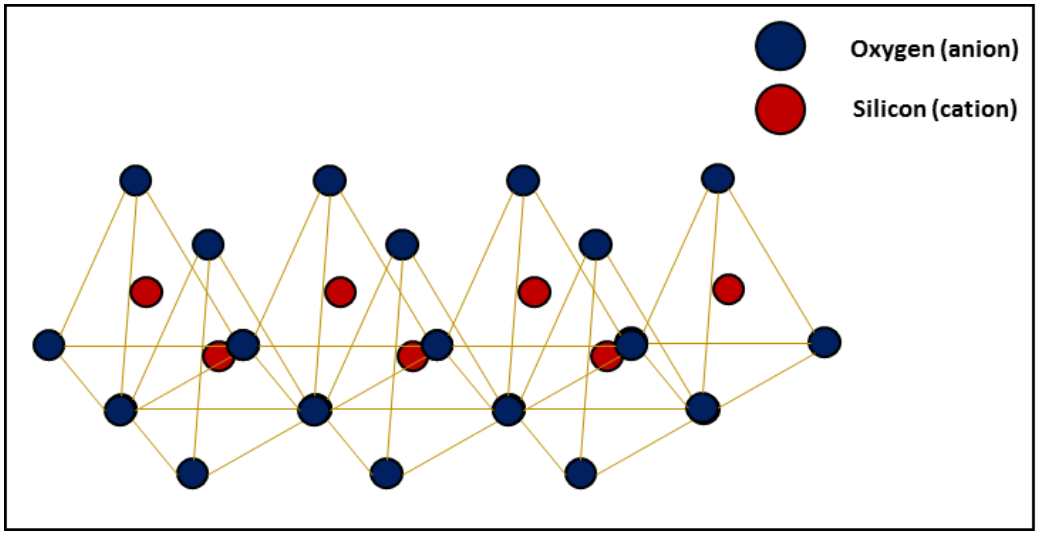

Figure 5 – Schematic of a tetrahedral sheet connected by oxygen atoms.

Figure 6 – A simplified diagram of a tetrahedral sheet.

The octahedral sheet (or aluminum sheet) is composed of octahedrons connected by oxygen, hydroxyl, and aluminum atoms. There are six oxygen atoms, two hydroxyl atoms, and one aluminum (or magnesium) atom in each molecule, giving the structure eight different faces. While oxygen has a "negative" charge and is referenced as an anion, aluminum is a cation and is more appropriately called tetravalent aluminum due to the number of valence electrons (Al^{+3}). **Figs 7 and 8** show the structure that makes up the octahedral sheet in a clay platelet. Octahedral sheets also have a net negative charge due to the six oxygen anions, two hydroxyl anions, and three aluminum cations. Similar to tetrahedral sheets, octahedral sheets are drawn as a rectangle for quick illustration, as shown in **Fig. 9**.

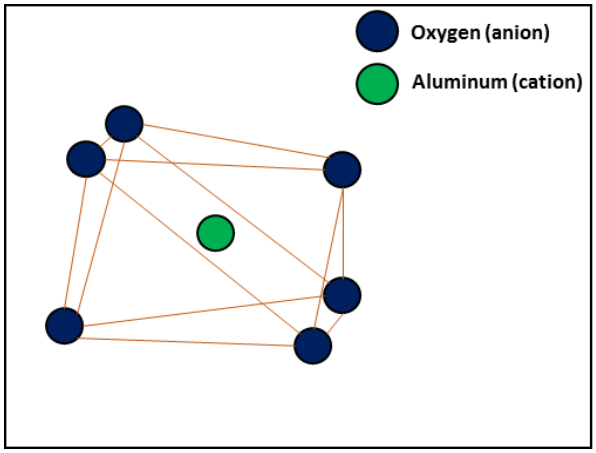

Figure 7 – Schematic of a single octahedral sheet composed of six oxygen atoms (anions), two hydroxyl atoms (anions), and one silicon atom (cation).

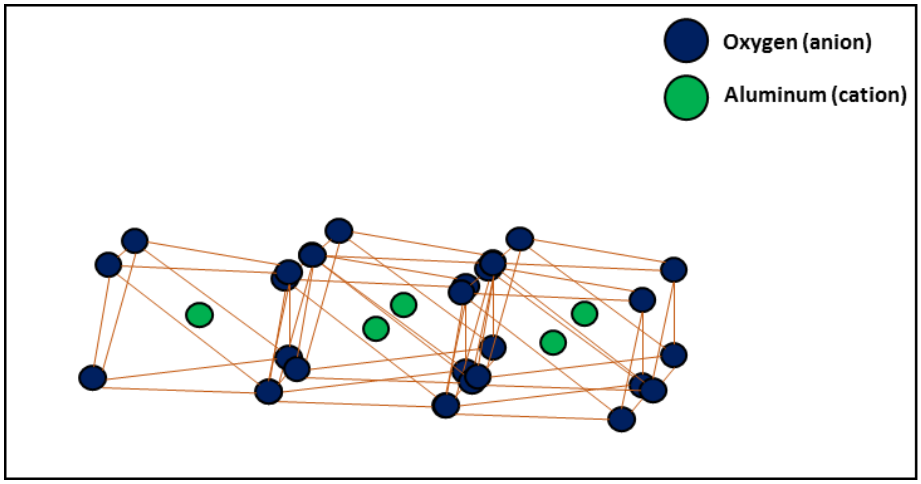

Figure 8 – Schematic of an octahedral sheet connected by oxygen atoms.

Figure 9 – A simplified diagram of an octahedral sheet.

The stacking of the clay layers determine the type of clay whereas the adsorbed (also called interlayer or accessory) cations and water determine the strength of the clay platelets.

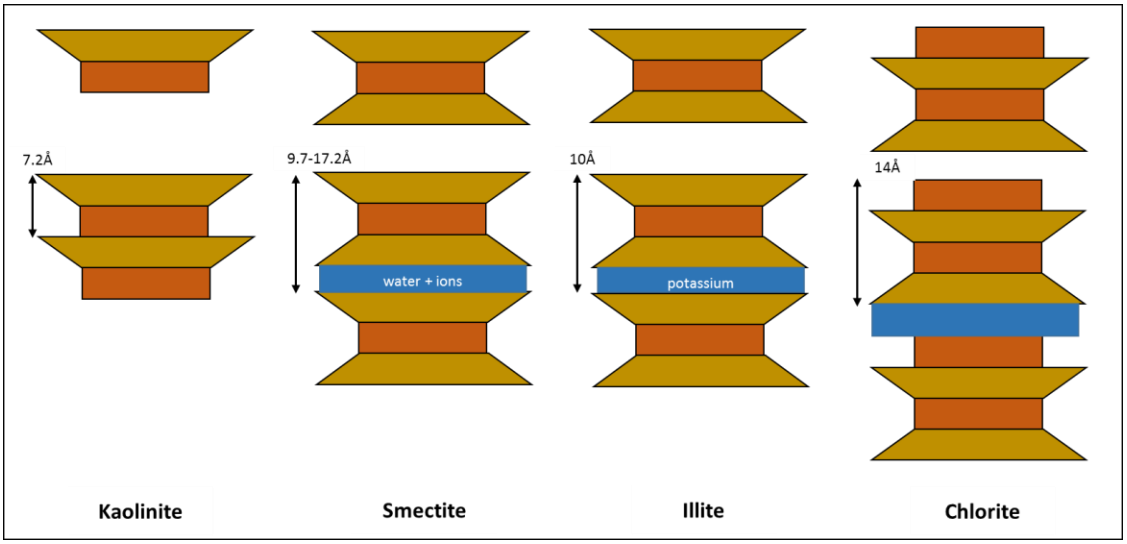

Figure 10 – Structural diagram of the four major clay groups: kaolinite, smectite, illite, and chlorite.

2.2.1 Clay minerals

In general, there are four major classes of clays: kaolinites, smectites, illites, and chlorites (**Fig. 10)**. Each class of clay is differentiated by the arrangement of structure, the interlayer cation present, and the cation exchange capacity. A discussion of the similarities and differences between each class of clay is provided next.

2.2.1.1 Kaolinite Minerals

Kaolinites are a 1:1 clay type mineral. The structure is composed of an alternating tetrahedral and octahedral layer as shown in **Fig. 10** (Mitchell, et al., 2005). Kaolinites have a strong interlayer strength due to Van Der Wall forces and hydrogen bonds (Bear, 1964). In particular, kaolinites have an outer hydroxyl group that is located on the octahedral sheet that is not in contact with the tetrahedral sheet and an inner hydroxyl group that is located in between the tetrahedral and octahedral sheets. As a result, most

sorption takes place on the open surface of the platelet. Kaolinite does not expand or compact and has very little isomorphous substitution, which is the process of one type of cation being replaced with another cation with the same or different valence (Rengasamy, 1975). Consequently, kaolinites have a low cation exchange capacity, averaging at around 0.03 meq/g (Mitchell et al., 2005). An image of kaolinite obtained under a scanning electron microscope is shown in **Fig. 11**. Kaolinites have a lateral dimension of 0.1-4µm and a thickness of 0.05-2µm (Mitchell et al., 2005). Common examples include kaolinite, nacrite, dickite, anauxite, and halloysite (higher water content), and are polymorphs. The basal spacing of kaolinites are approximately 7.2 Å (Mitchell et al., 2005).

Figure 11 – Intact kaolinite in a pore system obtained under a Scanning Electron Microscope (Hayatdavoudi, et al., 1996).

2.2.1.2 Smectites

Smectites are a 2:1 type mineral. This means that the structure of smectite includes two tetrahedral sheets on either side of an octahedral sheet. Other than the structural

differences between kaolinite and smectite, the capacity for smectites to absorb and store water in the basal layer is significantly greater due to weak van der walls forces and is typically selected for studies where clays with high sensitivity to temperatures and pressures are needed. When smectite is submerge in water, the water molecules cause an increase in the hydration energy which overcomes the attraction force between the silica and alumina layers. The basal spacing, as shown in **Fig. 10**, is the height of one unit layer and ranges between 9.7 and 17.2Å depending on the amount of interlayer water present. The thickness of a single layer of water molecule is approximately 2.9Å (Bassiouni, 1994). The most common type of smectite is montmorillonite and the width and thickness of a montmorillonite clay sheet is 1-2μm and 10Å, respectively. Other types of smectites include pyrophyllite, sauconite, saponite, and stevensite. **Fig. 12** shows the structure of bentonite clay under a scanning electron microscope.

The structure of smectite contains aluminum and silicon cations and undergoes extensive isomorphous substitution. The aluminum cations present in the octahedral sheet have a tendency to be replaced by other cations, such as magnesium, iron, zinc, or lithium. The silicon cations present in the octahedral sheet tend to be replaced by trivalent cations.

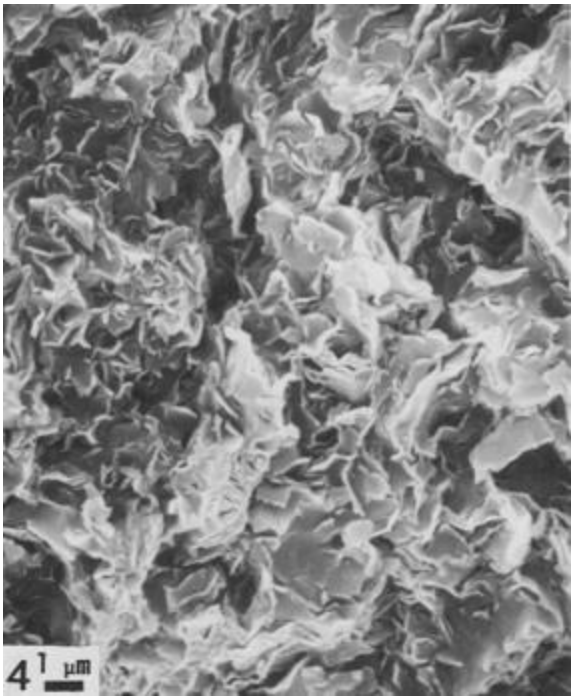

Figure 12 – Intact Na-montmorillonite in a pore system obtained under a Scanning Electron Microscope (Keller et al., 1986).

2.2.1.3 Illites

Like smectites, illites are a 2:1 type mineral. However, unlike smectites, illites do not have interlayer swelling due to the strong bond provided by the potassium ions and contain only potassium as the interlayer cation. The unit layer of illite is typically about 10Å and remains constant in spite of the presence of polar liquids. The structure of illite is similar to that of hydrous mica and therefore the two terms are used interchangeably. However, differences between the two minerals should be noted. First, more aluminum cations replace the silicon cations in hydra mica than illite during isomorphous substitution. Second, illite plates are randomly stacked. Third, Potassium content in illite is lower than in micas. Lastly, the particle size of illite is smaller than those in micas

(Mitchell et al., 2005). During cation exchange, the potassium ions present on the surface of the platelets can be replaced with other cations; however, the potassium ions between the layers are fixed and cannot be replaced. During isomorphous substitution, the silicon in the tetrahedral sheets are replaced by aluminum whereas the aluminum in the octahedral sheets are replaced by magnesium or iron. The already present potassium helps balance the overall charge deficiency within the platelet. In general, illites, like montmorillonite, have a high cation exchange capacity, averaging at about 0.20 meq/g (Bassiouni, 1994). Examples of illite clay include hydra-micas, phengite, and glauconite. Illites have a width of 0.1-several μm and a thickness of approximately 30Å. **Fig. 13** shows an image of illite plates obtained under the scanning electron microscope.

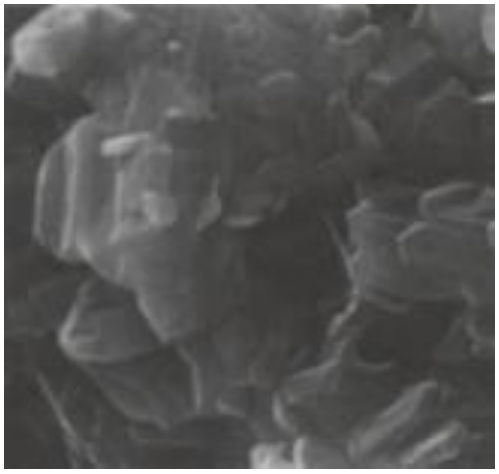

Figure 13 – Intact illite in a pore system obtained under a Scanning Electron Microscope; image dimension: 7.5μm (Mitchell, 1993, taken from Tovey 1971).

2.2.1.4 Chlorites

Chlorites are very similar in structure to smectites and illites. While smectites carry water and ions and illites carry potassium ions between their interlayers, chlorites have an additional octahedral layer in between each clay platelet. Consequently, chlorites are also a 2:1 clay type minerals with a basal spacing of 14Å. The sheet in between the two clay platelets is a trioctahedral sheet composed of magnesium cations. The sheet in between the tetrahedral layers is a decahedral sheet.

2.2.2 Specific surface area

Clays control the behavior of the soil as they are present in almost all soils and contain the largest surface area fraction compared to other minerals in the soil. As a result, the specific surface area (SSA) of clays is another factor in determining the amount of absorption of organic matter, nutrients, and pollutants that can take place within the structure and is crucial to quantify. Through the use of Atomic Force Microscopy (AFM) and other methods, researchers were able to determine the specific surface area of illite and montmorillonite (Macht, 2011). Mitchell noted that the specific surface area of kaolinite falls within 10 – 20 m^2/g while illite and smectite have a specific surface area of 65 – 100 m^2/g and 50-120 m^2/g, respectively (Mitchell et al., 2005). Macht et al. noted the specific surface area of illite and montmorillonite to be approximately 83 m^2/g and 346 m^2/g.

2.3 Introduction and theory of creep

The highly heterogeneous and transversely anisotropic nature of shales as well as their tight packing makes understanding and characterizing their multi-scale behavior very challenging. Applying the material science paradigm to study the microstructure of shales can provide valuable information about their physical properties and behaviors. In the field of petroleum engineering, hydrocarbon recovery is limited by the low permeability and porosity of source rocks. While hydraulic fracturing can help increase the amount of hydrocarbons recovered from the formation, several factors including the loss of fracture conductivity due to proppant embedment (**Fig. 14**) can result in lower recovery and inefficient production. One of the major contributors to the drop in fracture conductivity is the creep of the rock. This time-dependent (creep) behavior impacts the transport properties within the formation during production; as a result, observing the behavior of these rocks may result in accurately estimating reservoir performance during depletion.

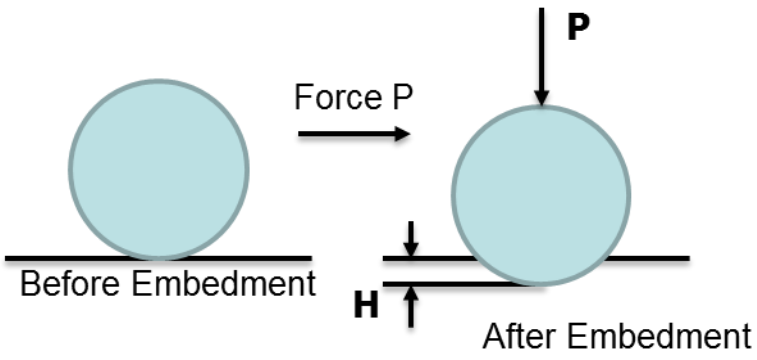

Figure 14 – Elastic deformation after proppant embedment (Revised from Guo, 2012).

With the continuous development of technology and the introduction and uses of complex materials, an understanding of the relationship between stresses and strains is critical for proper design and functionality. An elastic, plastic, or viscoelastic behavior is observed depending on the type of material under study. An elastic strain is observed in most materials under a small constant load (stress), meaning that upon removal of the load, the material reverses with no permanent deformation. In materials where plastic behavior is seen, the material shows signs of elastic behavior at the onset of a loading but quickly deforms when the load exceeds the elastic limit. Viscoelastic behavior, which is a combination of elasticity and viscosity, is different from elastic and plastic behavior in that it is dependent on three parameters: stress, strain, and time. Viscoelastic behavior shows a declining strain when a constant stress is applied. The time parameter is included to quantify the viscoelastic behavior because such materials show a different strain behavior based on the loading rate used. Examples of viscoelastic materials include plastics, wood, and concrete. The study of the time-dependent viscoelastic behavior of materials is classified as "creep". By definition, creep is the deformation of a material under constant load or stress (Findley et al., 1976). The behavior of creep is divided into three separate stages: primary, secondary, and tertiary (**Fig. 15**). Primary creep is the decrease in strain over constant load, secondary creep is the constant strain under constant load and is achieved after primary creep, and tertiary creep is the exponential increase in strain with constant load and results in a fracture. **Fig. 16** illustrates the behavior of various materials during and after the loading period. Linearly viscoelastic simply means that the stress is proportional to the strain. Shales are considered to be linearly viscoelastic.

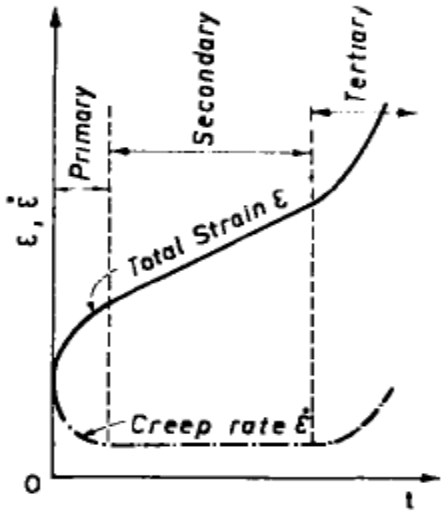

Figure 15 – The three stages of creep observed in materials (Findley et al., 1976).

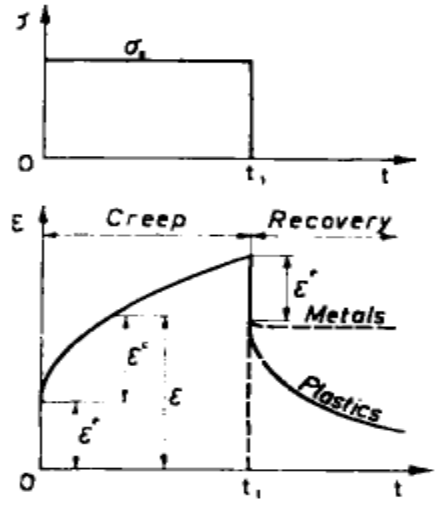

Figure 16 – The creep and recovery trend of metals and plastics (Findley et al., 1976).

The study of creep properties are crucial in all aspects of engineering. For example, creep in cements can have a positive or negative impact on the structure. Creep can assist in relieving stresses caused by strains initiated by shrinkage and changes in temperature. On the contrary, creep can interfere and counteract the artificial stresses imposed on the cement structure (Zhang et al., 2014). In shales, creep can significantly affect the production of hydrocarbons from a reservoir by causing fracture closure, conductivity loss, and reservoir subsidence, and requires a better understanding in order to improve wellbore stability and proppant embedment problems. In addition, creep at high temperatures are still unknown and, hence, the in-situ behavior of shales needs to be investigated. Furthermore, thermal recovery of shales requires an enhanced understanding of reservoir properties at elevated temperatures. In this regard, a quantitative relation between temperature, mechanical properties, and complex chemo-physical mechanisms that cause the thermal alteration needs to be obtained.

Next, a summary of the macroscopic testing procedures performed by various researchers studying creep is provided as well as their findings and limitations.

2.4 Creep testing on shales and a summary of results: macroscopic level

Li and Ghassemi (2012) studied the creep behavior of shales (Barnett, Haynesville, and Marcellus) containing varying amounts of clay and carbonates. They performed this study because there are several factors that affect the quality of the hydraulic fractures in gas-shales and the fracture conductivity. Proppant and asperity embedment as only two of these factors. While elastic properties are time-independent and

occur immediately, the creep (viscous) response is relatively slow and is classified as time-dependent.

Li and Ghassemi (2012) performed experimental tests at room temperature to study the visco-elasto-plastic property of shales. These samples were drilled perpendicular to bedding plane and contained varying amounts of clays and carbonates. Marcellus contained the maximum clay (40%), and the lowest carbonate (9%) and QFP (Quartz, feldspar, plagioclase, and pyrite) (28%). Barnett contained the lowest clay content (25%) and highest QFP (60%). Finally, Haynesville had a clay contented of 33% and a carbonate and QFP content of 23% and 25%, respectively. Samples were tested using a GCTS triaxial rock test system with syringe pumps to control the confining pressure on the samples.

Li and Ghassemi suggested that a linear viscoelastic model such as the Burgers or Maxwell model can be used between the 0-80 MPa range. Between the two models, the Maxwell model does not capture the transient creep portion of the train time relationship whereas the Burgers model, though provides a good fit to the creep strain, fails to capture the effect of plasticity. As a result, Li and Ghassemi suggested using the power law function to observe the creep deformation of shale samples. The power law has been used frequently to determine the relationship between stress, strain, and time. **Eq. 2.1** is also known as the nutting equation and is as follows,

$$\varepsilon^c = k\sigma^p t^n \tag{2.1}$$

where ε^c is the creep strain, σ is the stress, and $k, p,$ and n are the material constants.

Through these studies, Li and Ghassemi (2012) determined that shales with a high content of clays and organic matter creeped more than shales containing carbonates and other silt-size inclusions. A similar correlation was found when measuring the young's modulus through triaxial tests.

Rassouli and Zoback (2016) performed long-term creep experiments on Haynesville shale rocks. They performed the research to understand the effect that viscous deformation has on the mechanical properties and its impact on production. Triaxial creep experiments were performed in a servo-controlled triaxial apparatus in both parallel and perpendicular to bedding planes to observe the anisotropic in both directions. The Haynesville sample was extracted from North Louisiana and East Texas and contain 42% clay, 8% carbonate, and 1.6% TOC.

The experimental results were analyzed using a power-law model in the form of (**Eq. 2.2**)

$$\varepsilon = \sigma B t^{n} \tag{2.2}$$

where ε is the strain, σ is the differential applied stress, B is the empirical constant and n is the power-law exponent. Rassouli and Zoback (2016) found that samples in the horizontal direction showed less creep than in the vertical direction; furthermore, the power-law exponent, n is smaller for the horizontal samples than the vertical samples. Rassouli and Zoback (2016) concluded that the bedding direction plays an important role in the time-dependent compaction of shales.

Sone and Zoback (2013) evaluated the time-dependent deformation of gas shales and their effect on the in-site state of stress. It is well understood that materials with more

and organic matter show a higher time-dependency that samples that have stiffer components.

Sone and Zoback (2013) noted that the mechanical properties of shales can be used for improving wellbore stability, understanding the long-term behavior of the reservoir, and preventing errors in predicting reservoir compaction during depletion and accurate estimation of surface subsidence.

Triaxial tests were performed using a servo-controlled triaxial apparatus. The samples under study were Barnett (rich in QFP), Haynesville, Eagle Ford (carbonate rich), and Fort St. Johns. Here, they assumed that the principle of linear viscoelasticity and the principle of linear superposition (Boltzmann Superposition) holds. The Boltzmann superposition principle is used to describe linearly viscoelastic behavior. The principle states that the total stress outputs as a result of two separate stress inputs applied to a material is equivalent to the total strain output as a result of the total strain input.

Analysis of the experimental results were evaluated for creep using the logarithmic function (**Eq. 2.3**) and the power-law function in the form (**Eq. 2.4**),

$$J(t) = A_1 + A_2 log_{10}(t) \tag{2.3}$$

$$J(t) = Bt^n \tag{2.4}$$

where $J(t)$ is the creep compliance function describing the time dependent strain response, A_1 and A_2 are constants, t is the hold time, B is the compliance constant and n is the power-law exponent, both of which are constitutive parameters. The compliance constant

is the amount of strain that occurs after 1s of input stress. The power law exponent is the tendency to exhibit time-dependent deformation. The power law predicted future creep behavior more accurately.

Sone and Zoback (2013) found that Eagle Ford and Haynesville show a significant level of creep after three hours. Similar to the understanding by many researchers, they found that creep is directly proportional to the amount of clay/organic matter in the sample. Higher amounts of soft material means higher the creep rate. In equation form, 1/B correlated with the elastic modulus and a higher power-law exponent means higher creep behavior. The difference in anisotropy was also noted from the results, where horizontal samples had a tendency to creep less than vertical samples (horizontal B and n < vertical B and n).

The drawback to macroscopic testing is that researchers are unable to study the individual contribution of the material phases on the over property of the rock.

This section included a summary of the macroscopic experimental procedures and results performed by various researchers. However, methods such as Nanoindentation and Atomic Force Microscopy can be used to study the behavior of shales. Next, a similar summary of nanoindentation tests performed to measure creep is included.

2.5 Creep testing on shales and a summary of results: microscopic level

Slim et al., (2017) performed indentation experiments at the nano- and microscale levels to study role of organic matter. The study was performed because having a better

understanding of the viscous behavior of gas shales could sheds light on its effect on drilling, hydraulic fracturing, and pressure depletion due to production.

Slim et al, (2017) performed indentation tests to study the role of organic matter within mature and immature shales. The samples were divided based on two schemes: granular morphology, also known as self-consistent morphology, and Mori-Tanaka morphology, also known as inclusion morphology. Self-consistent morphology considers porosity to be evenly distributed throughout all phases of the material with the clay phase containing most of the organic matter; this method assumes a "disordered morphology" in which neither the solid nor the pore space makes up the matrix (Abedi et al., 2016). As a result, a percolation threshold (porosity level) of 0.5 exists for this method, above which the self-consistent scheme is no longer valid. Samples included Marcellus and Haynesville shales (mature samples). The Mori-Tanaka morphology is based on the assumption that the pore is completely surrounded by the solid phase (Dormieux et al., 2006). This approach considers porosity and kerogen to be concentrated within the matrix (clay) and applies specifically to immature samples (Abedi, et al., 2015). Samples included Antrim, Barnett, and Woodford shales.

Slim et al., (2017) used a chemo-mechanical approach to study the porous kerogen/clay phase present within these samples. For nanoindentation tests, a maximum force of 4.8mN is used, whereas a maximum force of 12-50nN is used for microindentation tests. Next, EDX is used to obtain the chemical information of the indented spaces. Finally, the clustering technique called MCLUST is used to analyze the experimental results and separate the data in similar phases.

Slim et al., (2017) used a logarithmic fit which could be used to quantify the contact creep modulus and characteristic time. They found that the contact creep modulus and characteristic time increased as the material became stiffer. The clay/kerogen phase is the softest component of the sample and the contact creep modulus for the porous clay/organic matter is the lowest as well. This means that the creep rate is high. In differentiating between mature and immature samples, Slim et al., (2017) determined that the creep rate present within the source rocks was isotropic, which also shows that a relationship exists between the isotropy of the contact creep modulus and the isotropic nature of kerogen and porosity.

Jones and Grasley (2010) measured the creep properties of cements using nanoindentation. They performed this study to have a better understanding of the deformation mechanisms within concrete. Obtaining the input parameters for the multi-scale response of Portland cement concrete can help predict the macroscale behavior of cements. With few studies on using nanoindentation as a tool for measuring the creep properties of cements, Jones and Grasley (2010) performed nanoindentation tests to quantify the viscoelastic behavior of cements at the nanoscale.

Specially cement samples cured in 98% humidity at room temperature and placed in lime water for 90 days were prepared and cut into 3mm tick plates for indentation. The Hysitron Triboindenter model TI-900 was used for creep tests and indented into using a Diamond Berkovich tip. The hold period for the tests was either 30s or 1 hour.

Jones and Grasley (2010) applied the elastic-viscoelastic correspondence principle, which makes use of the Laplace transformation to solve the boundary value

problem. Using the displacement (nm) versus time (sec) graph, a best fit function was applied to the raw data to obtain a fitted curve. Lee and Radok (1960) showed that, for indentation problems, this correspondence principle can be applied as long as the contact area (or equivalently the penetration depth) increases monotonically. They used a stretched exponential function (**Eq. 2.5**), where E_o is the initial elasto-plastic penetration, E_1 is the magnitude of the time-dependent penetration, and β controls the shape of the relaxation/retardation function.

$$J(t) = \frac{1}{E_0} + \frac{1}{E_1(1 - e^{-1})}(1 - e^{-\frac{t}{t_h}^{\beta}}) \tag{2.5}$$

where E_o controls the initial elasto-plastic penetration into the material, E_1 controls the magnitude of the time-dependent penetration, and β controls the shape of the relaxation/retardation function. They determined that three peaks exist within the fitted parameters, indicating the contribution of the low-density C-S-H, high-density C-S-H, and ultra-high density C-S-H phases (**Fig. 2.17**).

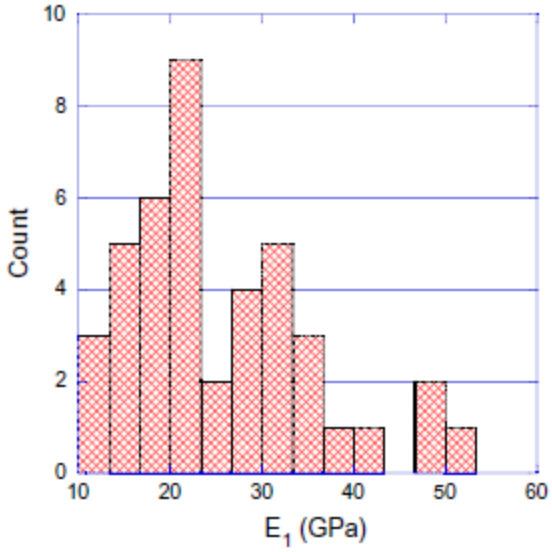

Figure 17 – A histogram distribution of the constitutive parameter E_1, the time-dependent penetration, for 30 second tests showing the trimodal distribution representing low-density C-S-H, high-density C-S-H, and ultra-high density C-S-H (Jones and Grasley, 2010).

Zhang et al., (2014) performed long-term creep tests on cementation materials comparing microindentation tests to macroscopic tests. Autogenous shrinkage, drying shrinkage, and aging are just three factor that contribute to the deformation of the material; creep is the fourth factor and occurs due to external mechanical load and can be divided into short-term creep and deviatoric long-term creep.

Creep was performed on concrete for 14.5 years using uniaxial compression. Autogenous shrinkage tests were performed, where on sample was held constant (no external load) and another sample was held under a constant load. Meanwhile, months-long (100 days) uniaxial compression creep experiments were performed. Lastly, minutes-long creep tests were performed at room temperature using the microindenter.

The results obtained from these experiments were plotted on a semi-log plot where time (day or seconds) was in a log form and the uniaxial creep function/contact creep function were in a Cartesian form. Next, a logarithmic model was fit to the raw data using regression and two parameters were obtained: the contact creep modulus (**Eq. 2.6**) for indentation tests or a Uniaxial creep modulus (**Eq. 2.7**), which quantifies the long-term creep kinetics, and the characteristic time (τ), which represents the point at which the creep kinetics starts to show logarithmic behavior. The time component (t) represents the holding period during which the primary stage of creep occurs.

$$L(t) - \frac{1}{M_o} = \frac{\ln(t/\tau_i + 1)}{C_i} \tag{2.6}$$

$$L(t) - \frac{1}{E_o} = \frac{\ln(t/\tau_u + 1)}{C_u} \tag{2.7}$$

The contact creep compliance function, $L(t) - L(0)$, can be obtained by integrating **Eq. 2.8** with respect to time from the beginning of the holding phase (Zhang et al., 2014) to obtain **Eq. 2.9**. The contact creep compliance rate, $\dot{L}(t)$, can be obtained during the holding phase of the nanoindentation creep experiment (Vandamme and Ulm, 2013). In **Eq. 2.8**, P_{max} is the applied loading during the creep phase, a_u is the equivalent projected contact area between the indenter and the indented material at the onset of unloading, and $\dot{h}(t)$ is the rate of penetration of the tip during the creep phase.

$$\dot{L}(t) = \frac{2a_u\dot{h}(t)}{P_{\max}} \tag{2.8}$$

$$L(t) - L(0) = L(t) - \frac{1}{M_o} = \frac{2a_u \Delta h(t)}{P_{max}} \quad (2.9)$$

Zhang et al., (2014) determined that nanoindentation was an accurate measure for determining the creep properties of cements by comparing the results to uniaxial tests, one that was years long and one that was months long.

2.6 Temperature testing and mechanical properties of shales

This section summarizes the various instruments used by researchers to study the behavior of shales, the objectives of their research, and experiments performed to study shales at high temperatures. This section is created to discuss other types of research on shales, particularly those related to high temperatures and/or mechanical properties (time-independent) that shed light on the developments made in these two areas. Researchers whose works have been summarized below include, Smith (2010), Grebowicz (2014), Eliyahu et al., (2015), Ahmadov et al., (2011), Emmanuel et al., (2016), Zargari et al., (2013), Shukla et al., (2013), Kumar et al., (2015), Abousleiman et al., (2007), Abedi et al., (2015), and Deirieh et al., (2012).

Smith (2010) introduced a study to recover hydrocarbons from unconventional reservoirs using heat (SAGD, Steam Assisted Gravity Drainage) produced from High Temperature Gas Reactors (nuclear energy). The study proposed heating the organic matter at a slow rate at temperatures between 350-400^{o}C for improved hydrocarbon

recovery. This method would eliminate the use of natural gas as a heat source and reduce CO2 emissions.

Grebowicz (2014) performed a thermal analysis of Green River Basin shale samples in order to investigate the use of nuclear heat as a heat source for increasing hydrocarbon recovery. Grebowicz determined that kerogen begins to decompose around 320^{o}C. Furthermore, through the use of Thermogravimetry Analysis (TGA) from room temperature to 1000^{o}C, Grebowicz proved that kerogen and carbonates decomposed below 460^{o}C only and above 500^{o}C, respectively. This comprehensive study to monitor the behavior of shale constituents under high temperature serves to further research initiatives for using the nuclear energy produced by reactors for In-situ Conversion Processes (ICP).

Eliyahu et al., (2015) obtained the mechanical properties of the various phases present in shales using Atomic Force Microscope (AFM). With the additional use of EDX elemental maps, they determined that four phases were present on the sample surface: pyrite, quartz (63 +/- 8 GPa) and calcite (52 +/- 6 GPa), clay minerals (29 +/- 1 GPa), illite and Fe-chlorite), and kerogen (0-25 GPa). A similar study was also performed by Ahmadov et al, (2011) using Atomic Force Microscopy to study kerogen. The study was conducted to build a better understanding of borehole stability and fracturing techniques and hydrocarbon flow.

For shales, Emmanuel et al., (2016) studied the behavior of organic matter at high temperatures using another high-resolution technique called Atomic Force Microscopy (AFM). They studied the mechanical response of both kerogen and bitumen and noticed that bitumen became softer with increasing temperatures whereas kerogen underwent little

to no change (**Fig. 18)**. While large scale high-resolution studies have been performed on concretes and shales, little evidence is found on measuring the mechanical behavior (elastic, strength, and creep) of shales at the microscopic scale through high temperature nanoindentation tests.

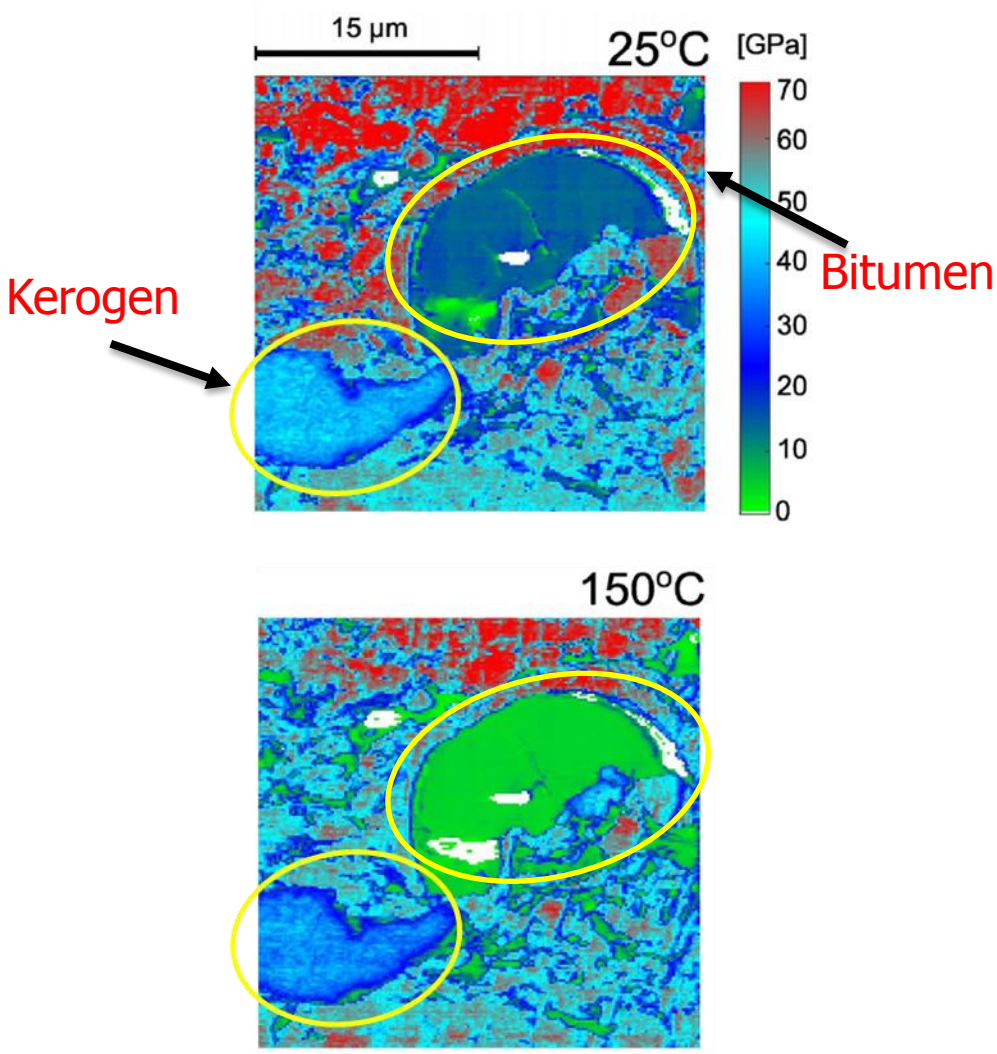

Figure 18 – Maps of reduced modulus at 25°C (top) and 150°C (bottom) where the conversion of Bitumen is much greater (becomes softer) and Kerogen remains relatively the same in comparison (Emmanuel, et al., 2016).

Zargari et al., (2013) performed a large scale nanoindentation study to monitor the behavior of kerogen in Bakken shale samples. Hydrous pyrolysis, which is pyrolysis in the presence of water, was used, through which the samples were heated to 350^{o}C for 72 hours. Studies have shown that hydrous pyrolysis produces hydrocarbons similar in nature to that of reservoir rocks. Several observations were noted. First, by observing the sample surface under a Scanning Electron Microscope, a color change occurred and was linked to calcification of carbonates. Second, kerogen present within the immature samples showed a reduction in TOC and transformation of kerogen into bitumen/hydrocarbons; this was correlated to a reduction in the Young's modulus for these immature samples, measured through nanoindentation. For mature samples, the Young's modulus remained the same or increased slightly. Unlike kerogen in immature samples, where the kerogen exists in clusters, kerogen in mature samples are interspersed within the clay matrix (Abedi et. al., 2015). Mature samples showed little to no increase in modulus, whereas immature samples became softer. This study enhances the understanding of the evolution of shales when exposed to higher temperatures.

Shukla et al., (2013) performed a nanoindentation study on Wolfcamp, Woodford, Barnett, Haynesville, Eagle Ford, and Collingwood shale samples to obtain the mechanical properties of the various phases present (pyrite, carbonates, clay, and kerogen). These results were then compared to hypothetical drill cutting samples prepared from crushed core sample pieces ranging between three and five millimeters. The young's modulus values of these "drill cuttings" were in between the perpendicular and parallel modulus values obtained previously, as was expected due to the randomness of the bedding

orientation. There are several take away points from this experimental effort. First, using drill cuttings is a cost effective method to obtain the mechanical properties of the pay zone, thereby improving hydraulic fracture design efforts. Second, an increase in porosity correlated with an increase in TOC, meaning that TOC contains a large amount of porosity. Third, and likely the most crucial comparison in the development of in-situ hydrocarbon recovery efforts, is the nanoindentation measurements on TOC before and after exposure to "low temperature." Kerogen was placed under a low temperature plasma ash for six hours, causing an increase in the modulus value. This was believe to be associated to the loss of the light hydrocarbons released from the concentrated kerogen.

Kumar et al., (2015) also performed a similar study on shales, particularly Barnett, Eagle Ford, Haynesville, Kimmeridge, Ordovician, and Woodford, to determine the dependence of porosity, TOC, and clay content on the elastic modulus. Kumar et al. determined that the elastic modulus decreased with increasing TOC, porosity, and clay content. Meanwhile, the elastic modulus increased with increasing quartz and carbonate (QC). Obtaining the mechanical properties is crucial in designing appropriate hydraulic fracturing designs, particularly in horizontal wells. Furthermore, due to the high cost of extracting core samples, drill cuttings can be used to interpret the type of shale present in the pay zone.

Abousleiman, et al., (2007) analyzed the mechanical properties of Woodford shale samples and correlated the results to acoustic measurements and log interpretations. Small shale samples were used for nanoindentation to reflect realistic sizes of drill cuttings,

proving the effectiveness of using readily available pay zone rocks rather than core samples that are expensive to extract and preserve.

Abedi et al., (2015) studied the mechanical behavior of the porous clay phase (with intermixed organic matter) in both mature and immature samples through a coupled nanoindentation-EDX analysis. The importance of this research is directly linked to developing predictive reservoir models in place of conducting costly experiments. A statistical clustering methodology was used to separate the clay phase from the remaining phases. Next, a power function was used to fit all of the experimental data; the power function indicated that the stiffness of the sample was directly dependent on the hardness. In other words, as hardness increased, so did the indentation modulus.

Deirieh et al., (2012) performed a similar study to Abedi et al, (2015) in terms of experimentally performing calculations on clay rich samples by measuring the mechanical (through nanoindentation) and chemical components (through Wave Dispersive Spectroscopy). They also used a statistical clustering approach to observe the mechanical properties of the clay phase. This research effort is important for developing appropriate drilling strategies, hydraulic fracturing, and carbon sequestration initiatives as they require a thorough understanding of the heterogeneous nature of shales.

2.7 Reservoir temperatures of shales

Reservoir temperature within the Haynesville shale formation is relatively higher than other shale formations. A comparison of the reservoir temperatures of Marcellus, Fayetteville, and Haynesville is shown in **Tables 1-3** from various sources. It can be seen

that the average reservoir temperature for Haynesville is between 323-338°F, whereas the average temperature for Marcellus and Fayetteville are between 132-148°F and 117-187°F.

Table 1 – Marcellus formation temperature (°F).

Marcellus Formation Temperature (°F)	Reference
140	Williams et al., 2011
120-150	Kargo, D et al., 2010
100-150	Gaultieri D., 2009
140	Izadi et al., 2014
160	Ajayi et al., 2011

Table 2 – Fayetteville formation temperature (°F).

Fayetteville Formation Temperature (°F)	Reference
120-220	Fritz, B. et al., 2012
100-150	Terracina J.M. et al., 2010
120-220	Bai B. et al., 2013
120-220	Deville J. P. et al., 2011
125	Song B. et al., 2011

Table 3 – Haynesville formation temperature (°F).

Haynesville Formation Temperature (°F)	Reference
315	Parker M et al., 2009
>300	Thompson J.W. et al., 2010
>350	Guo Q. et al., 2012
300-375	Pope C. et al., 2009
350-360	Trichel, K. et al., 2011
325	Terracina J.M. et al., 2010

2.8 Chapter summary

In the first portion of chapter II, the three level multi scale structure model is provided. Here, the three levels are differentiated and uses of each level is explained.

Nanoindentation tests are performed at level I, which is the porous clay/kerogen interface (clay + kerogen + porosity). Following this discussion, a detailed summary of the types of clays present in shales is introduced supported by supporting details of each clay and pictures taken under microscopes. In this study, the primary clay present in the sample is illite, which is a 1:1 type clay with little water content. In section 2.3, the concept of creep and the theory behind it is explained. Much of the experimental work measures the primary section of creep and the beginning portions of secondary creep. A literature review of studies performed at the macroscale and microscale along with results in each of those experiments is listed. Of particular importance is the microscale research performed by Zhang et al., (2014), Jones and Grasley (2010) and Slim et al., (2017). Their findings and analytical approach will be considered and partially used to study the experimental results in this thesis. In support of microscale and macroscale studied performed including, but not limited to, the mechanical properties (time-independent) is briefly mentioned in section 2.6. Finally, a comparison of reservoir temperatures of Haynesville, Marcellus, and Fayetteville are compared to show the relatively higher formation temperature of Haynesville as compared to other shale formations.

CHAPTER III

MATERIALS AND METHODS

Chapter three is broken into six major categories. First, details on the sample preparation methodology is provided along with schematics. Second, information on the type of sample used, including compositional results, porosity calculations, TOC and Rock Eval results, and experimental settings to measure Thermogravimetry are presented. Third, the theory behind nanoindentation, measurement testing techniques and the steps required to obtain accurate indentation results are discussed in depth. The fourth and fifth section include details on the SEM&EDX equipment used and data collection from this equipment as well as the procedure to couple the mechanical (nanoindentation) and chemical (EDX) technique. Finally, the chapter ends with a description of the model-based clustering technique and the application of it in evaluations the coupled experimental data.

3.1 Sample preparation

Shale is extremely heterogeneous and is composed of minerals with different mechanical and chemical properties. Furthermore, shales are considered transversely isotropic materials, where stiffness C_{11} is close to C_{22} and twice as large as C_{33}. (Wenk et al., 2007). As a result, to comprehensively determine the mechanical properties of shales, evaluation is required in both parallel (X1) and perpendicular (X3) to bedding planes.

Traditionally, two methods have been used by researchers to reduce the sample roughness. The first method utilizes broad beam argon ion milling (Kumar et al., 2012) and the second method uses a series of polishing pads (Abedi et al., 2015). Ion milling is

a procedure in which particles are raster-polished away from the surface to create a smooth and flat surface. One major drawback to using ion milling is the embedment of material particles into the pore space. This issue can interfere with providing nanoindentation measurements that are reflective of the true mechanical properties of the material. Loucks et al., (2012) also proved that ion milling may lead to a "curtaining" effect which could cause "a minor annoyance in photomicrographics" when images are taken of the sample. Consequently, the second method (manual polishing) is performed on all Haynesville samples in this study.

The samples are prepared in the following manner. First, proper evaluation of the sample is needed to determine the direction of bedding plane. **Figs 19A and 19B** show a visual of the directions and corresponding nomenclature used throughout this thesis. Using these guidelines, an Eagle Ford outcrop sample is shown in **Fig. 20A** indicating the location of the bedding planes. The visibility of the bedding planes vary significantly depending on the amount of TOC present in the sample and the depositional environment. Given the transversely isotropic nature of shales, samples need to be prepared in two directions.

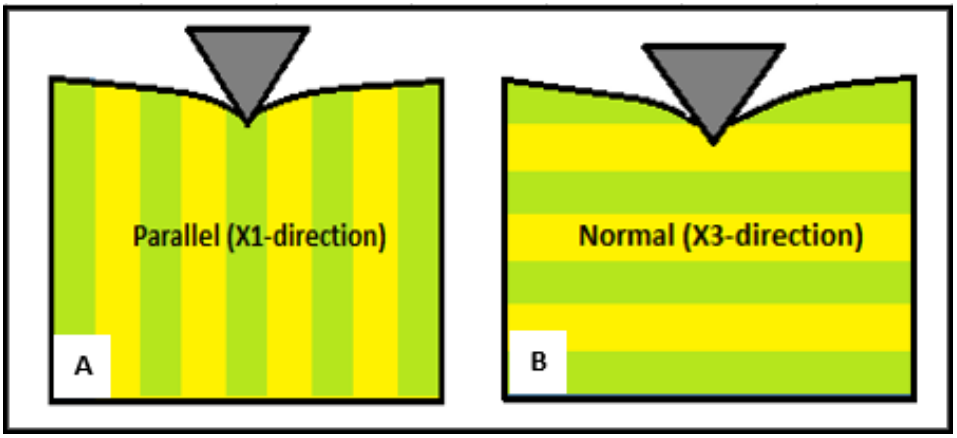

Figure 19 – Bedding planes illustrated in both parallel (left) and perpendicular (normal) (right) directions.

The second step is to cut the sample in each direction using a diamond saw machine (**Fig. 20B**). Lubricant (n-Decane) is used to prevent damage to the blade and the sample material. The third step is to grind the sample (**Fig. 20C**) using a 25µm polishing pad (Buehler TextMet) lubricated with an oil-based diamond suspension (**Fig. 20D**) for 10-15 minutes, or as needed. The fourth step is to clean the sample in an ultra-sonic water bath for 20 minutes (**Fig. 20E**). The sample is submerged in n-Decane and placed in a graduated cylinder; the graduated cylinder is then placed into the water bath for cleaning. Caution should be taken to ensure that only n-Decane (not water) is in contact with the sample. Sound waves from the sonic bath form microscopic bubbles (cavitation) at low pressures which implode at high pressures, creating enough energy to remove loose particles from the sample surface. The next step is to manually polish the sample using FiberMet (Buehler) polishing pads (9µm, 3µm, 1µm, and when needed, 0.3µm) (**Fig. 20G**) on a flat surface (**Fig. 20F**) to reduce the sample roughness (**Fig. 20H**). The sample should be washed repeatedly using the sonic bath to remove lose particles from the sample surface.

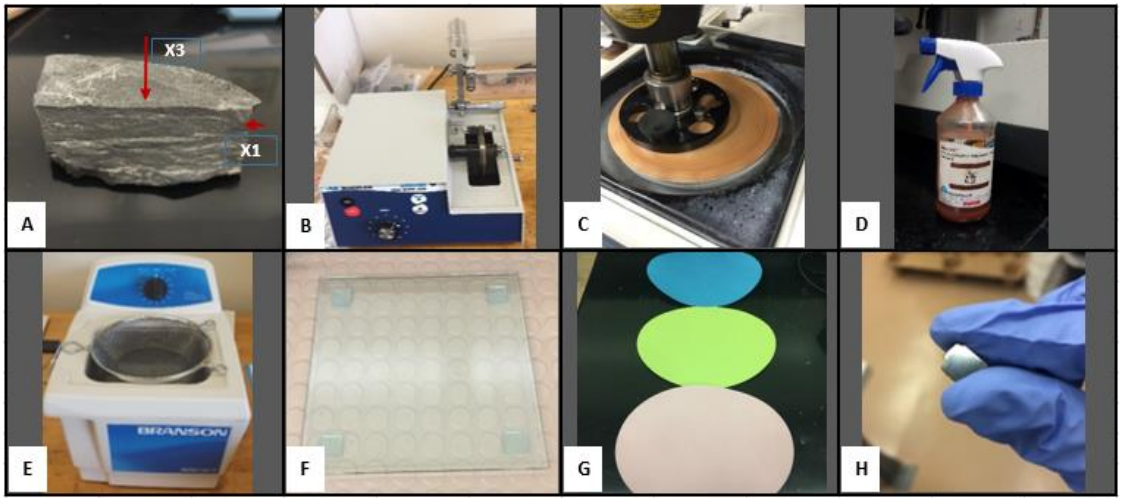

Figure 20 – (A) Eagle ford outcrop sample depicting the direction of bedding plane, (B) Buehler diamond saw machine, (C) Buehler grinding machine (located at Materials Characterization Facility, Texas A&M University), (D) Buehler diamond suspension (25µm), (E) Branson ultra-sonic water bath with mesh, (F) polishing glass surface, (G) Buehler TexMet polishing pads, and (H) finished sample surface.

The sample height is limited by the thickness of the rubber gasket placed in between the Nanoindenter temperature stage. Furthermore, the sample width should be smaller than the ceramic heating pod stationed at the bottom of the temperature stage. Samples tested under ambient conditions were approximately 6x6x6mm (*lxwxh*) and samples tested within the temperature control stage were 4x4x2mm.

Upon completion of clustering analysis, consistency in indentation depth was used as a standard to confirm polishing quality. Donnelly et al. (2006) determined that for proper surface measurements of shales, surface roughness should be three times smaller than the indentation depth.

Samples under investigation were carbon coated (20nm) to prevent electron charge build-up during imaging.

3.2 Porosity, XRD, TOC, rock eval and thermogravimetry

The purpose of this section is to provide information on the composition of the sample under study in this research. Additionally, methods and results of testing porosity of shale samples are introduced as well as volume fraction calculations to support the multi-scale thought model discussed previously. The results provided here will be used to interpret the chemo-mechanical properties obtained for the clay/kerogen phase.

3.2.1 Shale sample

The Haynesville shale core sample was provided by the Harold Vance Department of Petroleum Engineering at Texas A&M University. The Haynesville sample contains both organic and inorganic matter and was extracted from a gas-rich zone. Little information on the composition and porosity was provided thereby requiring XRD and porosity tests to be performed. The sample presents a high level of transverse anisotropy, with an anisotropic ratio of approximately 4:3 as determined through experimental results.

3.2.2 Composition of Haynesville (XRD results)

The composition of this sample was obtain by X-ray diffraction (XRD). The sample was also studied under the Energy Dispersive Spectroscopy (EDX) to qualitatively verify the validity of the XRD results. The XRD results and EDX distributions are provided in **Table 4**.

Table 4 – X-Ray Diffraction (XRD) and Energy Dispersive Spectroscopy (EDX) results for Haynesville shale.

Mineralogy	Haynesville Shale (wt. %)	Haynesville Shale (% Distribution per EDX map, fig. 3.3)
Clay	27.50	65.30
Quartz	23.10	10.01
Carbonate	40.90	13.84
Pyrite	1.40	1.800
Feldspar	6.20	8.050
Apatite	0.90	1.000
TOC	2.77	(combined with clay)

Fig. 21 represents the elemental overlay of silicon, aluminum, magnesium, sulfur, calcium, and sodium taken under an Energy Dispersive Spectroscope. The overlay is used to visually check the distribution of the various minerals present within the sample and compare the results to those obtained from an XRD test. It can be noticed that the differences between the EDX and XRD results for Pyrite, Feldspar, and Apatite are within close proximity of one another whereas the clay, quartz, and carbonate distributions vary significantly. Explanation for this resides in the fact that an area that is rich is clay and poor is quartz and carbonate was selected for indentation experiments. Comparing the results provided in Table 1, nonetheless, proves that the mineralogy detected through both approaches are the same; in other words, no additional mineralogy was detected through one method that was detected through the other method.

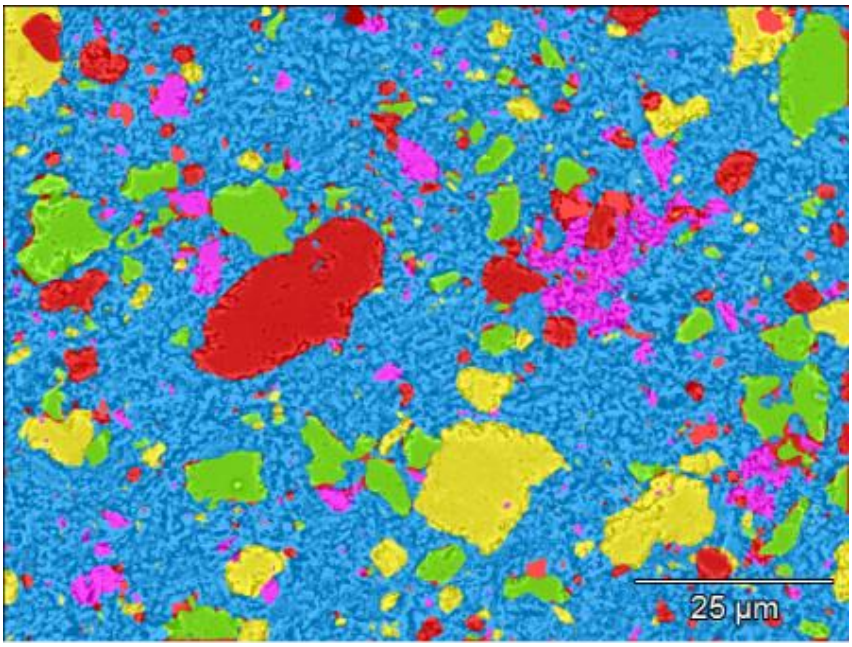

Figure 21 – Energy Dispersive Spectroscopy (EDX) results for Haynesville set 1 X3 250°C.

3.2.3 Porosity calculations

There are several experimental and analytical methods to determine the porosity of shales samples. The first method uses the mineralogy data obtained from the XRD results to determine the bulk density of the shale sample. The following equation can be used to calculate the porosity of a shale sample:

$$\frac{\emptyset}{100} = \frac{\text{Bulk Volume} - \text{Total Mineral Volume}}{\text{Bulk Volume}} \tag{3.1}$$

which can be re-written as,

$$\frac{\emptyset}{100} = 1 - \frac{\sum_{i=1}^{N}\left[\frac{\text{XRD wt. \% of mineral x } (100 - \text{\% TOC})}{\frac{100}{\rho_i}}\right]_{\text{inorganic}} + \left[\frac{\text{\% TOC}}{\rho_{TOC}}\right]_{\text{Organic}}}{\frac{100}{\rho_{bulk}}} \tag{3.2}$$

The second method to determine the porosity is to determine the bulk density of the shale sample before and after saturation. To obtain the bulk density after saturation, the sample is submerged into a fluid to allow the fluid to occupy the pore space. When considering the bulk density of the unsaturated sample, the sample should be oven dried (60°C, 2 hours) to remove any surface water present within the sample. Combining these two values, the following equation can be used to calculate the porosity:

$$\frac{\emptyset}{100} = \frac{\rho_{saturated} - \rho_{unsaturated}}{\rho_{saturated}} \tag{3.3}$$

$$\frac{\emptyset}{100} = \frac{\frac{mass_{saturated}}{Volume} - \frac{mass_{after\ oven-drying}}{Volume}}{\frac{mass_{saturated}}{Volume}} \tag{3.4}$$

$$= \frac{mass_{saturated} - mass_{after\ over-drying}}{mass_{saturated}}$$

The third method to calculate porosity in shales is through the use of helium porosimetry or mercury porosimetry (MICP). This method is conducted by pressurizing the crushed sample with helium or mercury within a closed chamber. MICP tends to underestimate the porosity. Mercury porosimetry was performed on Haynesville by Nutech PoroLabs.

The volume fraction of the Haynesville sample can be divided as such:

$$\eta_s + \eta_k + \emptyset = 1 \tag{3.5}$$

where the sum of the inorganic phase (clay), organic phase (kerogen), and porosity equal to one. **Eq. 3.6 and 3.7** can then be used to calculate the kerogen volume fraction:

$$\eta_k = \frac{f_k}{f_k + f_c + \emptyset_{k+c}} \tag{3.6}$$

$$\eta_c = \frac{f_c}{f_k + f_c + \emptyset_{k+c}} \tag{3.7}$$

Abedi et al. (2016) noted that the porosity at level I is equivalent to the porosity at level II in a self-consistent (mature) morphology which means $\phi = \varphi$; this is not applicable to immature samples. **Table 5** lists the calculations followed to obtain the volume fractions of clay and kerogen using the XRD values provided. Considering the high maturity of organic matter in the Haynesville sample, we assumed a density value of 1.3 g/cm^3 (Sone and Zoback, 2013).

Table 5 – Material volume fraction calculations for Haynesville shale.

Haynesville Composition	Mineral Density (g/cc)	XRD wt. % (Table 3.1)	Rescaled wt.%	Volume (cc) (XRD wt. %/density)	Fraction (100-Φ)*Vol./(Tot. Vol)
Chamosite (Chlorite)	2.9	1.70	1.65	0.57	1.45
Illite	2.65	25.80	25.09	9.47	24.10
Albite (Feldspar)	2.65	6.20	6.03	2.27	5.79
Apatite (Phosphates)	2.85	0.90	0.88	0.31	0.78
Carbonate	2.71	33.20	32.28	11.91	30.32
Dolomite	2.86	7.70	7.49	2.62	6.66
Quartz	2.65	23.10	22.46	8.48	21.58
Pyrite	5.01	1.40	1.36	0.27	0.69
Total		100.00			0.00
TOC	1.3		2.77	2.13	5.42
Total minus TOC %		97.23			
Total		102.77	97.23	38.03	96.80
Porosity (%)	3.2				
Porosity in Clay+Kerogen	1.02				
Volume Fraction of Clay	0.7985				
Folume Fraction of Kerogen	0.1695				

3.2.4 TOC and rock eval results

Rock eval. analysis was performed to understand the maturity level of the Haynesville shale sample. Analysis was performed by Nutech PoroLabs. **Table 6** shows the Tmax, S1, S2, S3, and calculated Ro values. Tmax is an indicator of maturity, where higher values mean higher the maturity. S1 is the amount of free hydrocarbons in the sample, S2 is the amount of hydrocarbons that the rock is capable of producing, S3 is the amount of CO_2 produced, and Ro is the vitrinite reflectance. Here, a value of Ro is indicative that the sample is from a dry gas zone and a Tmax value of 495 shows that the sample is mature.

Table 6 – Rock eval results obtained for a Haynesville core sample.

Rock Eval. Results	
Tmax	495
S1	0.79
S2	0.37
S3	0.30
Calculated R_o	1.75

3.2.5 Thermogravimetry

Thermogravimetric Analysis (TGA) is used to study the weight behavior of a material over a range of temperatures and time intervals. This methodology can be applied to both conventional and unconventional reservoir rocks. TGA can be used to study the removal of volatile components, loss of moisture, and adsorption/desorption within the nanopores. TGA tests was performed using TA Instruments Model Q500 (SN: 0500-1104) per testing method ASTM E1131-08 (2014); an image of the instrument is shown in **Fig. 22**.

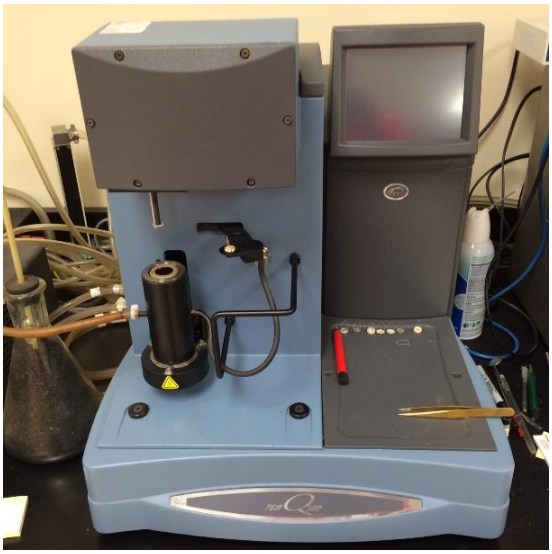

Figure 22 – TA Instruments Model Q500 used to perform Thermogravimetry Analysis on Haynesville.

Table 7 shows a summary of published TGA data on shales with heating rates and other experimental parameters followed.

Table 7 – TGA published results on shales.

Rock	Temperature Range (°C)	Heating Rate (°C/min.)	Gas Used	Purge Rate (ml/ min.)	Relative Humidity (%)	Source
Haynesville	110-200	5	Reagent grade Nitrogen (N_2)	50	50	U. Kuila, et al. 2013
Conclusion: TGA used at 200°C to remove clay bound water from the clay (illite) rich Haynesville shale sample; between 110-200°C, weight % loss of 0.14%; total weight % loss of 1.92%; 9-11% porosity						
Barnett	900	3	Nitrogen Gas (N_2)	N/A	N/A	T.G. Easley, et al. 2007
Conclusion: TGA can be used to clean shale gas samples; clay bound water calculation for shales						
Bakken, Eagle Ford, and Utica	1100	10	Nitrogen Gas (N_2)	40	Desiccator humidity	J. P. Gips, et al. 2014
Conclusion: Less than 100°C, free fluid escapes						

The following settings were used to obtain the TGA results for Haynesville shale in this research. The sample was heated at a rate of 1°C/min. or 5°C/min. up to 300°C or 350°C. Nitrogen gas was used at a purge rate of 50ml/min. Sample weight of 40-60mg were used during each experiment.

3.3 Nanoindentation

3.3.1 Background and introduction to nanoindentation

The nanoindentation technique has been in application since the early 1700's (Ulm et al., 2005). In the 1980's and 1990's, developments in nanotechnology, much to the

contributions of Bulychev, et al. (1975), Doerner and Nix (1986) and Oliver and Pharr (1992), have paved way to quickly and accurately determine the mechanical properties of materials using a depth sensing technique. Well known for their contribution to mechanical testing at the sub-micron scale, Oliver and Pharr performed studies on the indentation load-displacement behavior of six homogeneous samples to tabulate their elastic and strength properties. The Nanoindenter used in this study is the Hysitron TI-950 located at The Texas A&M University – Microscopy Characterization Facility (**Fig. 23)**.

Figure 23 – Hysitron TI-950 Nanoindenter located at the Texas A&M University – Microscopy Characterization Facility.

The setup of nanoindentation can be understood as follows. A ceramic indentation probe with a diamond tip is connected to a transducer to control the load applied on the specimen (**Fig. 24**). For the purposes of elastic, strength, and/or creep properties, a berkovich tip has been used by researchers to penetrate the sample (Jones and Grasley (2010), Vandamme and Ulm (2013), Abedi et al. (2015), and Slim et al., (2017)). These researchers have proven to effectively and accurately measure the mechanical properties of the various phases present within the specimen using large grids of indentations. The berkovich tip leaves a triangular impression on the sample surface, as shown in **Fig. 25**, in which both elastic and plastic deformation occur. During retraction of the tip from the sample surface, only the elastic properties are recovered and can be used to determine the mechanical properties of the indented material.

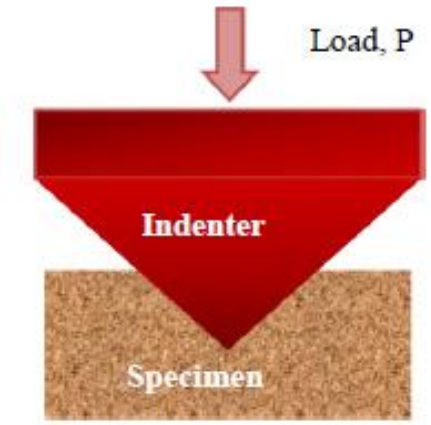

Figure 24 – Schematic of a diamond tip indenting into the sample surface (Kumar et. al., 2012).

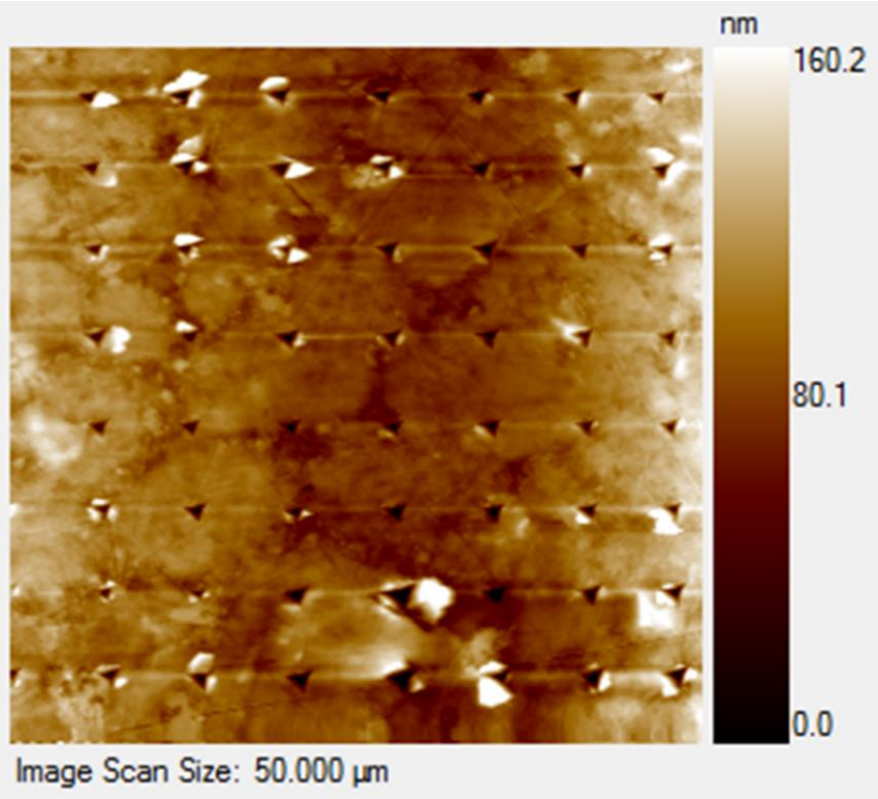

Figure 25 – Berkovich indentation on a polished Eagle Ford shale sample using contact-mode imaging; taken at the Texas A&M University Materials Characterization Facility.

Fig. 26 is a schematic representing the load-depth curve from an indentation test. During the loading and unloading phases of indentation, the load (P) versus displacement (h) curve is continuously measured by the indenter probe (**Fig. 24)**. Using the P-h curve as well as the slope of the unloading curve, also known as the contact stiffness (S), the indentation modulus and indentation hardness of the probed material is calculated.

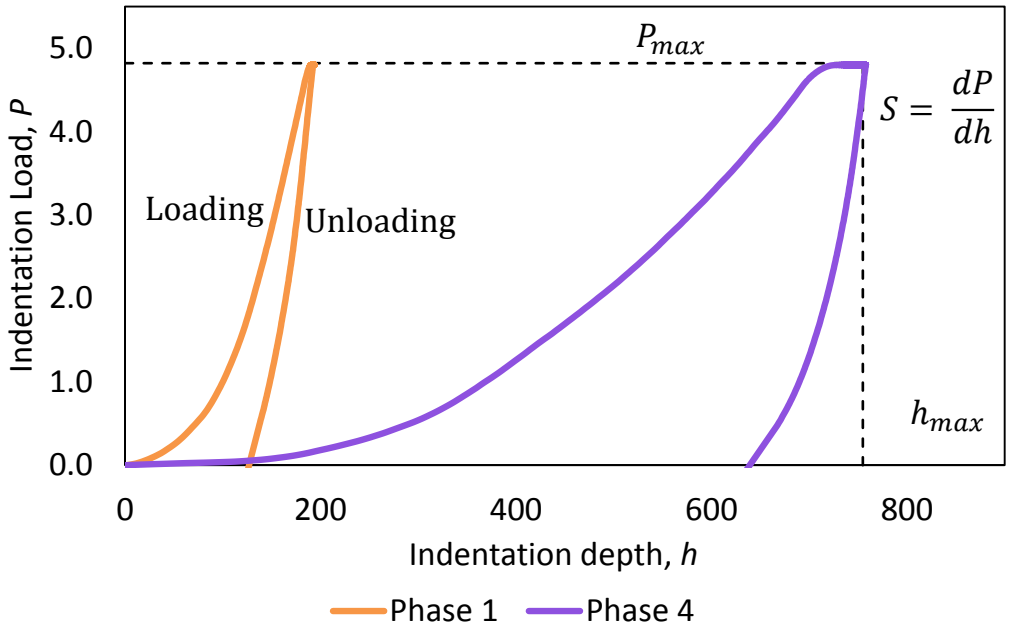

Figure 26 – Schematic of indentation depth versus load for two indent (Oliver and Pharr, 2003).

3.3.2 Indentation modulus

Originally proposed by a group of researchers, the BASh (Bulychev et. al. 1975) method provides an analytical tool for determining the elastic modulus. Indentation modulus is commonly represented by **Eq. 3.8**.

$$M = \frac{\sqrt{\pi}}{2} S \sqrt{A_c} \tag{3.8}$$

where, S is the initial slope of the unloading curve and is shown in **Eq. 3.9**.

$$S = \frac{dP}{dh} = \frac{2}{\pi} E_r \sqrt{A_c} \tag{3.9}$$

$$A_c = \pi {a_u}^2 \tag{3.10}$$

E_r is the reduced modulus and A_C is the portion of the tip that is in contact with the specimen (**Eq. 3.10**); a_u is the contact radius between the tip and the sample surface. The A_C parameter was also proposed by BASh and can be calculated using indirect methods using the maximum indentation depth. Oliver and Pharr introduced **Eq. 3.11** which can determine the contact height of the probed region. To account for the edge effects, a geometric constant of $\varepsilon = 0.75$ is used in this equation.

$$\frac{h_c}{h_{max}} = 1 - \varepsilon \frac{P_{max}}{S\, h_{max}} \tag{3.11}$$

The contact area is determined using the geometry of the tip and the depth of the contact, where the indenter geometry can be determined using the area function that relates the contact area to the indenter depth (h_{max}) as shown in **Eq. 3.12**.

$$A = C_o h^2 + C_1 h + C_2 h^{1/2} + C_3 h^{1/4} + C_4 h^{1/8} + C_4 h^{1/16} \tag{3.12}$$

The contact depth can be obtained by subtracting the contact perimeter, h_s, from the maximum contact depth. The contact perimeter can be obtained using **Eq. 3.11**. A schematic is provided in **Fig. 27** that show the physical meaning of many of these parameters.

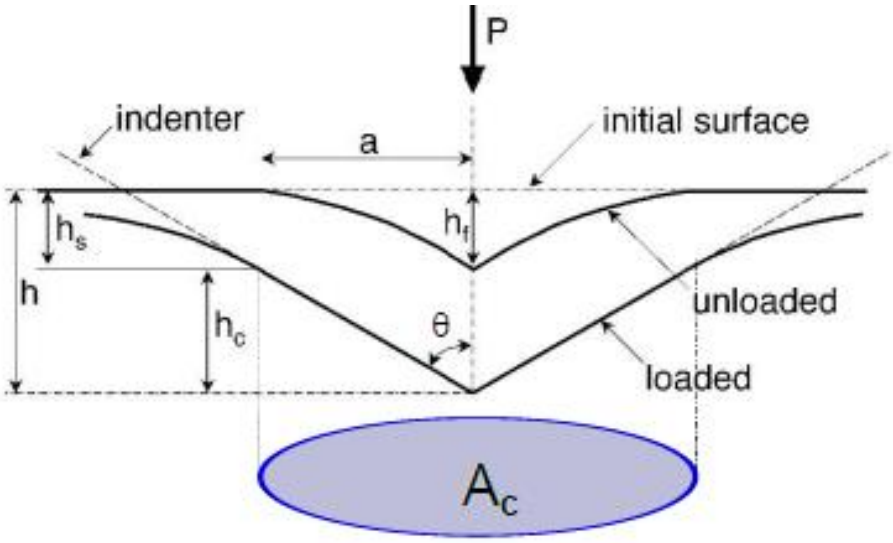

Figure 27 – Schematic of the tip penetration the sample under a specific indentation load; several parameters used to obtain the mechanical properties are listed (Zhang et al., 2014).

While some authors have directly used the Poisson's ratio of 0.3 for modulus calculation (Kumar et al., 2012), the elastic modulus in this thesis will be displayed as a function of Poisson's ratio, thereby classifying the reduced modulus values as indentation elastic modulus instead (**Eq. 3.13**). The reduced modulus can be written has a function of Poisson's ratio and modulus of both the specimen and the diamond tip.

$$\frac{1}{E_r} = \frac{(1-\nu^2)}{E} + \frac{(1-{\nu_i}^2)}{E_i} \tag{3.13}$$

In **Eq. 3.13**, ν_i and E_i are the Poisson's ratio and indentation elastic modulus of the diamond tip (0.07 and 1141 GPa, respectively). The indentation elastic modulus can also be represented by the plane-stress elastic moduli (**Eq. 3.14**), where *K* is the bulk

modulus and *G* is the shear modulus. The derivation of the transfer from the plane-stress elastic moduli equation to the plane-stress elastic moduli equation is shown in **Appendix A**. This equation can only be used for isotropic materials. However, given that shales are transversely isotropic materials, the indentation modulus can be obtained using **Eq. 3.15 and 3.16**, where the elastic constants ($C_{11}, C_{12}, C_{13}, C_{33}, and\ C_{44}$) are the five constants that define the material. In Voigt notation, these constant can be written as $C_{1111}, C_{1122}, C_{1333},\ C_{3333}, and\ C_{44} = C_{1313} = C_{2323}$) (Delafargue and Ulm, 2004).

$$M = \frac{E}{(1-v^2)} = 4G\frac{3K+G}{3K+4G} \tag{3.14}$$

$$M_3 \approx 2\sqrt{\frac{C_{11}C_{33}-C_{13}^2}{C_{11}}\left(\frac{1}{C_{44}} + \frac{2}{\sqrt{C_{11}C_{33}+C_{13}}}\right)^{-1}} \tag{3.15}$$

$$M_1 \approx \sqrt{\sqrt{\frac{C_{11}}{C_{33}}}\frac{C_{11}^2-C_{12}^2}{C_{11}}M_3} \tag{3.16}$$

3.3.3 Indentation hardness

The hardness, as determined by Oliver and Pharr, can be calculated using the projected contact area and the average pressure, P_{max}, applied onto the probe (**Eq. 3.17**).

$$H = \frac{P_{max}}{A_C} \tag{3.17}$$

It is understood that indentation hardness is not a property of a material. Accuracy of the results are primarily dependent on the contact area, the derivation of which is provided in the previous section.

3.3.4 Contact creep modulus

In measuring the indentation modulus and hardness using nanoindentation, the tip is held in contact with the sample for 10 seconds. The load and uploaded phases are also 10 seconds, which are fast enough to minimize the effect of plasticity during loading and viscous effects during loading and unloading (Vandamme and Ulm, 2013). When measuring creep of the heterogeneous sample, a hold time of 200 seconds is used.

There are several means of describing the behavior of viscoelastic materials. One such method is called the integral operator (also called the hereditary Integral) (**Eq. 3.18**). When a linear viscoelastic material is loaded over positive time (t>0) in a triaxial creep experiment, the output strain response can be described through this integral form. In other words, the strain $\varepsilon(t)$ can be described at time, t, using the integral equation.

$$\varepsilon(t) = \int_0^t J(t-\tau)\frac{d\sigma(\tau)}{d\tau}d\tau \tag{3.18}$$

τ represents any time between 0 and t. $J(t)$ is the creep compliance function that characterizes the time-dependent strain response to sudden loading and is a memory

function. By performing creep indentation tests, the contact creep compliance, can be used to characterize the creep properties of the material.

The Galin-sneddon solution, a widely used method for indentation of isotropic materials, is presented in **Eq. 3.19**. $P(t)$ represents the indentation load, $h(t)$ is the indentation depth, where both are a function of time. θ represents the half-angle of the conical indenter and M represents the indentation modulus. The indentation modulus is presented in **Eq. 3.12**.

$$P(t) = \frac{2\tan\theta}{\pi} M h^2(t) \tag{3.19}$$

The correspondence principle of linear viscoelasticity is a well-established method for solving boundary value problems involving viscoelastic materials. Here, the time-dependent elastic field variables and constitutive properties are replaced by the s-multiplied Laplace transform analogs, solved in the Laplace domain, and then translated back to the time domain. Proven by Lee and Radoc (1960), this principle can be applied as long as the contact area between the indenter probe and the indented material is increasing monotonically. Applying this principle to **Eq. 3.19** results in **Eq. 3.20**.

$$\overline{P(s)} = \frac{2\tan\theta}{\pi} s\overline{M(s)}\overline{h^2(s)} = \frac{2\tan\theta}{\pi}\frac{\overline{h^2(s)}}{s\bar{L}\overline{(s)}} \tag{3.20}$$

Creep indentation experiments can be approximated by a Heaviside step loading (**Eq. 3.21**).

$$P(t) = P_{max}H(t) \tag{3.21}$$

where $P_{\max}$ is the maximum applied load and $H(t)$ is the Heaviside step function.

The overbar in **Eq. 3.20** represents the Laplace transformed quantity and s the Laplace parameter. $L(t)$ is the contact creep compliance, which can be rewritten in the laplace domain as $s\overline{L(s)} = \frac{1}{s\overline{M(s)}}$ (Vandamme et al., 2012; Vandamme and Ulm, 2013; Zhang et al., 2014).

Vandamme and Ulm (2013) showed that the contact creep compliance rate $\dot{L}(t)$ can be obtained during the holding phase of the nanoindentation creep experiment (**Eq. 3.22**), as presented in **Eq. 2.8**, whose derivative with respect to time is shown in **Eq. 3.23** (also presented in **Eq. 2.9**) (Zhang, et al., 2014). At time zero, which corresponds to the start of the holding period, the contact creep compliance is $\frac{1}{M}$. Hence, the equation can be re-written to include the inverse of the indentation modulus (**Eq. 3.24**) and fit with a logarithmic function (Zhang et al., 2014).

$$\dot{L}(t) = \frac{2a_u\dot{h}(t)}{P_{\max}} \tag{3.22}$$

$$L(t) - L(0) = L(t) - \frac{1}{M} = \frac{2a_u\Delta h(t)}{P_{max}} \tag{3.23}$$

$$L(t) - \frac{1}{M} = \frac{\ln(\frac{t}{\tau} + 1)}{C} \tag{3.24}$$

The contact creep modulus, C, represents the creep kinetics, where the greater the contact creep modulus, the lower the creep rate of the material. The characteristic time τ specifies

the time at which creep kinetics starts showing a logarithmic behavior. The rate of this long-term creep kinetics can be can be captured by the contact creep modulus (**3.25**).

$$\dot{L}(t) = \frac{1}{Ct}; \quad t \gg \tau \tag{3.25}$$

3.3.5 Standard transducer, NanoDMA III transdsucer, and experimental parameters

The Hysitron TI950 nanoindenter was used to extract the indentation modulus, indentation hardness, and creep properties of the Haynesville shale samples studied in this thesis. Specifically, the 2-D transducer was used to measure the indentation modulus and indentation hardness whereas the nanoDMA III transducer was used to measure the time-dependent (creep) properties. The nanoDMA III transducer, a dynamic testing technique, was designed by Hysitron® to measure time dependent properties that are not easily measured through standard techniques (Hysitron nanoDMA III User Manual, 2014). The Hysitron TI-950 nanoindenter located at the Texas A&M Materials Characterization (MCF) facility was used for all experiments performed in this study. Calibration of the nanoindenter was performed on fused quartz and polycarbonate to ensure that the tip, optics, and stage were calibrated correctly. A Nano-DMA III transducer was used instead of a 2D transducer to measure the creep behavior because of its reduced sensitivity to drift. Experiments at ambient conditions utilized a short-duration Berkovich tip while experiments at high temperatures required an extended temperature tip. The extension of the tip is required to account for the thickness of the temperature stage. An image of the short-duration and high temperature tip are shown in **Fig. 28**.

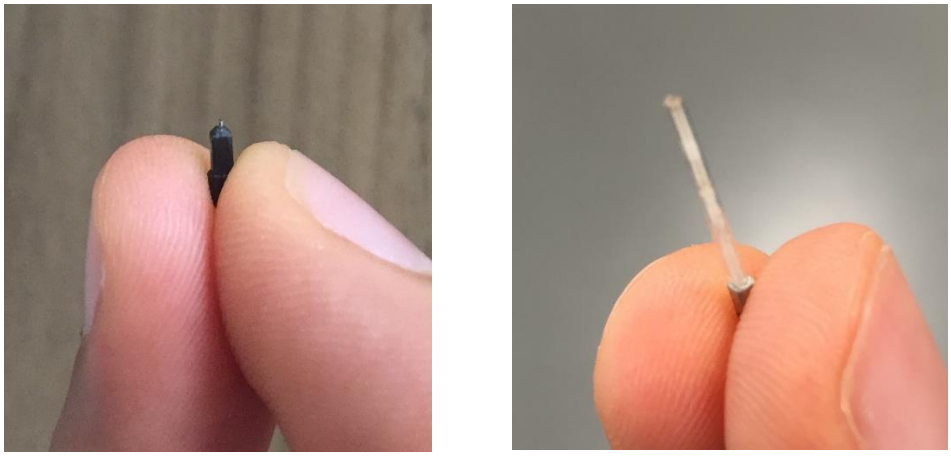

Figure 28 – Short-duration tip (left) and high temperature tip (right) used for indenting samples.

Indentation settings are highly dependent on the material being examined. Wang et al., (2009) used load settings between 1-9mN for nanocrystalline nickel. In the case for shales, Kumar et al., (2013) used a load of 300-500mN for nanoindentation of Woodford samples. In a large scale indentation campaign, Bobko and Ulm (2008) experimented with a range of applied loads between P = 0.3mN and 4.8mN; at a constant loading rate of 0.3 mN, the indentation depths were between 250-500nm and a load of 4.8mN resulted in depths between 0.5-2.5μm, the latter producing more stable mechanical properties. Bobko and Ulm (2008) proposed nanoindentation parameters (with the exception of creep holding time) listed in **Table 8** to capture the mechanical properties of materials with length scales between 0.5 to 3μm which is particularly useful for understanding the mechanical responses of porous clays. In an attempt to capture accurate mechanical properties of porous clay in the X1 and X3 bedding directions, load conditions listed in **Table 8** are applied for all experiments performed in this study. Each experiment consisted of 400-625 indents (20x20 or 25x25 matrix) covering approximately 140μmx140μm to

175μmx175μm of the sample surface. Test runs were made on Haynesville, Marcellus, and Eagle Ford samples on the nanoindenter and the results were validated to ensure the surface polishing protocol was adequate for correct data extraction. A representation of the indentation grid is shown in **Fig. 29**.

Table 8 – Nanoindentation settings for measuring the mechanical properties of clays in shales (Bobko and Ulm, 2007; Abedi et. al., 2015).

Nanoindentation Load Settings	
Applied Load (μN)	4800
Loading Time (sec)	10
Unloading Time (sec)	10
Short-duration Holding Time (sec)	10
Creep Holding Time (sec)	200
Spacing (μN)	7

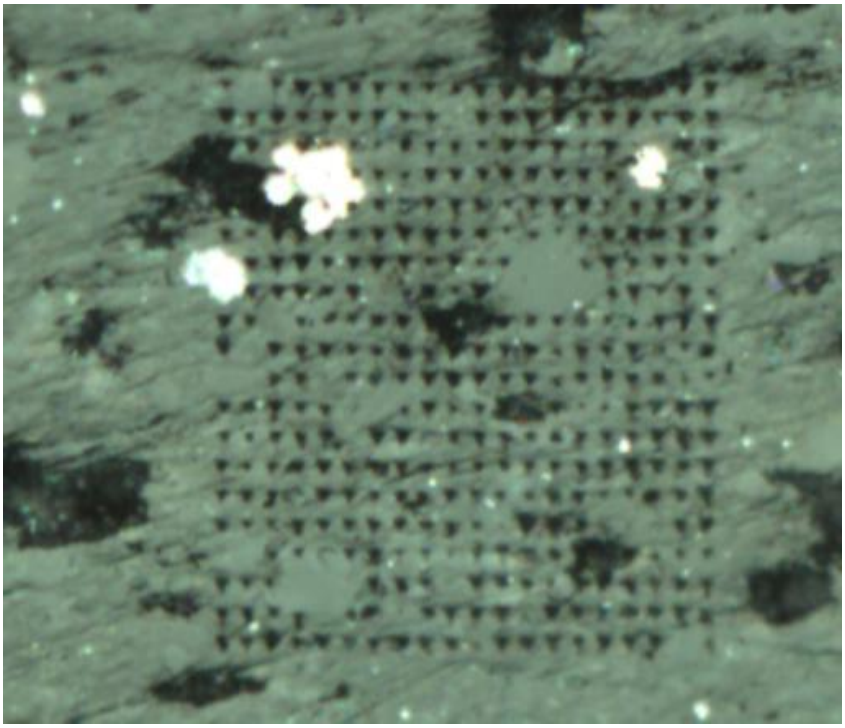

Figure 29 – Indentation grid (20x20) performed using nanoindentation using the parameters listed in Table 8.

3.3.6 Loading or replacing the diamond tip

Replacing the tip on the transducer is a delicate process and should be performed carefully so as to avoid damage to the probe. To replace the diamond tip,

1. Unplug the three transducer/scanner cords from the system, loosen the hex screw, remove the transducer/scanner from the nanoindenter, and place on a flat surface.
2. Carefully remove the standard berkovich probe from the transducer using one of two nanoindentation tip mounting tools. The short tool is for the berkovich probe and the long tool is for the high temperature berkovich probe (**Fig. 30**).

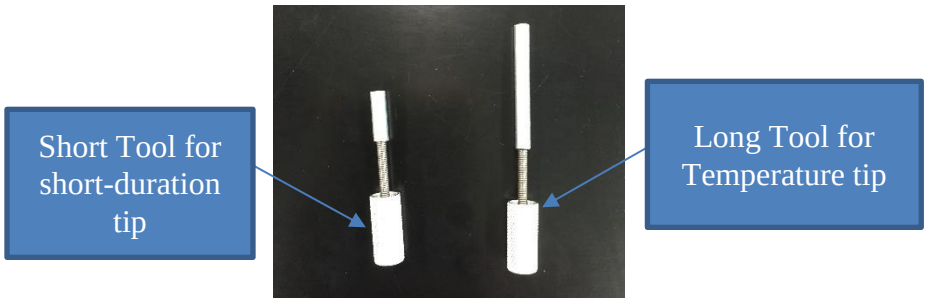

Figure 30 – Small tool (left) and large tool (right) for replacing the short-duration and high temperature tips, respectively.

3. When unscrewing the tip, carefully place the tool over the tip with minimal lateral movement and loosen in a counter-clockwise manner until the tip is completely removed from the transducer socket.
4. Once removed, place the tip back into the plastic tube and store carefully.
5. Next, remove the high temperature tip carefully from the storage container and remove the tip from the plastic tube. Note that when storing the tip in the plastic tube, the tip should be inserted into the tube without force; the metallic portion of

the tip should be partially inserted into the plastic tube. This is to prevent damage to the tip shaft.

6. Insert the tip into the long mounting tool and carefully place the end of the tip into the transducer socket. Rotate the tool in a counter-clockwise manner until a "click" is heard, then tighten in the clockwise direction. Rotate the tool an additional quarter circle once the tip is fully tightened.
7. Load the transducer back onto the nanoindenter machine, tighten the hex screw, and connect all wires.
8. Load the correct area function by going to Calibration > Tip calibration > File. Make sure to choose the correct slot when loading the area function.

3.3.7 Tip to optics calibration

Tip to optics calibration is performed when the transducer has been removed and needs to be aligned with the optical microscope. Tip to optics calibration should be performed on a soft sample, such as Aluminum or Polycarbonate. To perform tip to optics calibration, the following method should be used:

1. Create a boundary on the standard sample (Aluminum or Polycarbonate)
2. Go to Calibration > Stage Calibration > Tip to Optics Calibration. Create an "H-pattern" on the sample.
3. Once complete, place the optical microscope on the center indent of the "H-pattern" and indent once more to complete the calibration.

3.3.8 Air indent calibration

Air indent calibration is performed to confirm that the tip is free of foreign debris. To perform air indent calibration, the following method should be used:

1. Calibration > Systems Calibration > Indentation Axis > Calibrate > Air Indent
2. When running the test, make sure that the vibration isolation control unit is turned on.

Note: air indent calibration is not necessary when performing tip to optics calibration.

If the air indent is unsuccessful, confirm that the tip is clean, placed correctly into the transducer slot, and that the scanner screw is tightened completely.

3.3.9 Cleaning the tip and standard sample

Cleaning the tip and standing sample is one of the most important and crucial steps in performing a proper experiment. To clean the tip, use a cotton swap and acetone and wipe the tip from top to bottom (**Fig. 31**). Do not place the cotton swab directly onto the end of the shaft as it can damage the tip. Once the tip has been cleaned with acetone, gently blow compressed nitrogen along the shaft to evaporate the excess liquid. The tip can also be cleaned using an ultra-sonic water bath, though this cleaning procedure was not following in this thesis.

To clean the standard sample, such as fused quartz, the following steps should be used:

1. Blow compressed nitrogen onto the sample to remove large particles

2. Wet a cotton swap with acetone and gently rub the wet swap over the sample. Start in the middle and circle outwards to remove maximum amount of debris.
3. Use the compressed nitrogen and blow the surface to remove excess fluid.
4. Repeat steps 2-3 three times for best results.

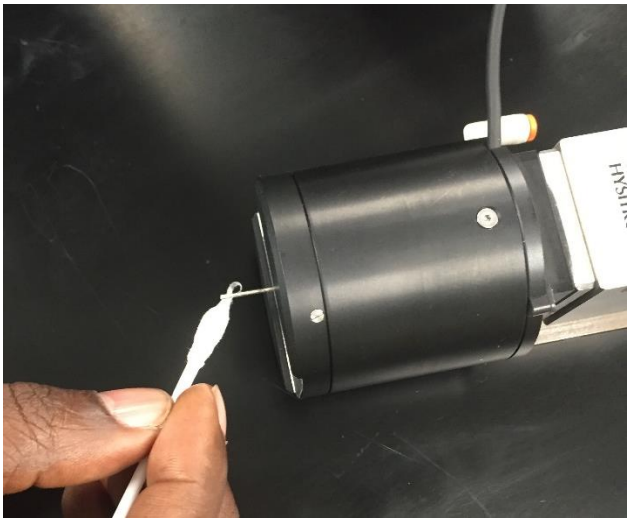

Figure 31 – Cleaning a high temperature tip using a cotton swab and acetone.

3.3.10 Tip calibration

To confirm that the tip produces accurate results, standard sample calibration should be performed before and after each experiment. Fused quartz has a modulus and hardness of 69.6 GPa and 9.25 Gpa, respectively. A short test of 6-9 indents should be performed over a range of loads. Typical loads used were between 4,000 and 10,000mN. If scatter in the results is detected, it may likely be due to excess drift, in which case, the sample should be placed carefully inside the nanoindenter chamber for 20 minutes before beginning the test. A tip calibration is important because each berkovich tip, which is

similar in shape, has its own unique shape. To account for the particular shape of the tip, an area function is obtained as shown in **Eq. 3.26**.

$$A = C_o h^2 + C_1 h + C_2 h^{1/2} + C_3 h^{1/4} + C_4 h^{1/8} + C_4 h^{1/16} \quad (3.26)$$

3.3.11 Indentation at elevated temperatures

In this study, the Hysitron® TI-950 nanoindenter equipped with a dual XSol temperature stage (max temperature of 800°C) was used to perform indentations at elevated temperatures. The upper and lower temperature stages contain heating elements that maintain a uniform temperature gradient throughout the sample (**Fig. 32**). The temperature stage comes equipped with a dry gas shroud connected to a dry gas source (argon) to prevent condensation on the sample when it is cooled to room temperature. The argon gas also helps reduce the occurrence of oxidation of the diamond tip and the sample, the latter being a key condition needed to replicate in-situ conditions.

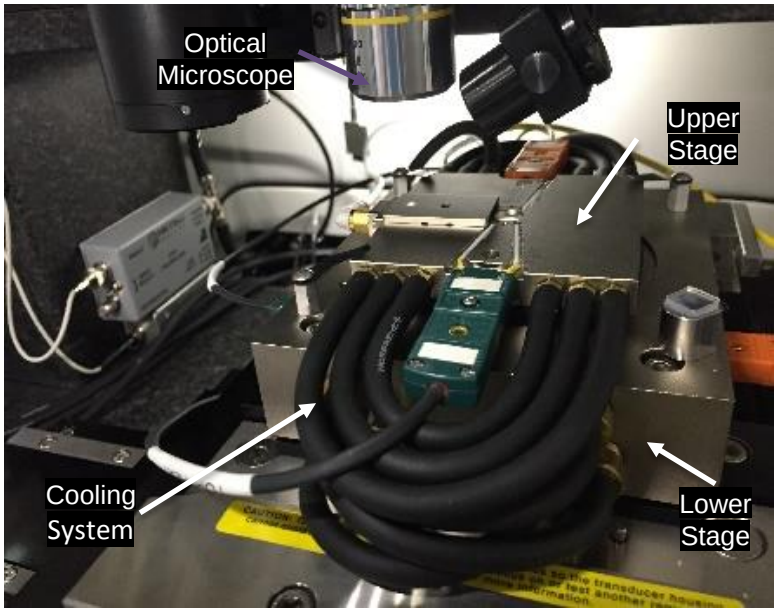

Figure 32 – A Hysitron TI950 Nanoindenter temperature stage assembly (upper stage and lower stage) connected to a cooling system used to heat the sample and maintain a uniform temperature around the stage.

The temperature of the top and bottom stages are measured in real time by the stage sensors and stored by the computer software. The stage can be programmed to heat the sample instantly or at a constant rate. A plot of temperature versus time (**Fig. 33**) shows that allowing the sample to heat at a constant rate reduces the chance of exceeding the pre-set temperature value. Moreover, since the goal of this investigation is to characterize the effect of exposure to high temperatures on mechanical properties of organic-rich shales, the heating procedure needs to be designed to limit the corresponding thermal gradients and transient effects of heating. Therefore, specimens were heated at a rate of 1°C/min. using the constant rate method, also known as the "ramp" feature.

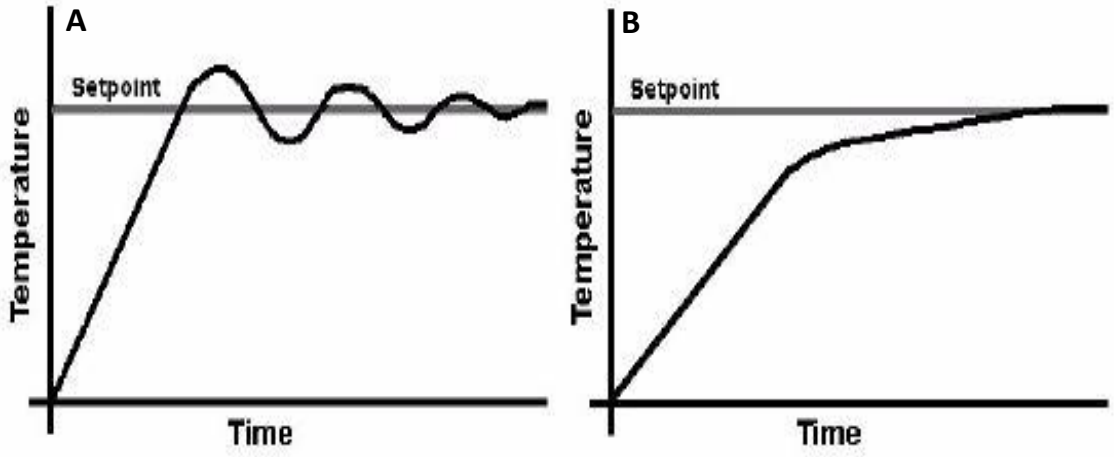

Figure 33 – Increasing the stage temperature before (left, A) and after (right, B) selecting the "ramp" feature (modified from Hysitron Temperature Stage Controls manual, 2014).

There are two major types of drifts to consider when performing indents, especially at higher temperatures. The first is electrical drift and the second is thermal drift. Electrical drift is caused by the motors and sensors connected to the stage and tip assemblies (Lu et al., 2010). Thermal drift occurs when the components of the system, such as the motors, release heat into the surrounding and cause temperature fluctuations in the system. Engineers and researchers have attempted to eliminate thermal drift by increasing the amount of "dwell" time between the tip and sample during indentation. In the case of the nanoindenter, it was observed that a dwell time of 45 seconds is automatically programmed in each indentation cycle to allow for the drift to stabilize. While 45 seconds may not entirely eliminate this issue, this hold time allows the drift for most indents to fall within the desired drift limit (+/- 0.05 nm/s). **Table 9** lists the percent of indents that fell

within the drift limit for all short-duration indentation tests (23-350°C), and **Fig. 34** shows the average drift rate for each experiment.

Table 9 – Temperature dependence on drift rate for short-duration indentation experiments performed between 23-350°C.

Temperature (°C)	% of Indents within the Drift Rate (=<-0.05 nm/s)
X1-23 (Set 1)	100
X1-23 (Set 2)	99
X1-70	98
X1-250	83
X1-350	97
X3-23	67
X3-250 (Set 1)	86
X3-250 (Set 2)	71
X3-350 (Set 1)	85
X3-350 (Set 2)	99

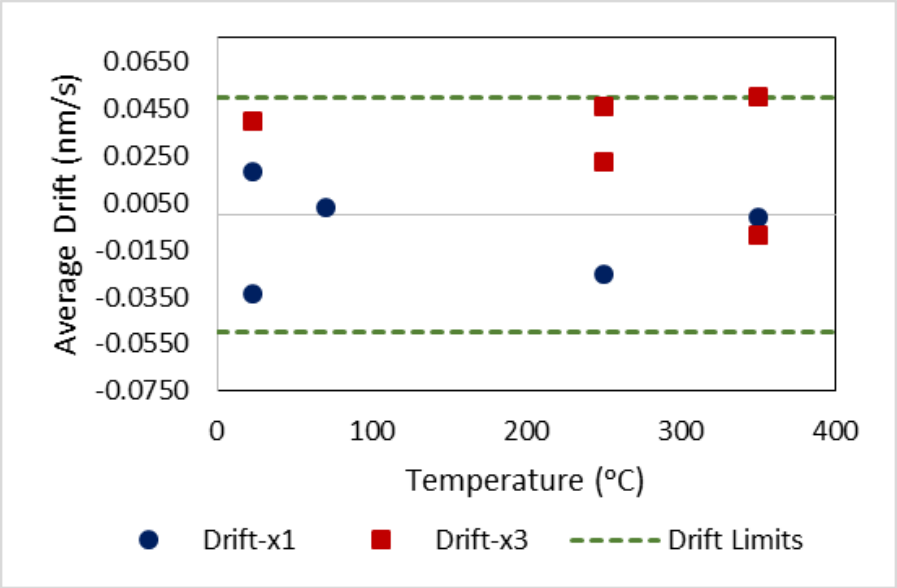

Figure 34 – Average drift rate (nm/s) over a range of temperatures.

To reduce the amount of error in indentation measurements, careful attention should be placed to ensure that the tip and sample are at the same temperature. A tip at room temperature coming into contact with the heated sample can cause incorrect mechanical property measurements. In addition, it is necessary to consider the specific environment that the nanoindenter is placed in. As a result, an equilibrium time of ~4 hours was allotted for any unforeseen causes affecting the system's steady-state rate. During heating and equilibrium time, the tip is brought into contact with the sample and then retracted 0.05μm to account for sample expansion. Grebowicz (2014) recorded the thermal expansion of green river shales and determined that between 100-210°C, the sample expanded linearly and by 4.3% in dimension up to 350°C. While it is unclear whether significant sample expansion occurs during the heating process in our experiments, precaution was taken by retracting the tip during all temperature experiments to avoid damage to the tip or the sample. To monitor the sample expansion, images of the sample surface were taken on the nanoindenter before and after the thermal equilibrium had been achieved. **Fig. 35** shows a comparison of the Haynesville sample surface before and after heating it to 350°C. To achieve a higher level of clarity in the second image, the magnification needed to be reduced slightly. Two conclusions can be drawn from these images. The first is that the sample may have expanded due to an increase in temperature. Further investigation is needed to determine whether dilatation occurs in the sample and the amount of time needed to heat the sample before expansion levels off. The second conclusion is that the magnification needed to be changed due to the interference with heat

waves. No major changes were made to the experimental procedure to account for sample expansion.

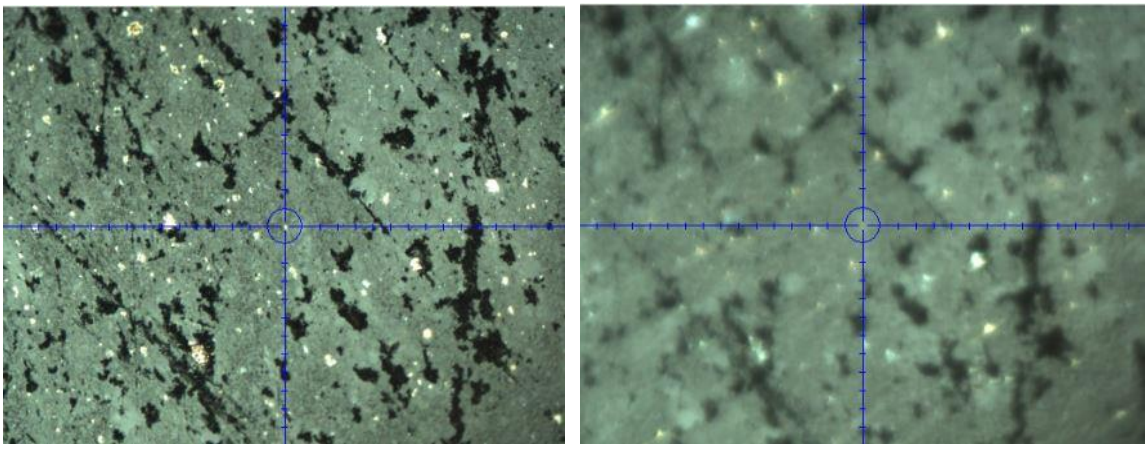

Figure 35 – Optical image of an X1-direction Haynesville sample before (left) and after (right) heating to 350°C.

3.4 SEM and EDX

Scanning Electron Microscope was used to obtain high-resolution topographic images of sample surfaces and is commonly used to study the pore network present within organic-rich shales (Loucks et al., 2009). The scanning electron microscope has four main components: the electron gun, electron lenses (both of which make up the "column"), a vacuum system, and a specimen stage (Reed). The electron gun is composed of a tungsten filament closely set to a cathode and an anode that helps control the flow of electrons from the filament and onto the sample surface. The electron lenses help project the electrons onto the surface of the sample. The lens, which are composed of an iron shroud and copper windings, consist of a small window opening that allows the beam to deflect towards the axis. A total of three lenses (two condensers and one immersion lens) are used to redirect

the electron beam towards the sample surface. A low pressure environment is created to prevent damage to the electron source and high-voltage breakdown in the gun. The vacuum also allows the electrons to reach the surface directly, rather than dispersing around the sample. When electrons reach the surface of the sample, the behavior of the electrons are categorized into two groups: inelastic and elastic electrons. Elastic electrons, also known as secondary electrons, are electrons with energies less than 50eV, and reflect at an angle less than 90°. See **Fig. 36** for a cross-sectional illustration. These electrons are captured by a detector such as the Everhart-Thornley type detector. Inelastic electrons, also known as back-scattered electrons, have energies greater than 50eV and reflect at an angle greater than 90° thereby analyzing a deeper portion of the sample surface. These electrons are captured by a detector typically placed directly above the specimen.

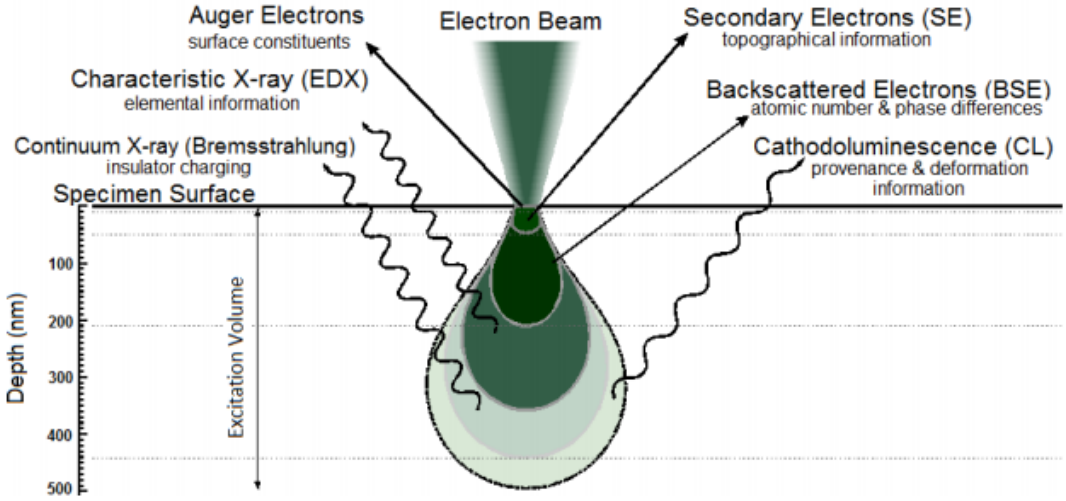

Figure 36 – Cross-section illustration of the depth at which secondary electrons and back-scattered electrons penetrate the sample surface (taken from Ads, et. al., 2014).

Energy Dispersive X-Ray Spectroscopy (EDS or EDX) was used in conjunction with an SEM to help acquire quantitative and qualitative chemical information of the imaged surface. All results were obtained using a LYRA FIB-SEM, equipped with a standard EDX Microanalysis System, located at the Texas A&M MCF facility or an Electron Microprobe, paired with a Thermo EDS System (**Fig. 37**), located at the Texas A&M Microscopy and Imaging Center. Electrons bombarded onto the sample surface cause electrons to be ejected from the atoms. X-rays are emitted as a consequence of the transferring of electrons from a higher state to a lower stage and are captured by the EDX detector for processing; EDX is reflective of the energy level of the x-rays emitted from the sample surface.

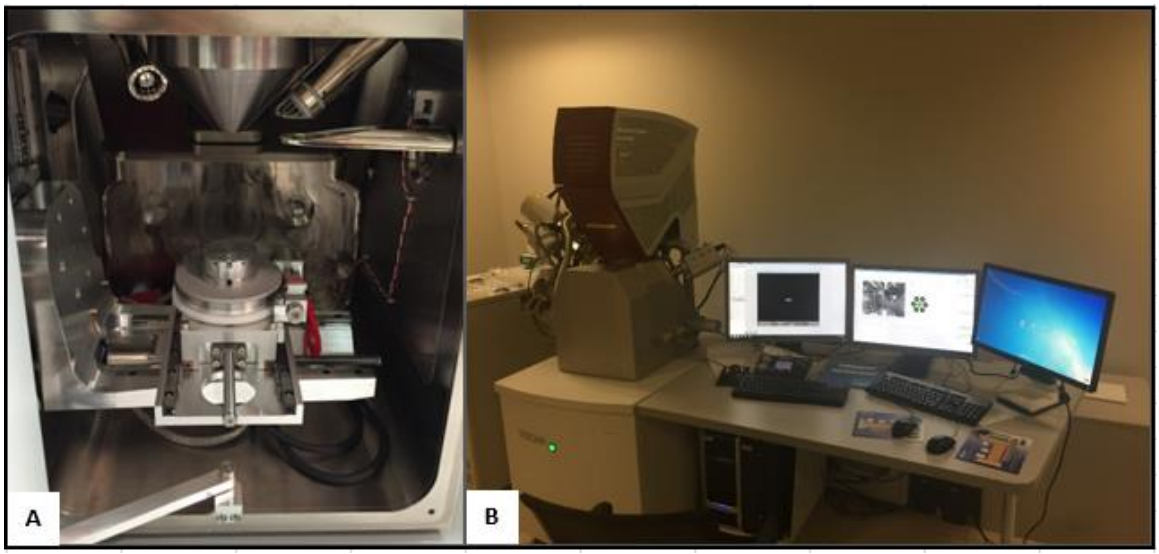

Figure 37 – Chamber view of a Lyra FIB-SEM machine (left) and SEM/EDX work station (right) located at the Microscopy Imaging Center (Texas A&M University).

Processing of the x-rays versus counts is needed to determine the elemental composition of the imaged surface. An accelerating voltage of 15kV and a working distance of 9mm were used to obtain topographical and compositional images of the nanoindentation grids. Qualitative data was extracted for elements of interest: Si, Al, and Ca. Other elemental maps were also obtained (C, Fe, K, Mg, Na, O, P, and S) but were typically not included in the analytical approach to study the porous clay/kerogen phase. Next, the quantitative results for Si and Al were extracted to identify the clay/kerogen phase (Deirieh et al., 2012, Abedi et al., 2015, and Slim et al., 2017). Qualitative results were extracted from the software in the form of .tiff files, which provide the intensity values for each pixel. For example, a typical image resolution obtained was 512x351; the .tiff file would correspond to 512X351 columns and rows of numerical data which can be imported into another program (Matlab) for analysis. The elemental maps are shown in **Fig. 38.**

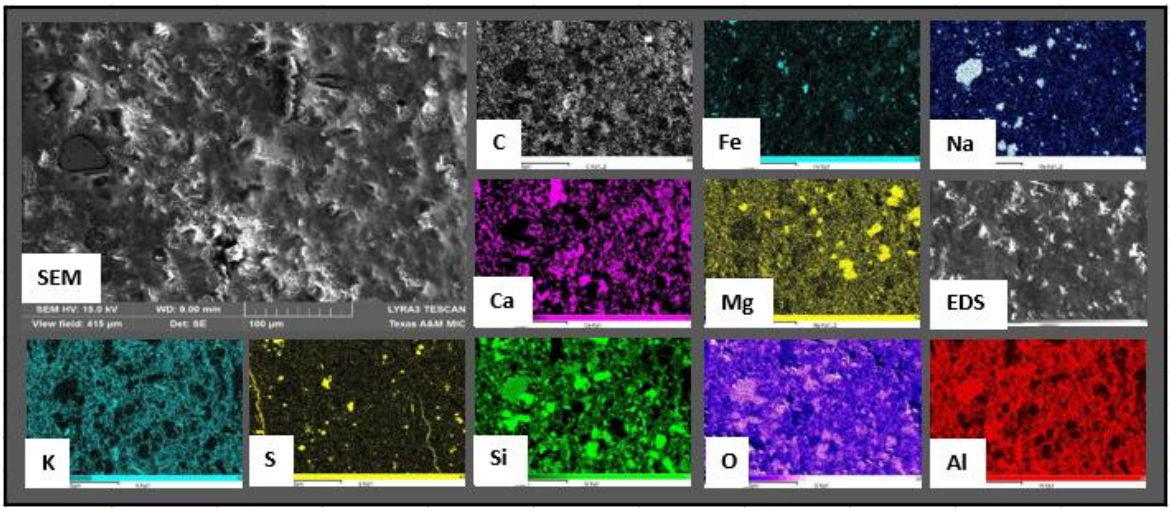

Figure 38 – Topographic and elemental images of a Haynesville shale sample (X1, parallel) for a sample tested at 250°C (on the nanoindenter) using the Lyra FIB-SEM.

Samples under investigation were carbon coated (20nm) to prevent electron charge buildup during imaging. All samples were carbon coated using the carbon coating machine located at the Texas A&M MIC facility.

3.5 Coupling nanoindentation and EDX results

With the extraction of mechanical properties from nanoindentation and chemical properties from SEM/EDX, coupling analysis is performed to determine the averaged chemical intensity values around each indentation point; these quantitative values are needed to implement a chemo-mechanical clustering approach, as will be discussed in the next section. First, determine the elements of interest. Second, using a programming platform (Matlab), the pixel location of the four corners of the indentation grid need to be obtained. Next, using the x-value and y-value of each indent (provided by the Hysitron

software) and knowing that the spacing of each indent is 7μm, we determine the pixel locations of each indent. Fourth, an averaged intensity value is extracted for all visible indents within each elemental map. Given that our focus is to primarily understand the behavior of indented clay phase, average (1μm radius) intensity values are obtained for each indent for both aluminum (Al) and silicon (Si); depending on the concentration of calcium and type of clay present within the imaged area, the calcium (Ca) and/or potassium (K) intensity values were also obtained. As a result, for each indentation modulus, indentation hardness, and contact creep modulus value exists an averaged silicon and aluminum intensity value. In cases where dolomite concentrations were relatively high, the magnesium (Mg) intensity values were also obtained to help better differentiate the soft components (clays) from the hard components (carbonates) in this model-based clustering analysis.

An example of the output of this analysis is shown in **Fig. 39**. Though indentations are not visible on the elemental maps, these images show the locations at which the sample was indented; indents are visible on the SEM images and are used as reference to overlay the indents on elemental maps. **Table 10** lists the mechanical properties (elastic and strength) with the corresponding elemental intensity values for calcium, aluminum, silicon, and potassium for the first five indents (starting from bottom left of grid and to the right) for one grid.

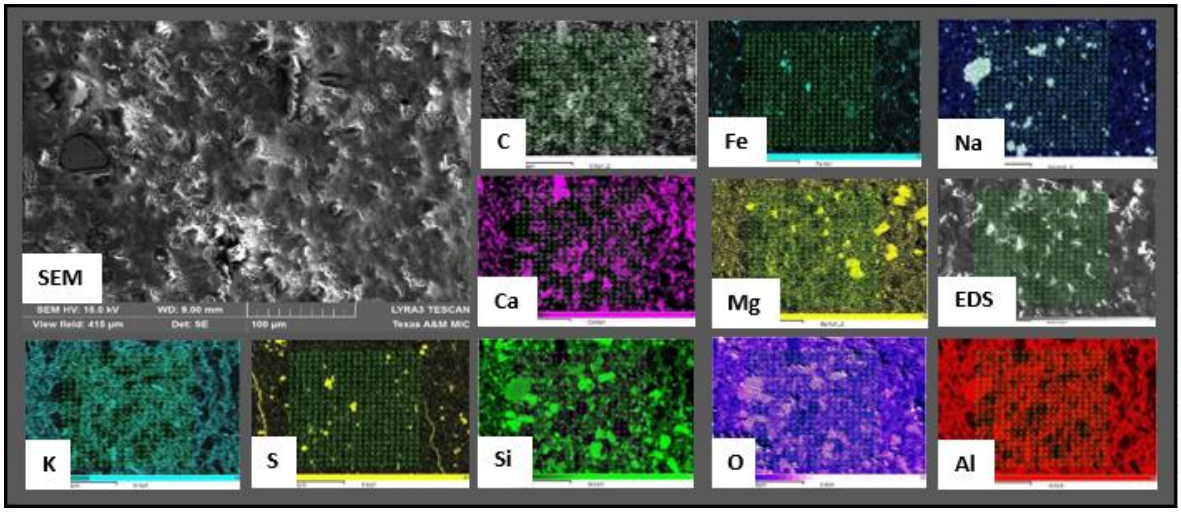

Figure 39 – SEM and elemental maps with overlapped indents for Haynesville (X1-250°C).

Table 10 – Summary of the mechanical and elemental intensity values for X1-250°C.

Haynesville X1-250°C							
Points	Reduced Modulus (GPa)	Indentation Modulus (GPa) $\frac{E}{1-\nu^2}$	Hardness (GPa)	Averaged Intensity (1μm Radius)			
				Ca	Al	Si	K
1	45.30	47.17	0.725	1.7	4.2	12.9	1
2	23.51	24.00	0.187	5.1	5.0	7.7	1.4
3	29.47	30.25	0.509	2.0	4.6	16.8	1.5
4	13.25	13.40	0.093	3.5	4.3	6.3	0.6
5	32.42	33.37	0.309	7.6	2.5	5.4	0.9

3.6 Model-based clustering for chemo-mechanical characterization

To evaluate the experimental results obtained from nanoindentation and SEM/EDX mapping, the mechanical properties (M, H, C) and chemical intensity values (Si, Al, and Ca or K) are used in conjunction as input parameters to a model-based clustering approach. Such a statistical approach is commonly used to group similar data

points and provide uncertainties associated with each grouped data set (Fraley and Raftery, 2007). Analysis was performed using R programming language with a model-based clustering package (mclust) available through R. The mclust package uses a model-selection criteria called BIC, or Bayesian Information Criterion, to identify and categorize the input parameters based on maximum likelihood (volume, shape, and orientation).

An example of the chemo-mechanical clustered results for X1-23°C experiment are shown in **Fig. 3.21 and 3.22**, where phases 1 through 4 in **Fig. 3.21** correspond to clay-rich (2:1, Si:Al ratio), clay-carbonate interface, carbonate-rich, and quartz rich phases, respectively. The input parameters in evaluating these results are: H, M, Si, and Al. **Fig. 40** shows the intensity values of aluminum and silicon with the corresponding intensity values. In interpreting these results, it is necessary to understand the chemical formula of each mineral present in the sample. For example, quartz has a chemical formula of SiO_2. This corresponds closely to phase 4, which has negligible aluminum and a high value for silicon. Therefore, this phase is classified to represent quartz. The high mechanical properties also prove that this phase correlates with a harder mineral. It is also evident that indentation depth decreases with increasing mechanical properties, confirming that the softest phase (Kerogen/clay phase) has the highest indentation depth.

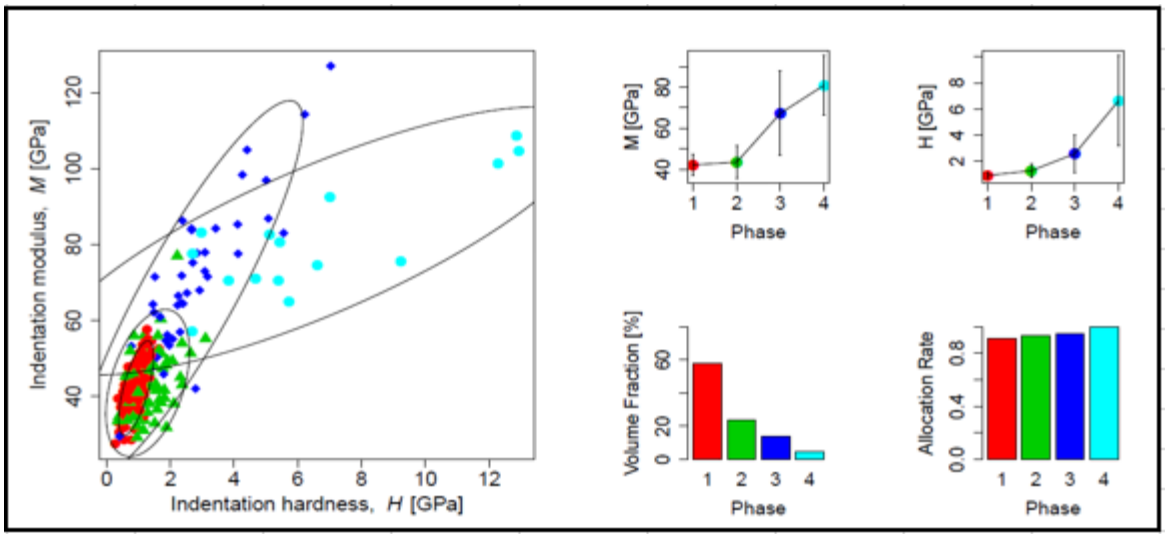

Figure 40 – Chemo-mechanical clustering results for Haynesville shale sample parallel-to-bedding (X1) at room temperature where the indentation modulus, indentation hardness, volume fractions, and allocation rates for each phase are presented.

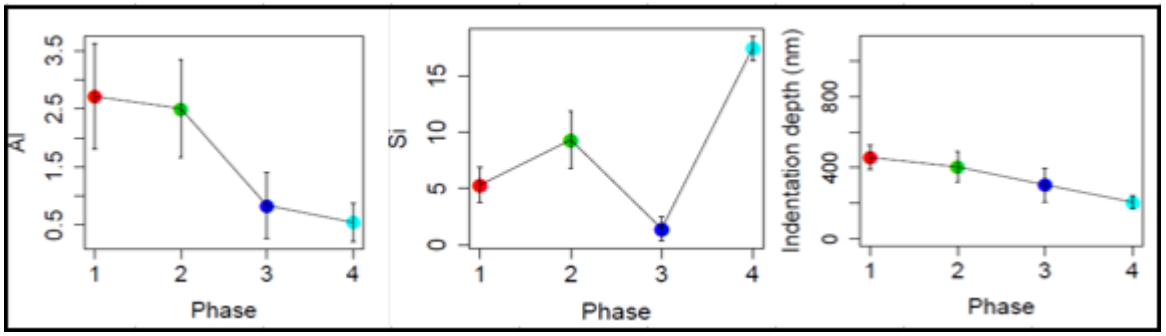

Figure 41 – Chemo-mechanical clustering results for Haynesville shale sample parallel-to-bedding (X1) at room temperature where the average intensity for aluminum and silicon are presented as well as the indentation depths for each phase.

Fig. 41 shows the frequency distribution of each of these phases for both indentation modulus and hardness according to their respective volume fractions. A similar behavior is observed for creep experiments where both indentation modulus and

indentation hardness as well as contact creep modulus increase with decreasing indentation depth. In the case of contact creep modulus, a high modulus value means lower creep kinetics. In other words, quartz has a higher contact creep modulus than clay, but creeps less than clay.

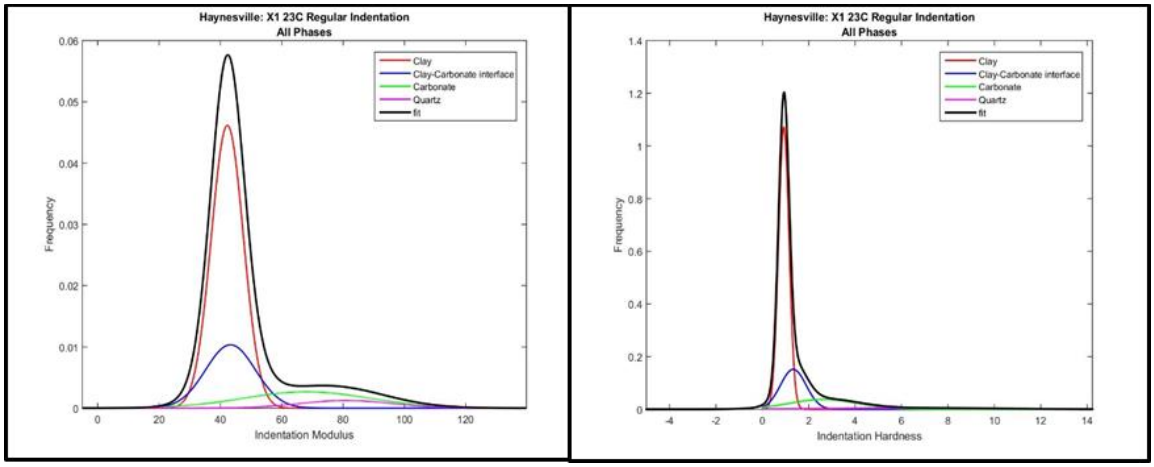

Figure 42 – Indentation modulus (left) and indentation hardness (right) for clustered chemo-mechanical results produced in figures 2-4 plotted based on volume fraction.

Using the coupled and clustered results discussed previously, phase maps are created to validate the accuracy of coupling the qualitative elemental values to the mechanical results obtained from nanoindentation. **Fig. 42** shows the color map of the calculated intensity values for elements Al and Si as well as the estimated location of the indentation grid overlayed on Si and Al elemental maps. Additionally, a phase map (**Fig. 43)** is composed using the model-based clustered results and is compared to both the elemental and color maps for similarities to confirm that the indentation points were selected with high accuracy on the elemental maps. This is of vital importance particularly

for nanoindentation grids performed in the direction perpendicular to bedding plane (X3) where poor polishing is attributed to a higher pore connectivity (Ulm et al., 2005). It is clear that areas that are rich in only silicon correspond to phase 4, which is attributed to quartz (SiO_2). An extensive library of indentation, coupling, clustering, and color map results are included in **Appendix C**.

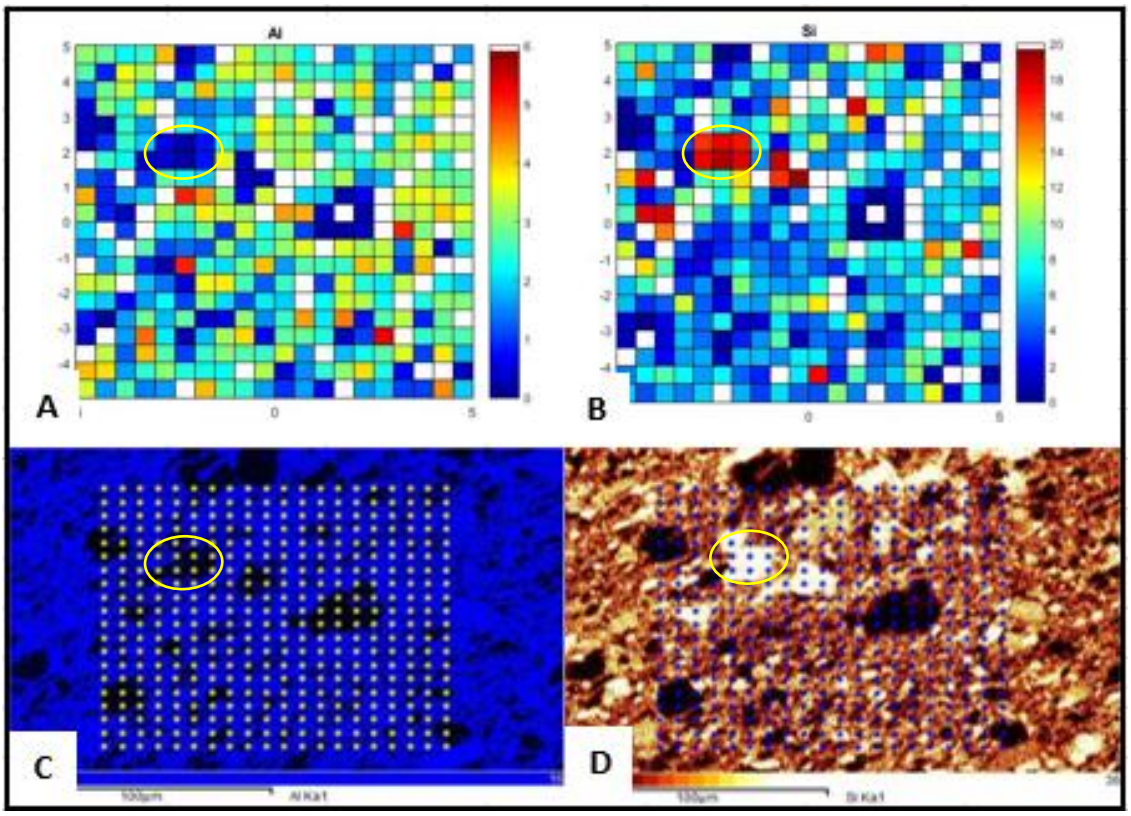

Figure 43 – Color maps (A and B) and elemental maps (C and D) are presented for Aluminum and Silicon on the same area as the nanoindentation grid (Haynesville X1-23°C).

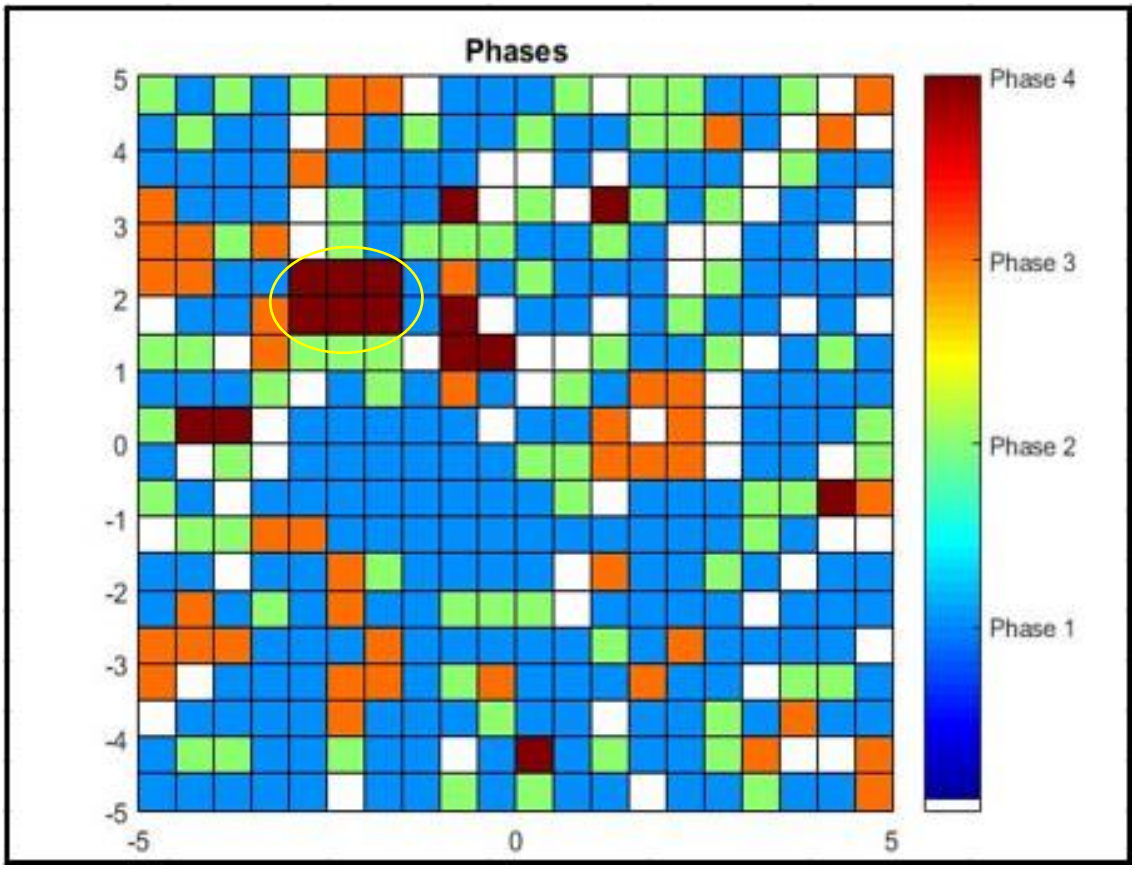

Figure 44 – Phase color map of the clustered results for a nanoindentation grid performed on Haynesville X1-23°C. Comparison of all five maps validate that correct indentation locations were used to couple and cluster the experimental data.

3.7 Chapter summary

This chapter introduced the various ways of analyzing shales samples, ranging from XRD, TOC, Rock Eval, and TGA. Furthermore, calculations are provided for obtaining the volume fraction of clay and kerogen. Next, the theory and experimental procedure to obtain mechanical properties, setting up the equipment, and various calibration methods are presented. Finally, the SEM&EDX results, coupling methodology, and clustering analysis are explained though sample images.

CHAPTER IV

RESULTS AND DISCUSSION

This chapter includes the results and discussions of this work. Initially, discussion of the effect of temperature on the time-independent results for short-duration indentations are reviewed followed by time-independent results obtained from creep experiments. After that, the contact creep modulus for each experimental temperature value is provided and explained in detail. Results from thermogravimetry and its correlation to the outcome of the results is also explained in a separate section. At the end, further evaluation of the experimental data shows particular behavior was performed and are included within. To consolidate all research findings introduced in this chapter, a section is dedicated to the summary of these results in a numbered format.

4.1 Effect of temperature on elasticity and strength properties: short-duration nanoindentation

Nanoindentation tests were performed in both the X1 and X3 directions it measure the time-independent properties, which are indentation modulus and hardness, at 23, 70, 250, and 350°C. These results were coupled with the chemical intensities explained in Chapter III and evaluated using MCLUST. Two elements were used, Si and Al, to determine the presence of clay, though Ca and K were also used based on their concentration within the indented region.

Figs. 45 and 46 show the trend of indentation modulus and hardness at each experimental temperature value. The indentation modulus and hardness values of the

porous clay/kerogen phase shows some variation in mechanical properties; however, the overall trend is relatively stable and suggests that little to no change occurs with increasing temperatures. Emmanuel et al., (2016) performed high temperature studies using Atomic Force Microscope (AFM) to evaluate the behavior of kerogen and bitumen. They also suggested that little change in modulus occurs with increasing temperature values for kerogen. Ibanez and Kronenberg (1993) observed weak temperature dependencies of illite-rich shales between temperatures of 22–196°C. Jarad et al., (2016) showed a negligible variation in effective stress-strain response of compacted illitic clay up to 69.2°C. These observations sheds light on the insensitive nature of the mechanical properties, (kerogen and illite) to high temperatures.

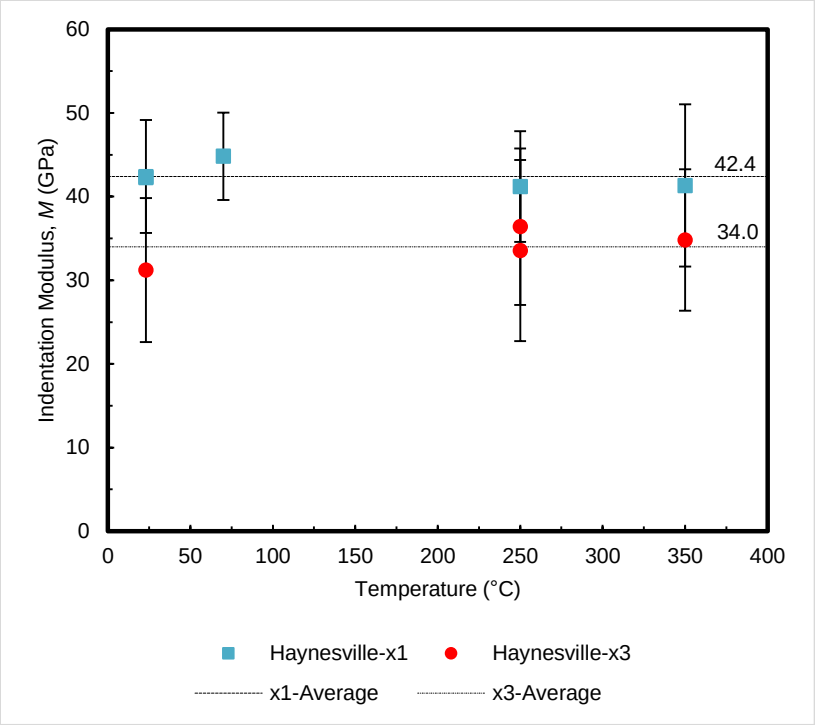

Figure 45 – Indentation modulus obtained from short-duration experiments for Haynesville shale samples parallel and perpendicular to bedding direction for a range of temperatures (23-350°C).

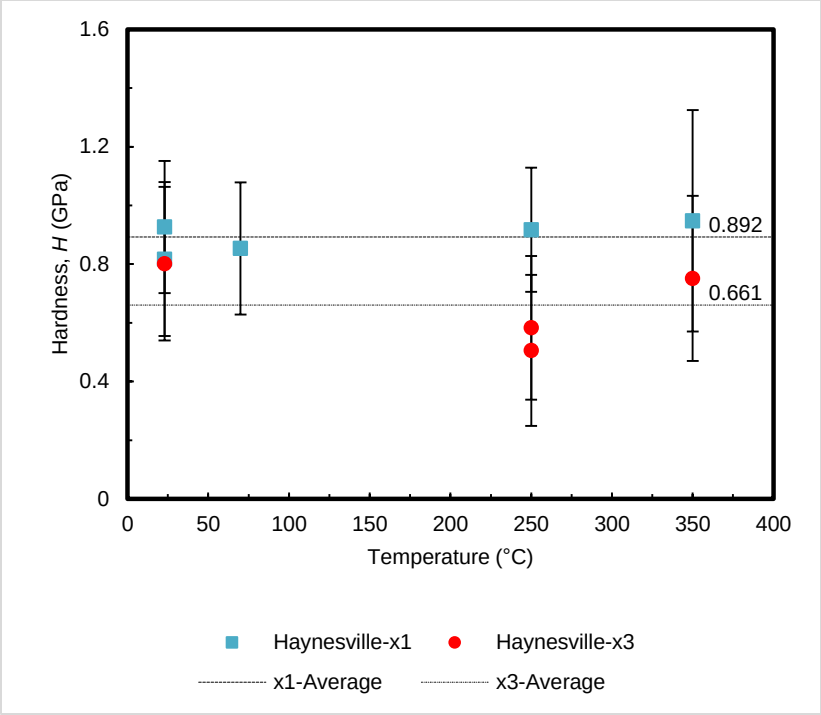

Figure 46 – Indentation hardness obtained from short-duration experiments for Haynesville shale samples parallel and perpendicular to bedding direction for a range of temperatures (23-350°C).

Another reason for negligible change in the mechanical properties of the clay/kerogen phase with increasing temperatures is the ratio between the mechanical properties of kerogen and clay. One of the assumptions made under the self-consistent morphology is that organic matter has negligible modulus and hardness as compared to the inorganic (clay) phase (Abedi, et al., 2016). Furthermore, considering that illite is the main clay constituent and holds significantly less water than other clays such as smectite (discussed in Chapter II), the time-independent properties measured are mostly those of the clay phase. By these two measures, it can be justified that the mechanical properties of the clay/kerogen phase remain unchanged with high temperatures.

Under high temperatures, particularly around 300C, conversion of TOC into hydrocarbons occurs and causes an alteration of the physical properties of organic matter. It has been proved that TOC contains large numbers of pores, often referred to as "organoporosity." While TOC is being converted into hydrocarbons at high temperatures, the formation of new pores, particularly within the organic matter, does not affect the volume fraction of the clay particles within the composite and as a result, no major changes in modulus and hardness are observed during nanoindentation. **Tables 11** lists the various parameters measured and calculated for each of the time-independent experiments.

Table 11 – Haynesville shale results including Indentation Modulus, Indentation Hardness, Silicon, Aluminum, and Si/Al ratio for all short-duration indentation experiments.

Sample	Set	Temperature (°C)	Clay Phase	# of Indents	H (GPa)		M (GPa)		h (nm)		Si		Al		Si/Al
					Mean	Std. Dev.	Mean	Std. Dev.	Mean	Std. Dev.	Mean	Std. Dev.	Mean	Std. Dev.	
Hay-x1	1	23	1	174	0.817	0.26	42.40	6.75	496.41	100.50	3.62	1.37	2.00	0.73	1.81
Hay-x1	2	23	1	207	0.927	0.23	42.26	5.22	458.20	66.21	5.34	1.54	2.73	0.90	1.95
Hay-x1	1	70	1	140	0.854	0.21	44.83	6.61	471.55	64.10	4.41	1.75	2.45	0.99	1.80
Hay-x1	1	250	1	130	0.917	0.38	41.21	9.70	488.72	145.00	5.10	2.56	3.07	1.59	1.66
Hay-x1	1	350	1	144	0.948	0.34	41.32	7.90	467.86	107.01	8.93	2.01	4.72	1.27	1.89
Hay-x3	1	23	1	87	0.802	0.26	31.21	8.61	574.07	102.05	17.70	4.00	10.03	3.91	1.77
Hay-x3	1	250	1	68	0.506	0.26	33.54	10.84	794.39	279.89	5.24	1.54	2.38	0.60	2.20
Hay-x3	2	250	1	130	0.583	0.24	36.41	9.35	708.83	199.97	3.03	1.19	1.83	0.73	1.66
Hay-x3	1	350	1	177	0.751	0.28	34.82	8.45	568.20	143.69	4.89	1.33	2.50	0.78	1.96

4.2 Post creep elasticity and strength

Creep nanoindentation grids were performed in parallel to bedding and normal to bedding directions at 23, 100, 200, and 300°C. Similar to short-duration indentation results, coupling analysis was performed to find the elemental intensities of Silicon, Aluminum, as well as Calcium and/or Potassium and then coupled with the mechanical properties. For creep analysis, indentation modulus, hardness, and contact creep modulus were used for mechanical properties. **Figs. 47 and 48** show that the trend of the indentation modulus and hardness between 23-200℃ are similar to short-duration indentation results. There is some variation in these properties; however, the overall trend is once again relatively stable and suggests that little to no change occurs between 23-200℃. However, it is important to note that the indentation hardness values obtained from creep experiments are slightly lower than those from short-duration indentation results. In the X1 and X3 directions, the average indentation hardness is 0.892 GPa and 0.661 GPa for short-duration indentation tests and 0.659 GPa and 0.576 GPa for creep indentation tests. This is likely due to a higher contact radius between the tip and sample right before unloading caused by the increased hold period during creep tests (200s). It is also important to note the small increase in indentation modulus between 23-200℃. In the X1 and X3 directions, the average indentation modulus is 42.4 GPa and 34.0 GPa for short-duration indentation tests and 39.8 GPa and 32.3 GPa for creep indentation tests. This is likely due to higher packing density values of the solid phase. **Tables 12** lists the various parameters measured and calculated for each of the time-independent experiments.

Table 12 – Haynesville shale results including Indentation Modulus, Indentation Hardness, Silicon, Aluminum, and Si/Al ratio for all creep indentation experiments.

Sample	Set	Temperature (°C)	Clay Phase	# of Indent	H (GPa)		M (GPa)		h (nm)		Creep, C (Gpa)		Tau, (s)		Si		Al		Si/Al
					Mean	Std. Dev.	Mean	Std. Dev.	Mean	Std. Dev.	Mean	Std. Dev.	Mean	Std. Dev.	Mean	Std. Dev.	Mean	Std. Dev.	
Hay-x1	1	23	1	160	0.72	0.23	40.69	6.39	520.72	88.00	194.96	75.28	0.63	0.74	6.35	1.68	2.93	0.70	2.17
Hay-x1	1	100	1	194	0.71	0.39	40.96	9.13	661.14	169.39	186.42	93.92	2.77	6.53	5.07	2.00	2.55	0.98	1.99
Hay-x1	1	200	1	69	0.54	0.08	37.86	4.60	680.31	50.18	134.81	34.79	1.05	1.92	4.78	2.68	1.97	0.58	2.42
Hay-x1	1	300	1	174	1.22	0.45	48.19	9.93	481.71	97.37	348.87	104.30	0.45	1.23	6.63	2.91	3.38	1.37	1.96
Hay-x3	1	23	1	124	0.37	0.17	25.38	7.27	794.84	349.72	131.72	69.18	0.61	0.70	6.37	2.85	3.04	1.27	2.09
Hay-x3	2	23	1,2	382	0.45	0.24	28.91	9.59	698.97	226.79	154.78	104.82	0.70	1.29	6.79	2.68	3.35	1.35	2.02
Hay-x3	1	100	1	90	0.65	0.26	35.26	9.48	660.65	144.50	172.13	73.83	0.44	1.43	7.18	2.37	4.18	1.63	1.72
Hay-x3	1	200	1	168	0.62	0.25	32.71	8.04	684.66	164.81	173.61	81.09	0.46	2.03	8.75	5.14	3.40	1.52	2.58
Hay-x3	1	300	1	202	1.22	0.66	41.36	11.96	518.92	169.52	331.97	224.42	0.95	4.99	7.28	3.73	3.50	1.82	2.08

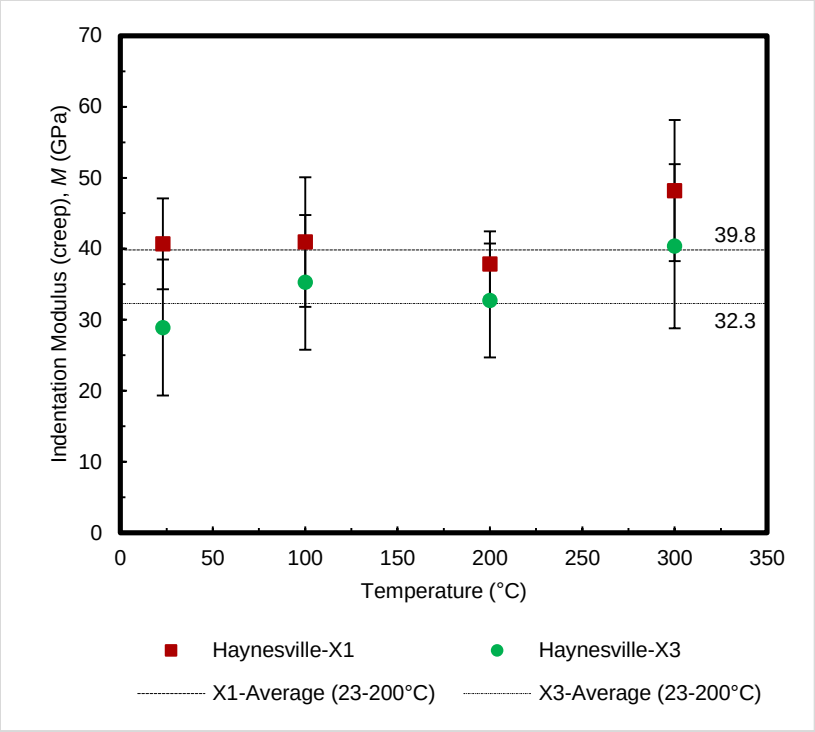

Figure 47 – Indentation modulus obtained from creep nanoindentation experiments for Haynesville shale samples parallel and perpendicular to bedding direction for a range of temperatures (23-300°C).

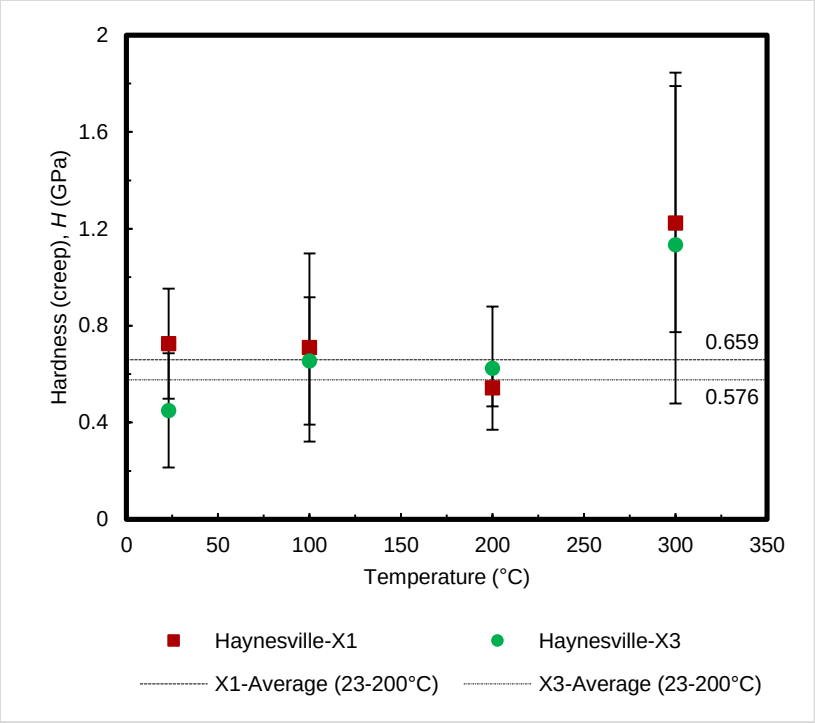

Figure 48 – Indentation hardness obtained from creep nanoindentation experiments for Haynesville shale samples parallel and perpendicular to bedding direction for a range of temperatures (23-300°C).

While similar time-independent trends are observed between creep experiments and short-duration indentation experiments, the results of hardness and modulus at 300°C from creep experiments are different and require further investigation. At 300°C, both the indentation hardness and modulus increased significantly compared to the results obtained by short-duration indentation (at 350°C) and the values at lower temperatures. There are two hypotheses to consider to explain this result. First, an increase in temperature yields an increase in the time-independent properties. Second, the conversion of TOC into hydrocarbons generates pores within the organic matter and as a result, provides room for particle sliding ad subsequent compaction during the creep phase. It is clear that the first

hypothesis is in contradiction based on the results obtained from short-duration indentation tests at 350°C, where negligible change in mechanical properties were observed. As a result, an increase in the mechanical properties of the constituents of the indented volume at 300°C is not significant enough to be the sole source of the observed increased response.

The second hypothesis required additional analysis of the indentation data to determine whether particle sliding occurs during creep experiments at 300°C. To further investigate this argument, a back-analysis approach that incorporates textural modeling is used. This analysis was proposed and validated by Abedi et al., (2016) and is described in **Appendix B**. The back-analysis approach is based on the self-consistent scheme assumption. First, the packing density of 0.202 is used and the mechanical properties of clay particles are obtained from short-duration experimental tests at 23°C. The obtained results are m_1=69.13 and h_1=1.96 GPa (X1) and m_3=52.2 GPa and h_3=1.96 GPa (X3). These results are consistent with the values obtained in Abedi et al. (2016) for a wide range of organic-rich shales with different thermal maturity levels and different organic contents. Assuming that there is negligible change in mechanical properties of the clay phase at high temperatures, a second back-analysis is performed using the results obtained from the first back-analysis to determine the packing density at each indentation point from creep indentation tests. The results produced are the predicted packing densities of the porous clay phase. The results from this analysis are plotted in **Fig. 49**.

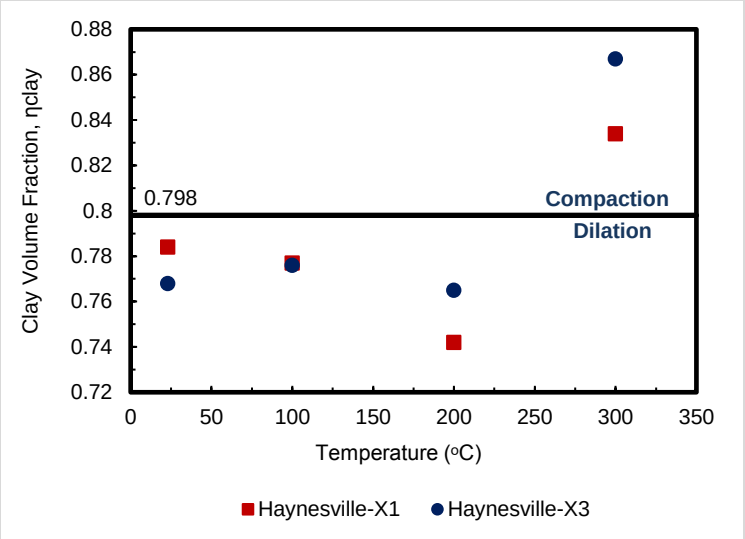

Figure 49 – Results from back-analysis showing changes in packing density during the holding phase.

Here, the packing density at room temperature is used as a reference point, above which the data points represent compaction and below which dilation occurs. It is clear that the packing density of clay between 23-200°C are in the dilation region as a consequence of a decrease in packing density. Dilation can be attributed to the formation of microcracks as also observed by Slim et al., (2017) in samples with low amounts of TOC. On the other hand, an increase in the clay packing density at 300°C proves that compaction of the clay particles occurs within the indented clay regions. As a result, the increased indentation modulus and hardness measured upon unloading at 300°C can be attributed to particle sliding and compaction caused by the conversion of TOC into hydrocarbons.

4.3 Creep rate from nanoindentation

The contact creep modulus values were obtained using a logarithmic function. The function was fitted to the raw experimental data and two parameters were obtained, one of which is the characteristic time and other, the contact creep modulus. **Fig. 50** shows the contact creep function as a function of time for three experimental curves. These curves represent the clay/kerogen phase. This trend is qualitatively similar to those obtained by Sone and Zoback (2014) at the macroscopic level. Creep test on shales can be performed within minutes through nanoindentation, thereby shedding light one of the major benefits of using nanoindentation to measure the long term creep kinetics of shales.

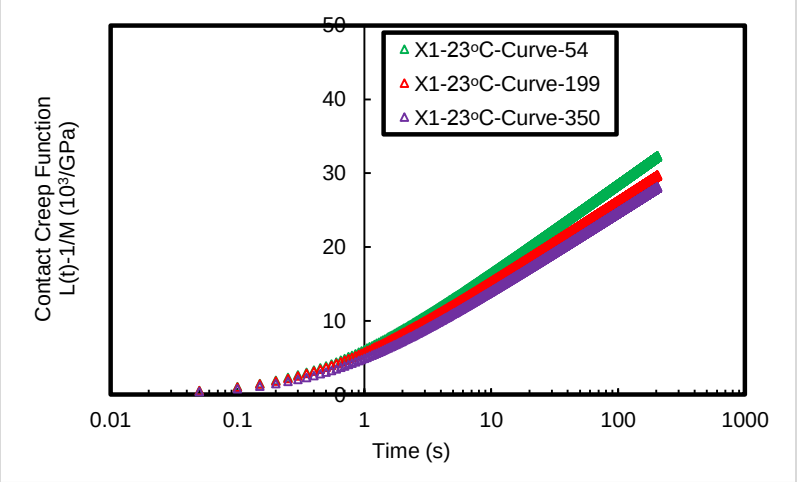

Figure 50 – Examples of three contact creep compliance functions obtained from creep nanoindentation experiments performed at 23°C on a Haynesville shale sample, parallel (X1) to bedding direction.

The contact creep modulus of the porous clay/kerogen phase were obtained for each experimental temperature value and are graphed in **Fig. 51**. The trend shows that the

contact creep modulus between 23-200°C is relatively stable and remains unchanged in both the X1 and X3 directions. However, the contact creep modulus at 300°C, the porous clay phase creeps slower (higher contact creep modulus) in both X1 and X3 directions. This shows that the organic phase plays a dominant role in driving the viscous behavior of organic-rich shales.

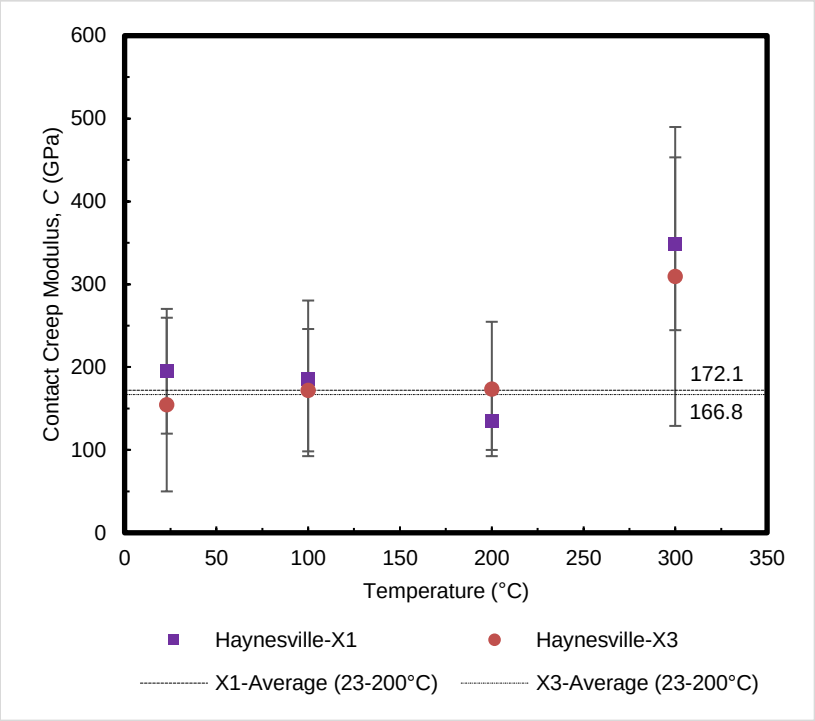

Figure 51 – Contact creep modulus data versus temperature (23-350°C) for all creep experiments performed on Haynesville shale samples parallel and perpendicular to bedding direction.

Additionally, the isotropic increase in both the X1 and X3 directions shed light on the role of the isotropic phases, which are organic matter and porosity, in driving the creep behavior in shales. These results are consistent with recently published results of Slim et

al. (2017), in which they performed indentations on mature and immature gas-rich shale samples and concluded that mature samples tend to creep less (higher contact creep modulus) than immature samples. This difference was attributed to kerogen and porosity and their tendency to drive creep rates within the composite clay phase. While the study by Slim et al. (2017) was limited to experiments at room temperature, this thought process can be applied to study the behavior of the porous organic-rich clay phases at elevated temperatures.

4.4 Thermogravimetry

The weight (%) change of the Haynesville sample as a function of temperature was measured by Thermogravimetry Analysis (TGA). The test was performed from room temperature (23°C) to 300°C at a heating rate of 5°C/min. The temperature was held constant for two hours at 300°C to investigate the weight change of the sample during high temperature creep indentations. **Fig. 52** shows the change in weight (%) and temperature (°C) as a function of time (min). These results show a substantial weight loss between 23°C and 100°C, where the beginning portion accounts for the loss of surface and pore water and the latter portion reflects the transformation of the fraction of organic matter that takes place between 200-450°C (Tissot and Welte, 1984). This transformation results in the formation of low to medium molecular weight hydrocarbons and pore spaces. **Fig. 53** shows a TGA experiment performed up to 350°C, in which the temperature was held constant at 70°C and 250°C for two hours. Here, the change in weight was approximately 0.66% and 0.30% and stabilized overtime; however, the weight loss

continues to increase above this temperature and shows no signs of stabilization. This once again shows that the first two stages are likely caused by the free and surface water in pore space, whereas the third stage corresponds to the transformation of organic matter into hydrocarbons.

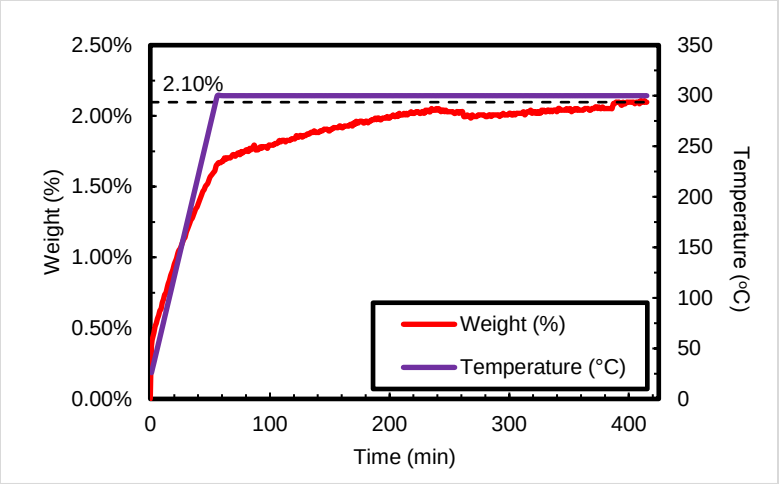

Figure 52 – Thermogravimetry Analysis (TGA) performed on Haynesville shale at 300°C; figure shows the change in weight (%) (primary axis) and temperature (°C) (secondary axis) versus time (min) (x-axis).

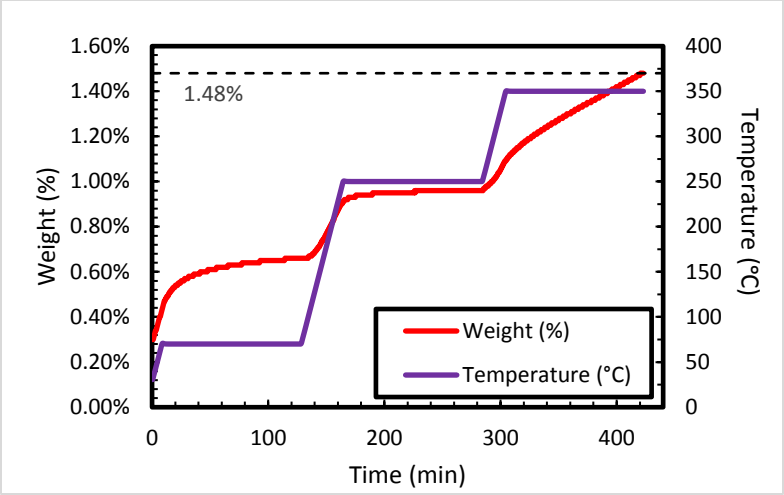

Figure 53 – Thermogravimetry Analysis (TGA) performed on Haynesville shale at 300°C; figure shows the change in weight (%) (primary axis) and temperature (°C) (secondary axis) versus time (min).

4.5 The role of organic matter and porosity: bimodal trend

To further evaluate the behavior of the porous clay/kerogen phase between 23-300°C, a histogram was plotted for each data set and fitted with a Probability Density Function. **Fig. 54** shows the experimental frequency distribution of the creep modulus for porous clay/kerogen present within the creep indentation grid (X3) at 23°C with an overlay of the deconvoluted peaks of each mode. The data was deconvoluted using the sample clustering technique, as presented in Section 3.4, for separating the various phases within the indented regions. From the distribution of the data set, the contact creep modulus can be divided into two categories and can be classified as the main driving mechanisms of creep in organic-rich shales. The first category represents the porous clay/kerogen phase whereas the second category represents the porous clay phase only. While these two mechanisms are present in the distributions between 23-200°C, the contact creep modulus

distribution at 300°C shows a unimodal distribution (**Fig. 55)**. The unimodal distribution coupled with a high contact creep modulus (creeps less) proves that the second mechanism, which is the porous clay phase, plays a dominant role in driving creep kinetics at this temperature.

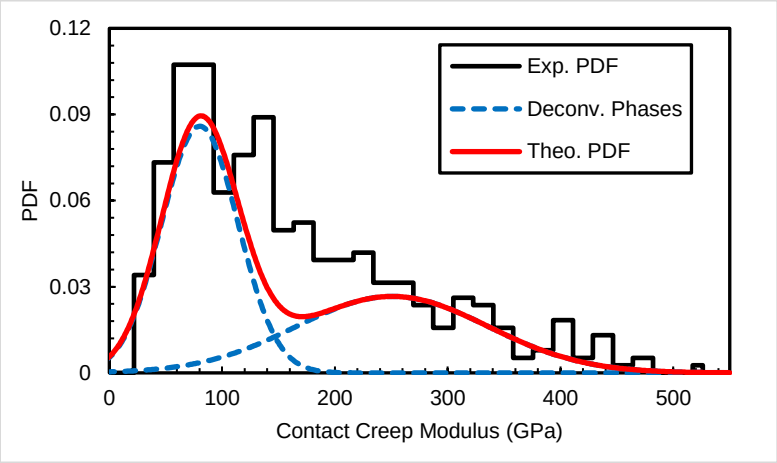

Figure 54 – Frequency density and Probability Density Function (PDF) of contact creep modulus values (x-axis) for porous clay/kerogen phase at X3-23°C overlaid with deconvoluted peaks.

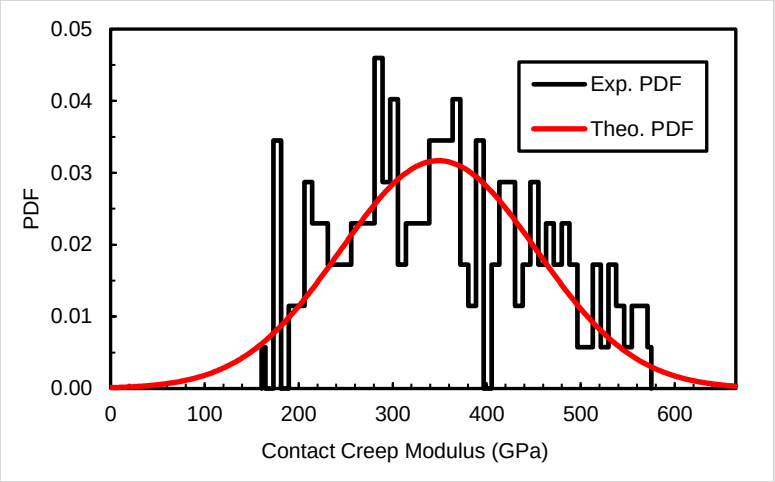

Figure 55 – Frequency density and Probability Density Function (PDF) of contact creep modulus values (x-axis) for the porous clay-kerogen phase at X1-300°C present within the Haynesville shale sample.

A summary of the probability density function distributions for each experimental temperature value are sketched in **Fig. 56** for comparison. Here, the first mechanism is termed mode I and the second mechanism is termed mode II. There are four main conclusions that can be drawn from the combines PDF distributions and volume fractions. First, the distributions for mode I align closely with each other and have an average of approximately 132 GPa. Similarly, the second mode (mode II) align closely and can be grouped with the unimodal distribution at 300°C. The average of mode II is 290 GPa. The exception to this argument is for X1-200°C, where a second mode was not detected.

Second, the distributions in the X1 and X3 for mode I and mode II are almost the same which means that the driving mechanisms are isotropic and show that the same behavior occurs in both parallel and perpendicular to bedding plane.

Third, using the deconvoluted results obtained and plotted in **Fig. 56**, the volume fractions of each experiment are compared in **Fig. 57**. The bar plots represent the fractional

contribution of mode I (porous clay/kerogen phase) and mode II (porous clay phase only), where the average volume fractions of mode I and mode II are 0.78 and 0.22, respectively. These values are similar to the contribution of organic matter and porosity, which can be obtained using the methodology provided in Section 3.2.3. The contribution of organic matter is $\frac{\eta_k}{\eta_k+\varphi} = \frac{0.1695}{0.1695+0.032} = 0.84$ and $\frac{\eta_k}{\eta_k+\varphi} = \frac{0.032}{0.1695+0.032} = 0.16$. This further supports the argument that mode I corresponds to the porous clay/kerogen phase and mode II corresponds to the porous clay phase.

Fourth, the unimodal distribution of contact creep modulus at 300°C exhibits peaks at 349 GPa (X1) and 309 GPa (X3) which are consistent with the second peak observed in the bimodal distributions of creep modulus between temperatures 23-200°C. This observation again points to the dominant role of organic matter in the creep behavior of organic-rich shales and supports the hypothesis that, at 300°C, the reduction in creep rate is attributed to the reduction of TOC due to exposure to high temperatures.

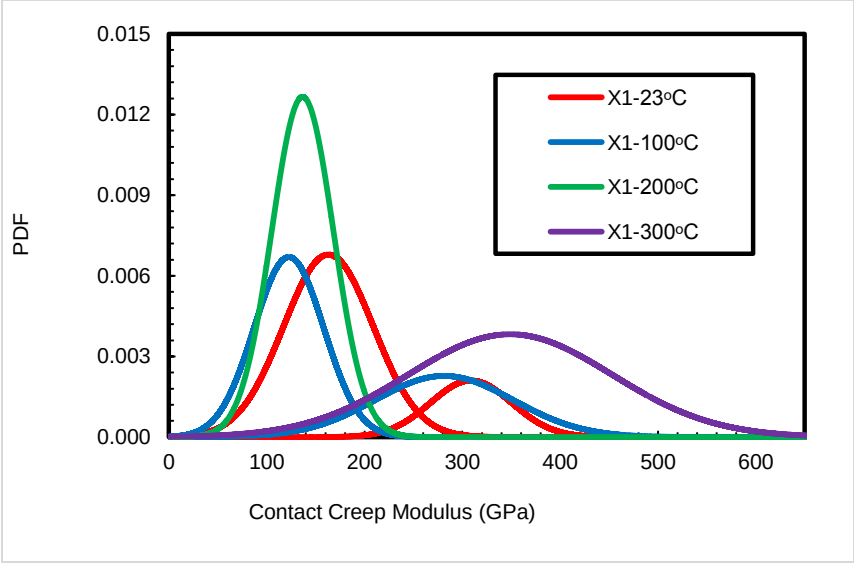

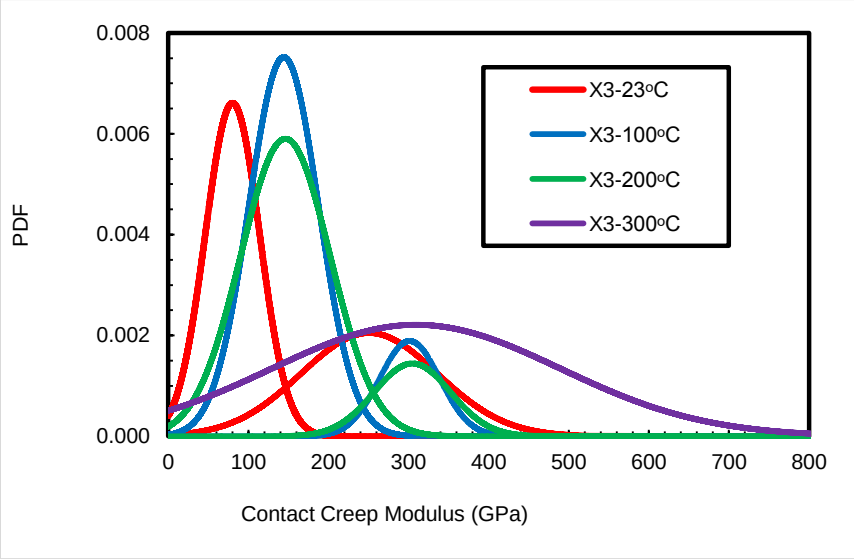

Figure 56 – Probability Density Functions (PDF) of the contact creep modulus values for porous clay/kerogen indentations performed parallel and perpendicular to bedding direction.

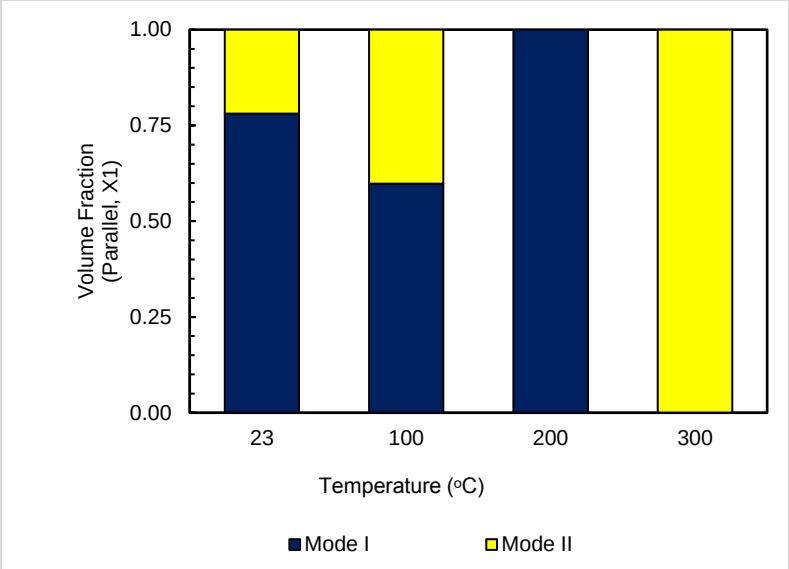

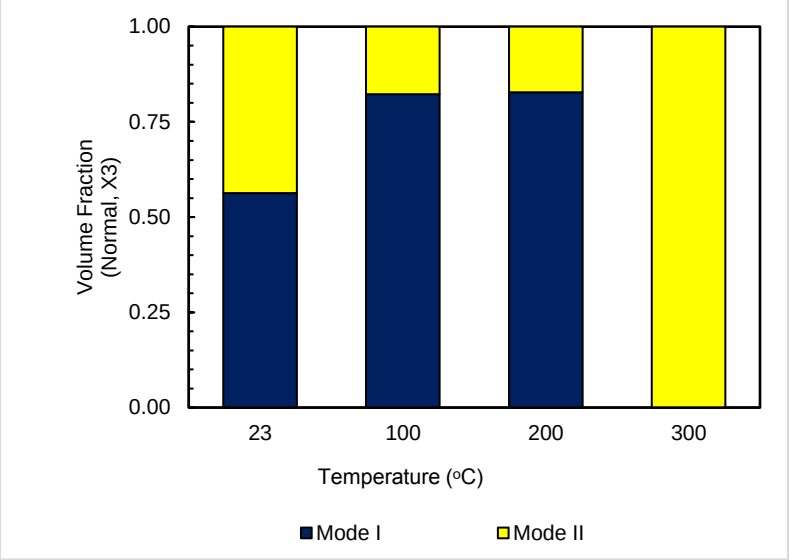

Figure 57 – Volume fractions detected within the porous clay/kerogen phases for all creep experiments in X1 and X3 directions.

The contribution of kerogen and porosity on creep properties is further analyzed by considering the porous kerogen-rich clay phase as a mixture of clay/kerogen and

clay/pore (porous clay) phases. The homogenized creep properties of these two phases, at the scale of nanoindentation, are obtained with a self-consistent homogenization scheme, as described previously (Vandamme and Ulm, 2013). Assuming a constant poisson's ratio $\nu = 0.2$, Vandamme and Ulm (2013) showed that the homogenized creep modulus of a composite material is linked to the creep modulus of its constituents through (**Eq. 4.1)**:

$$A\sum_{i=1}^{N}\eta_i\frac{1}{1+\frac{1}{2}\left((C_i/C^{hom})-1\right)}=\sum_{i=1}^{N}\eta_i\frac{C_i/C^{hom}}{1+\frac{1}{2}\left((C_i/C^{hom})-1\right)} \tag{4.1}$$

where η_i and C_i represent the volume fraction and contact creep modulus, respectively, of phase i and C^{hom} represents the homogenized contact creep modulus. It is assumed that the contact creep modulus of the clay/kerogen phase and the porous clay phase to be 132 GPa (average of mode I, X1 23-200℃ and X3 23-200℃) and 290 GPa (average of mode II, X1 23-200℃ and X3 23-200℃), respectively. Considering the contribution of organic matter is $\frac{\eta_k}{\eta_k+\varphi}=\frac{0.1695}{0.1695+0.032}=0.84$ and $\frac{\eta_k}{\eta_k+\varphi}=\frac{0.032}{0.1695+0.032}=0.16$, the homogenized creep modulus of the porous kerogen-rich clay is obtained to be 149 GPa; **Eq. 4.2** shows the input values required to solve for the homogenized contact creep modulus, denoted as "y".

$$0.84\cdot\frac{1}{1+0.5(\frac{132}{y}-1)}+0.16\cdot\frac{1}{1+0.5(\frac{290}{y}-1)} \tag{4.2}$$

$$=\ 0.84\cdot\frac{1}{1+0.5(\frac{132}{y}-1)}+0.16\cdot\frac{1}{1+0.5(\frac{290}{y}-1)}$$

The averaged contact creep modulus of all creep nanoindentation tests at temperatures 23–200°C is 169 GPa. The close agreement of the model-based estimate of contact creep modulus and experimental measurements supports the hypothesis that organic matter and porosity play a dictating role on creep properties. At 300°C, a portion of the organic matter is transformed into hydrocarbons and the effect of porous clay phase dominates the creep behavior.

4.6 Summary of results

1. Nanoindentation creep tests at elevated temperature on Haynesville shale show that an increase in the contact creep modulus (reduced creep rate) occurs in both parallel (X1) and perpendicular (X3) directions to bedding plane at 300°C. **Fig. 4.14** a comparison of the contact creep curve at 23°C and 300°C. This increase is attributed to the conversion of kerogen to hydrocarbons at 300°C which creates additional pore spaces (i.e. organoporosity) within the kerogen/clay. The isotropic increase in the contact creep modulus values at 300°C indicates toward the isotropic nature of organic matter and porosity and their dominant role in driving creep properties in shales.

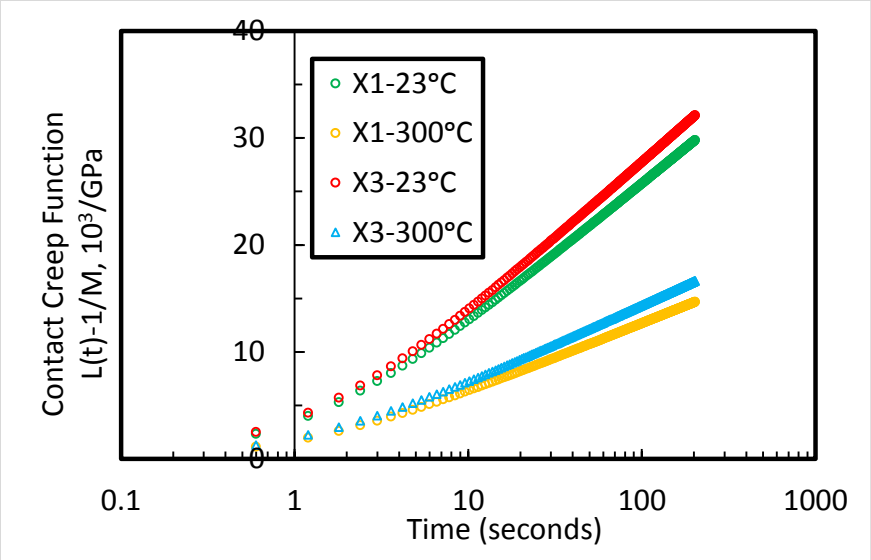

Figure 58 – Comparison of the creep curves at 23°C and 300°C.

2. In order to evaluate the results of creep obtained from nanoindentation tests, a logarithmic trend was used to fit the strain (ε) versus time (sec) data to obtain quantitative values for further evaluation. The fitted function provides two parameters for analysis: the contact creep modulus (C), which quantifies the long-term creep kinetics, and the characteristic time (τ), which represents the point at which creep kinetics starts to show a logarithmic trend. The contact creep modulus obtained through logarithmic fits was used as an input parameter in the clustering analysis in order to link it to the porous clay/kerogen phase.
3. The Probability density function (PDF) curves obtained for the contact creep modulus values of the porous clay/kerogen phases suggest that a bimodal distribution occurs between temperatures of 23-200°C, corresponding to two different modes: the clay/kerogen mode (mode I) and the porous clay mode (mode

II). However, at 300°C, the PDF function shows a unimodal trend, which aligns closely with mode II; this indicates that these values are only linked to the porous clay phase and not the clay/kerogen mode due to the conversion of kerogen to hydrocarbons.

4. The indentation modulus and hardness values of the porous clay/kerogen phase show little to no change with increasing temperatures; this homogenized response is an acceptable outcome considering the highly mature nature of the sample and aligns closely with the observations made by Emmanuel et al. (2016) on Kerogen's elastic properties with increasing temperatures. Through micromechanical modeling (back-analysis) results, dilation is observed in the clay particles between 23-200°C which is attributed to the formation of microcracks within the indented volume. At 300°C, there in an increase in the indentation hardness and modulus; this can be explained by the transformation of organic matter to hydrocarbons, which creates more room for particle sliding and compaction of the clay particles and causes higher stiffness and strength measurements.
5. The homogenized response, obtained assuming a self-consistent homogenization scheme, of the model-based approach aligns well with experimental results and suggests that organic matter and porosity play a dominant role in the creep behavior of organic-rich shales.

4.7 Chapter summary

In this chapter, all experimental and analytical results obtained in this project were provided. The effect of elasticity and strength with temperature is negligible. However, the elasticity and strength obtained through creep experiments shown an increase at 300°C in both the X1 and X3 directions. This is likely because of the particle sliding and compaction caused by the conversion of TOC into hydrocarbons. Next, the creep kinetics showed a similar trend which shed light on the possibility that organic matter and porosity expressing play a role in the isotropic response of creep. The response of organic matter and water at high temperatures is captured my TGA experiments. From additional analysis of these results, it is evident that there is a bimodal distribution in the contact creep modulus data (observed through PDFs) which affirms that organic matter and porosity are the main drivers of creep. The chapter ends with a summary of all of the findings.

CHAPTER V

CONCLUSION AND SIGNIFICANCE

This chapter summarized the major findings in this research, the limitations of this study, and ends with a significance of this work to petroleum engineers.

5.1 Conclusion

Short-duration and creep nanoindentation tests at ambient and elevated temperatures are performed to measure the elastic, strength, and creep properties of the porous clay/kerogen phase present within an organic-rich shale sample. Two hypotheses were studied to investigate the outcome of our experimental results. The first hypothesis was that the mechanical properties of organic matter or clay change with temperature. Negligible change occurs in the time-independent properties (elastic and strength) of the porous clay/kerogen phase between temperatures 23-350°C. The second hypothesis was that, at 300°C, the conversion of kerogen to hydrocarbons creates additional pore space allowing for particle sliding and compaction. This hypothesis is supported by results obtained from creep experiments. First, negligible anisotropy in creep rates is observed when comparing creep modulus in parallel to bedding (X1) and normal to bedding (X3) directions, which indicates toward the prevailing role of isotropic phases, specifically organic matter and porosity, in driving creep properties of organic-rich shales. Second, the results show a decrease in the creep rate (increased contact creep modulus) at 300°C in both parallel and perpendicular to bedding plane, proving the dominant role of organic matter in driving the viscous behavior of organic-rich shales. Micromechanical modeling

of the post creep mechanical response predicts the compaction of clay particles at the end of creep deformation at 300°C, signaling the existence of more pore space for particle sliding and compaction due to of kerogen transformation.

A closer examination of the creep results at temperatures 23-200°C shows a bimodal trend within the porous clay/kerogen phase. It is suggested that the first mode captures the contribution of kerogen whereas the second mode is linked to the effect of porosity on viscoelastic response. On the other hand, the creep modulus of the porous clay/kerogen phase at 300°C exhibits a unimodal distribution with a wider range and combines both the kerogen and porosity modes due to the lesser contribution of kerogen.

While these experiments shed light on the role of organic matter and porosity in organic-rich shales, this study focuses on a single shale formation. Further studies are required on both mature and immature shale samples to capture the time-dependent relationship present between organic matter (kerogen/bitumen), clays, and porosity from different depositional environments.

5.2 Significance

The significance of this work is to help petroleum engineers better understand the impact of high temperatures on the time-dependent (creep) properties of shales as well as the main factors that influence this time-dependent response. Many source rocks have a relatively low permeability which makes hydrocarbon extraction an expensive process. While hydraulic fracturing can help increase the amount of hydrocarbons recovered from the formation, several factors including the loss of fracture conductivity can result in lower

recovery and inefficient production. The loss of the fracture conductivity can be associated with the creep of the rock. The behavior of creep can be studied in laboratories at both the microscale and macroscale. Unlike macroscopic triaxial tests which can take a significant amount of time to produce meaning creep results, microscopic tests require shorter experimental times and small amounts of samples to produce meaningful results. Furthermore, studying the creep properties of rocks at elevated temperatures could shed light on the behavior of the rock in the reservoir and for thermal recover efforts performed in the reservoir. Producing quantitative values from short-term nanoindentation tests can quickly help petroleum engineers assess the quality of the reservoir early on, provide insight on how to accurately assess hydrocarbon recovery, and lead to optimized hydraulic fracture operations for economic production. The experimental procedure and analytical method presented here could also be used by researchers to investigate other shale formations with varying levels of maturity and develop a better understanding between kerogen/bitumen, clays, and porosity from different depositional environments.

REFERENCES

Aad, Georges, et al. "Electron and photon energy calibration with the ATLAS detector using LHC Run 1 data." *The European Physical Journal* C 74.10 (2014): 3071.

Abedi, Sara, et al. "Nanochemo-mechanical signature of organic-rich shales: a coupled indentation–EDX analysis." *Acta Geotechnica* 11.3 (2016): 559-572.

Abedi, Sara, Mirna Slim and Franz-Joseph Ulm. "Nanomechanics of organic-rich shales: the role of thermal maturity and organic matter content on texture." *Acta Geotechnica* 11.4 (2016): 775-787.

Abousleiman, Younane N., et al. "Geomechanics field and laboratory characterization of the Woodford Shale: The next gas play." *SPE Annual Technical Conference and Exhibition*. Society of Petroleum Engineers, 2007.

Ahmadov, Ramil Surhay oglu. "Microtextural, elastic and transport properties of source rocks." Doctor of Philisophy Dissertation. Standford University, 2011.

Ajayi, Babatunde Tolulope, et al. "Channel hydraulic fracturing and its applicability in the marcellus shale." *SPE Eastern Regional Meeting.* Society of Petroleum Engineers, 2011.

Baojun, Bai, et al. "Rock characterization of Fayetteville shale gas plays." *Fuel Journal* 105 (2013): 645-652.

Bassiouni, Zaki. *Theory, measurement, and interpretation of well logs*. Vol. 4. Society of Petroleum Engineers, 1994.

Bear, Firman E. "Chemistry of the Soil." *Soil Science Journal* 98.1 (1964): 70.

Blatt, Harvey, Robert Tracy and Brent Owens. *Petrology Igneous, Sedimentary, and Magmatic.* 3rd. W.H. Freeman, 2006.

Bobko, Christopher and Franz-Josef Ulm. "The nano-mechanical morphology of shale." *Mechanics of Materials* 40.4 (2008): 318-337.

Bulychev, S. I., et al. "Determination of Young modulus by the hardness indentation diagram." *Zavodskaya Laboratoriya* 41.9 (1975): 1137-1140.

Chateau, Xavier and Luc Dormieux. "Micromechanics of saturated and unsaturated porous media." *International Journal for Numerical and Analytical Methods in Geomechanics* 26.8 (2002): 831-844.

Dake, L. P. *Fundamentals of reservoir engineering: Developments in Petroleum Science.* Vol. 8. Amsterdam: Elsevier, 1978.

Deirieh, A., et al. "Nanochemomechanical assessment of shale: a coupled WDS-indentation analysis." *Acta Geotechnica* 7.4 (2012): 271-295.

Delafargue, Antoine and Franz-Josef Ulm. "Explicit approximations of the indentation modulus of elastically orthotropic solids for conical indenters." *International Journal of Solids and Structures* 41.26 (2004): 7351-7360.

Deville, Jay P., Brady Fritz and Michael Jarrett. "Development of water-based drilling fluids customized for shale reservoirs." *SPE Drilling & Completion* 26.04 (2011): 484-491.

Doerner, Mary F. and William D. Nix. "A method for interpreting the data from depth-sensing indentation instruments." *Journal of Materials Research* 1.04 (1986): 601-609.

Donnelly, Eve, et al. "Effects of surface roughness and maximum load on the mechanical properties of cancellous bone measured by nanoindentation." *Journal of Biomedical Materials Research Part A* 77.2 (2006): 426-435.

Dormieux, L., A. Molinari and D. Kondo. "Micromechanical approach to the behavior of poroelastic materials." *Journal of the Mechanics and Physics of Solids* 50.10 (n.d.): 2203-2231.

Dormieux, Luc, Djimédo Kondo and and Franz-Josef Ulm. *Microporomechanics*. John Wiley & Sons, 2006.

Easley, G., Richard Sigal and Chandra Rai. "Thermogravimetric analysis of Barnett shale samples." *Society of Core Analysts Annual Symposium*. Calgary, 2007.

Eliyahu, Moshe, et al. "Mechanical properties of organic matter in shales mapped at the nanometer scale." *Marine and Petroleum Geology* 59 (2015): 294-304.

Emmanuel, Simon, et al. "Softening of organic matter in shales at reservoir temperatures." *Petroleum Geoscience* (2016): 2016-2035.

Energy Information Administration. "Where Our Natural Gas Comes From." n.d. 19 February 2017.

Findley, William N., James S. Lai and Kasif Onran. *Creep and relaxation of non-linear materials with an introduction to linear viscoelasticity.* New York: North-Holland Publishing Company, 1976.

Fraley, Chris and Adrian E. Raftery. "Model-based methods of classification: using the mclust software in chemometrics." *Journal of Statistical Software* 18.6 (2007): 1-13.

Fritz, Brady and Michael Jarrett. "Potassium silicate treated water-based fluid: an effective barrier to instability in the fayetteville shale." *IADC/SPE Drilling Conference and Exhibition* (2012).

Gathier, B. "Multiscale strength homogenization: application to shale nanoindentation." Massachusetts Institute of Technology, 2008.

Gips, Jameson Parker. "Shale Characterization Using TGA, Py-GC-MS, and NMR." Master of Science Thesis. The University of Texas at Austin, 2014.

Grebowicz, Janusz. "Understanding thermal properties of oil shales at high temperature toward application of nuclear energy in extraction of natural hydrocarbons." *Journal of Thermal Analysis and Calorimetry* 116.3 (2014): 1481-1490.

Gualtieri, Dan. "Meeting the Challenges of the Marcellus ShaleThrough Technology." Halliburton presentation, 2009.

Guo, Quan, et al. "Marcellus and Haynesville drilling data: Analysis and lessons learned." *SPE Asia Pacific Oil and Gas Conference and Exhibition*. Society of Petroleum Engineers, 2012.

Hayatdavoudi, A. and A. Ghalambor. "Controlling formation damage caused by kaolinite clay minerals: Part I." *SPE Formation Damage Control Symposium*. Society of Petroleum Engineers, 1996.

Hellmich, C., J. F. Barthélémy and L. Dormieux. "Mineral–collagen interactions in elasticity of bone ultrastructure–a continuum micromechanics approach." *European Journal of Mechanics-A/Solids* 23.5 (2004): 783-810.

Holditch, Stephen A. "The increasing role of unconventional reservoirs in the future of the oil and gas business." *Journal of Petroleum Technology* 55.11 (2003): 34-79.

Hysitron. "Hysitron Temperature Control Stages." 2014.

Ibanez, William D., and Andreas K. Kronenberg. "Experimental deformation of shale: Mechanical properties and microstructural indicators of mechanisms." *International Journal of Rock Mechanics and Mining Sciences & Geomechanics Abstracts* 30.7 (1993).

Izadi, Ghazal, et al. "Production Performance in Marcellus Shale: Multidisciplinary Study of Hydraulic Fracturing." *Abu Dhabi International Petroleum Exhibition and Conference*. Society of Petroleum Engineers, 2014.

Jones, Christopher A., and Zachary C. Grasley. "Short-term creep of cement paste during nanoindentation." *Cement and Concrete Composites* 33.1 (2011): 12-18.

Kargbo, David M., Ron G. Wilhelm and David J. Campbell. "Natural gas plays in the Marcellus Shale: Challenges and potential opportunities." *Environmental Science & Technology* 44.15 (2010): 5679-5684.

Keller, W. D., R. C. Reynolds and Atsuyuki Inoue. "Morphology of clay minerals in the smectite-to-illite conversion series by scanning electron microscopy." *Clays Clay Miner* 34.2 (1986): 187.

Kuila, Utpalendu, and Manika Prasad. "Specific surface area and pore-size distribution in clays and shales." *Geophysical Prospecting* 61.2 (2013): 341-362.

Kumar, Vikas, Carl H. Sondergeld, and Chandra Shekhar Rai. "Nano to macro mechanical characterization of shale." *SPE Annual Technical Conference and Exhibition*. Society of Petroleum Engineers, 2012.

Lee, E. H. and J. R. M. Radok. "The Contact Problem for Visooelastia Bodies." *Journal of Applied Mechanics* 27.3 (1960): 438-444.

Li, Yawei and Ahmad Ghassemi. "Creep behavior of Barnett, Haynesville, and Marcellus shale." *46th US Rock Mechanics/Geomechanics Symposium*. American Rock Mechanics Association, 2012.

Loucks, Robert G., et al. "Spectrum of pore types and networks in mudrocks and a descriptive classification for matrix-related mudrock pores." *American Association of Petroleum Geologists* 96.6 (2012): 1071-1098.

Lu, Y. C., et al. "High temperature nanoindentation of PMR-15 polyimide." *Experimental Mechanics* 50.4 (2010): 491-499.

Macht, Felix, et al. "Specific surface area of clay minerals: comparison between atomic force microscopy measurements and bulk-gas (N2) and-liquid (EGME) adsorption methods." *Applied Clay Science* 53.1 (2011): 20-26.

Mitchell, James Kenneth and Kenichi Soga. *Fundamentals of Soil Behavior*. 3rd. John Wiley & Sons, 2005.

N., Jared, O. Cuisinier and F. Masrouri. "Temperature impact on the creep behavior of compacted illitic clay." *Energy Geotechnics* (2016): 691-697.

Oliver, Warren Carl and George Mathews Pharr. "An improved technique for determining hardness and elastic modulus using load and displacement sensing

indentation experiments." *Journal of Materials Research* 7.02 (1992): 1564-1583.

Ortega, J. Alberto. "Microporomechanical modeling of shale." Doctor of philosophy Dissertation. Massachusetts Institute of Technology, 2009.

Parker, Mark A., et al. "Haynesville shale-petrophysical evaluation." *SPE Rocky Mountain Petroleum Technology Conference*. Society of Petroleum Engineers, 2009.

Pope, Charles, et al. "Haynesville Shale-One Operator's Approach to Well Completions in this Evolving Play." *SPE Annual Technical Conference and Exhibition*. Society of Petroleum Engineers, 2009.

Rassouli, F. S., and M. D. Zoback. "A comparison of short-term and long-term creep experiments in unconventional reservoir formations." *50th US Rock Mechanics/Geomechanics Symposium*. American Rock Mechanics Association, 2016.

Rengasamy, P., Krishna Murti and V. A. K. Sarma. "Isomorphous substitution of iron for aluminum in some soil kaolinites." *Clays and Clay Minerals* 23.3 (1975): 211-214.

Shukla, Priyavrat, et al. "Nanoindentation studies on shales." *47th US Rock Mechanics/Geomechanics Symposium*. American Rock Mechanics Association, 2013.

Slim, M., S. Abedi and F. J. Ulm. "Creep Properties of Source Rocks Using Indentation: The Role of Organic Matter." *Acta Geotechnica* (2017). Approved for publishing.

Smith, Joseph. "Using Nuclear Heat for In-Situ Recovery of Unconventional Hydrocarbons: A Case for the High Temperature Gas Reactor (HTGR)." 2010. Idaho National Laboratory.

Sone, Hiroki and Mark D. Zoback. "Mechanical properties of shale-gas reservoir rocks—Part 1: Static and dynamic elastic properties and anisotropy." *Geophysics* 78.5 (2013): D381-D392.

Sone, Hiroki and Mark D. Zoback. "Time-dependent deformation of shale gas reservoir rocks and its long-term effect on the in situ state of stress." *International Journal of Rock Mechanics and Mining Sciences* 69 (2014): 120-132.

Sone, Hiroki, and Mark D. Zoback. "Mechanical properties of shale-gas reservoir rocks—Part 2: Ductile creep, brittle strength, and their relation to the elastic modulus." *Geophysics* 78.5 (2013): D393-D402.

Song, Bo, and Christine A. Ehlig-Economides. "Rate-normalized pressure analysis for determination of shale gas well performance." *North American Unconventional Gas Conference and Exhibition*. Society of Petroleum Engineers, 2011.

Terracina, John M., et al. "Proppant selection and its effect on the results of fracturing treatments performed in shale formations." *SPE Annual Technical Conference and Exhibition*. Society of Petroleum Engineers, 2010.

Thompson, John, et al. "An overview of horizontal-well completions in the Haynesville Shale." *Journal of Canadian Petroleum Technology* 50.06 (2011): 22-35.

Tissot, B. P. *Petroleum Formation and Occurrence*. Springer-Verlag Berlin Heidelberg, 1984.

Trichel, Donald Keith and John A. Fabian. "Understanding and Managing Bottom Hole Circulating Temperature Behavior in Horizontal HT Wells-A Case Study Based on Haynesville Horizontal Wells." *SPE/IADC Drilling Conference and Exhibition*. Society of Petroleum Engineers, 2011.

Ulm, Franz-Josef, and Younane Abousleiman. "The nanogranular nature of shale." *Acta Geotechnica* 1.2 (2006): 77-88.

Vandamme, Matthieu and F-J. Ulm. "Nanoindentation investigation of creep properties of calcium silicate hydrates." *Cement and Concrete Research* 52 (2013): 38-52.

Wang, C. L., M. Zhang, and T. G. Nieh. "Nanoindentation creep of nanocrystalline nickel at elevated temperatures." *Journal of Physics D: Applied Physics* 42.11 (2009): 115405.

Wenk, Hans-Rudolf, et al. "Preferred orientation and elastic anisotropy of illite-rich shale." *Geophysics* 72.2 (2007): E69-E75.

Williams, Robert Heath, et al. "Flexible, expanding cement system (FECS) successfully provides zonal isolation across Marcellus shale gas trends." *Canadian Unconventional Resources Conference*. Society of Petroleum Engineers, 2011.

Zaoui, A. "Continuum micromechanics: survey." *Journal of Engineering Mechanics* 128.8 (2002): 808-816.

Zargari, Saeed, et al. "Organic maturity, elastic properties, and textural characteristics of self resourcing reservoirs." *Geophysics* 78.4 (2013): D223-D235.

Zhang, Qing, et al. "Long-term creep properties of cementitious materials: Comparing microindentation testing with macroscopic uniaxial compressive testing." *Cement and Concrete Research* 58 (2014): 89-98.

APPENDIX A

$$M = \frac{E}{1-\nu^2} = 4G\frac{3K+G}{3K+4G}$$

Starting with,

$$E = \frac{9KG}{3K+G}$$

and,

$$\nu = \frac{3K-2G}{2(3K+G)} = \frac{3K-2G}{6K+2G}$$

Substitute into the original equation:

$$M = \frac{\frac{9KG}{3K+G}}{1-\left(\frac{3K-2G}{2(3K+G)}\right)^2}$$

Assume K = a and G = b,

$$M = \frac{9ab}{\left(1-\left[\left(\frac{3a-2b}{2(3a+b)}\right)\right]^2\right)*(3a+b)}$$

$$M = \frac{9ab}{\left(1-\frac{(3a-2b)^2}{4*(3a+b)^2}\right)*(3a+b)}$$

$$M = \frac{9ab}{\left(\frac{4*(3a-2b)^2}{4*(3a+b)^2}-\frac{(3a-2b)^2}{4*(3a+b)^2}\right)*(3a+b)}$$

$$M = \frac{9ab}{\left(\frac{4*(3a+2b)^2-(3a+2b)^2}{4*(3a+b)^2}\right)*(3a+b)}$$

$$M = \frac{9ab}{\left(\frac{3a+b)*(4*(3a+2b)^2-(3a+2b)^2)}{4*(3a+b)^2}\right)}$$

$$M = \frac{9ab * (4 * (3a + b)^2)}{(3a + b) * (4 * (3a + b)^2 - (3a + 2b)^2)}$$

$$M = \frac{9ab * (4(3a + b))}{(4(3a + b)^2 - (3a + 2b)^2)}$$

Expand using the FOIL method:

$$(3a + b)^2 = 9a^2 + 6ab + b^2$$

and

$$(3a - 2b)^2 = 9a^2 - 12ab + 4b^2$$

$$M = \frac{9ab * 4 * (3a + b)}{4(9a^2 + 6ab + b^2) - (9a^2 - 12ab + 4b^2)}$$

$$M = \frac{9ab * 4 * (3a + b)}{36a^2 + 24ab + b^2 - 9a^2 + 12ab - 4b^2}$$

Grouping like terms,

$$M = \frac{9ab * (4(3a + b))}{27a^2 + 36ab}$$

$$M = \frac{9b * (4(3a + b))}{9(3a + 4b)}$$

$$M = \frac{4b * (3a + b)}{(3a + 4b)}$$

Substitute back a = K and b = G,

$$M = \frac{4G * (3K + G)}{(3K + 4G)}$$

A derivation on how to obtain the following derivation is shown next:

$$E = \frac{9KG}{3K + G}$$

We know that,

$$E_{ii} = \frac{1}{E_y}[(1+v)T_{ii} - 3vT_{kk}] = \frac{1}{E_y}[(1-2v)T_{ii}]$$

where $T_{ii} = 3\sigma$. Rearranging the above equation, we get:

$$K = \frac{\sigma}{e} = \frac{E_y}{3(1-2v)}$$

which can we re-written as,

$$K = \frac{E}{3(1-2v)}$$

Combining $v = \frac{E}{2G} - 1$ and $K = \frac{E}{3(1-2v)}$, we get:

$$K = \frac{E}{3(1-2\left(\frac{E}{2G}-1\right))}$$

Rearranging and solving for E, we get:

$$E = \frac{9KG}{G+3K}$$

A derivation on how to obtain the following equation is provided next:

$$v = \frac{3K-2G}{2(3K+G)} = \frac{3K-2G}{6K+2G}$$

We know that,

$$K = \frac{\sigma}{e} = \frac{E_y}{3(1-2v)}$$

Rewriting this equation, we get:

$$K = \frac{\sigma}{e} = \frac{E_y}{3(1-2v)}$$

$$e = \frac{\sigma}{K} = \frac{3\sigma(1-2v)}{E_y}$$

The stresses cancel and we are left with the simplified equation:

$$E_y = 3K(1 - 2v)$$

We know that,

$$G = \frac{E_y}{2(1 + v)}$$

Substituting this equation into the simplified equation, we get:

$$v = \frac{2G + 3K}{6K + 2G}$$

APPENDIX B

For an indentation test performed on porous organic-rich clay phase, the indentation volume probed by a Berkovich indenter is composed of the clay particles, the organic phase, and the empty pore spaces. Therefore, the mechanical response of the indentation test, i.e., indentation modulus (*M*) and indentation hardness (*H*), are representative of the homogenized response of porous organic-clay particles. This homogenized response can be written in dimensionless form as (Abedi et al., 2016):

$$\frac{M}{m_s} = \Pi_M \left(\frac{C_{ijkl}}{m_s}, \eta_s, \eta_k, \eta_0 \right) \tag{B-1}$$

$$\frac{H}{h_s} = \Pi_H (\eta_s, \eta_k, \eta_0) \tag{B-2}$$

with m_s and h_s being modulus and hardness of clay particles, η_k volume fraction of kerogen, η_s volume fraction of clay particles, and η_0 percolation threshold which characterizes microstructural texture of the indented volume. The model can be used to back calculate mechanical properties of clay particles and porosity or volume fraction of kerogen from indentation mechanical properties (*M* and *H*). In their back-analysis approach, Abedi et al., (2016) successfully attributed the role of thermal maturity on texture in modeling elasticity and strength of organic-rich shales, with immature systems exhibiting a matrix-inclusion morphology, while mature systems exhibit a polycrystal morphology (self-consistent scheme). Considering results of rock-eval pyrolysis, Haynesville sample can be considered as a mature sample; thus, we use a self-consistent morphology in back-analyzing indentation data.

The homogenized stiffness tensor of the anisotropic porous organic-rich clay phase can be obtained using linear micromechanics theory (Chateau and Dormieux, 2002; Dormieux et al., 2002; Dormieux et al., 2006; Hellmich et al., 2004; Ortega, et al., 2009):

$$\mathbb{C}^{hom} = \sum_r \eta^r \mathbb{C}^r \mathbb{A}^r \tag{B-3}$$

Based on the above equation, the homogenized stiffness tensor $\mathbb{C}^{hom}$ depends on the stiffness $\mathbb{C}^r$, packing density η^r, and the strain concentration tensor $\mathbb{A}^r$ of each phase r in a multiphase material. The strain concentration tensor is given by (Dormieux et al., 2002; Hellmich et al., 2004; Ortega, et al., 2009; Zaoui, 2002):

$$\mathbb{A}^r = [\mathbb{I} + \mathbb{P}^r : (\mathbb{C}^r - \mathbb{C}^0)]^{-1} : \left\{\sum_s \eta_s [\mathbb{I} + \mathbb{P}^s : (\mathbb{C}^s - \mathbb{C}^0)]^{-1}\right\}^{-1} \tag{B-4}$$

where $\mathbb{I}$ is the fourth-order unit tensor and $\mathbb{P}^s$ is the Hill tensor that describes particle interactions and particles shapes. For the self-consistent estimate (considered in this study for mature Haynesville samples) $\mathbb{C}^0 = \mathbb{C}^{hom}$, with $\mathbb{C}^{hom}$ being the homogenized stiffness of the composite material.

Nonlinear micromechanics (Dormieux et al., 2002; Fritsch et al., 2007; Gathier, 2008) is used to obtain the dimensionless equation presented in equation B-2. For the case of granular morphology, this dimensionless function is obtained as (Bobko and Ulm):

$$\Pi_H = \frac{\sqrt{2\left(1 - 2(\varphi + \eta_k)\right)} - \left(1 - 2(\varphi + \eta_k)\right)}{\sqrt{2} - 1} \times (1 + b(\varphi + \eta_k) + c(\varphi + \eta_k)^2 + d(\varphi + \eta_k)^3) \tag{B-5}$$

and for a cohesive solid that obeys Von-Mises strength criterion, the solid's hardness, h_s, is related to the solid's cohesion, c_s, by $h_s = ac_s$ where $\mathrm{a} = 4.7644, \mathrm{b} = -5.3678, \mathrm{c} = 12.1933, \mathrm{d} = -10.3071, \mathrm{e} = -1.2078, \mathrm{f} = 0.4907$, and $\mathrm{g} = -1.7257$.

In applying the back-analysis approach to our indentation data, we have considered negligible kerogen's strength and stiffness compared to clay particles properties.

APPENDIX C

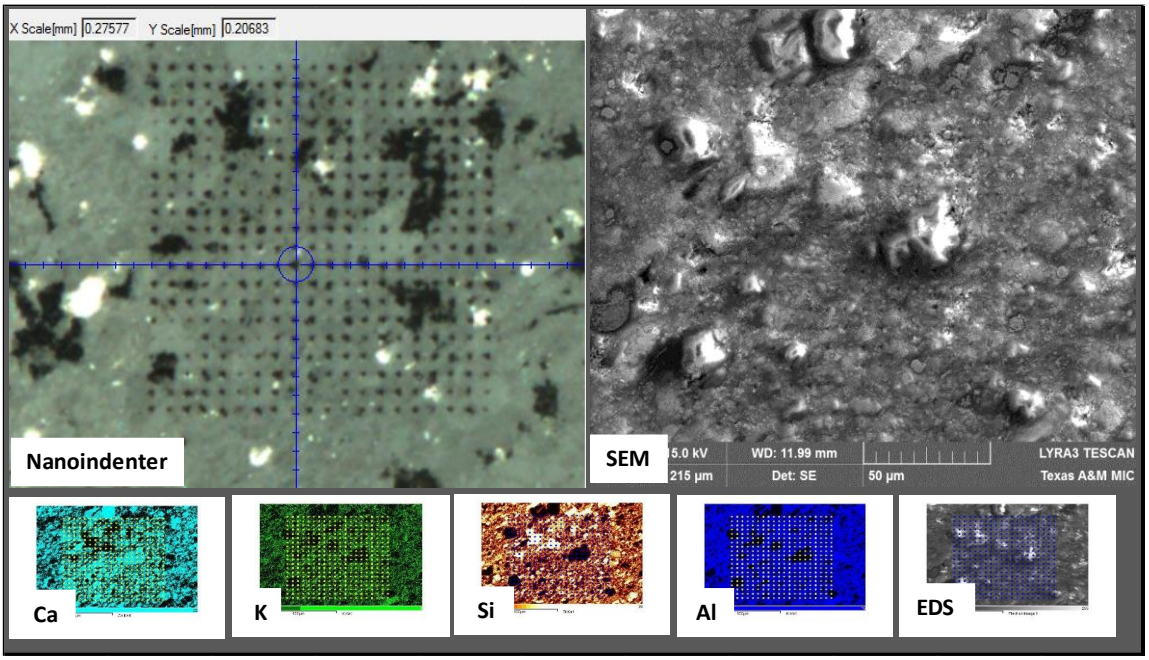

Figure C.1 – Nanoindentation grid and corresponding SEM, Calcium, Potassium, Silicon, Aluminum, and EDX maps for X1-23°C.

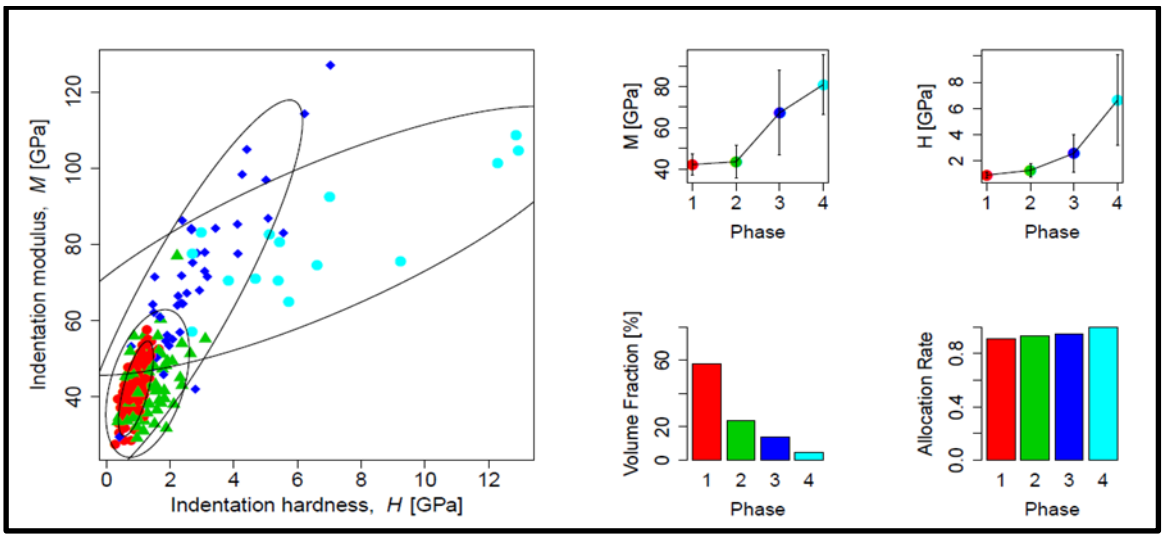

Figure C.2 – Clustering results for X1-23°C; indentation modulus vs. indentation hardness and modulus, hardness, volume fraction, and allocation rate for each phase detected.

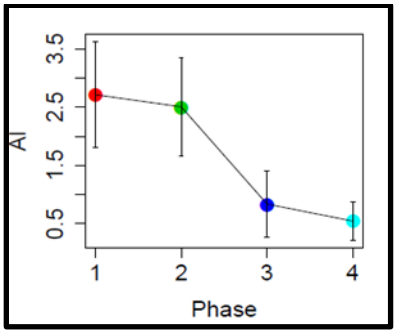

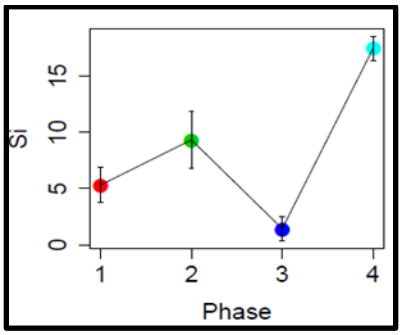

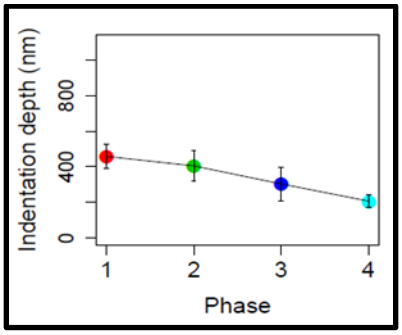

Figure C.3 – Clustering results for aluminum, silicon, and indentation depth at X1-23°C for each phase detected.

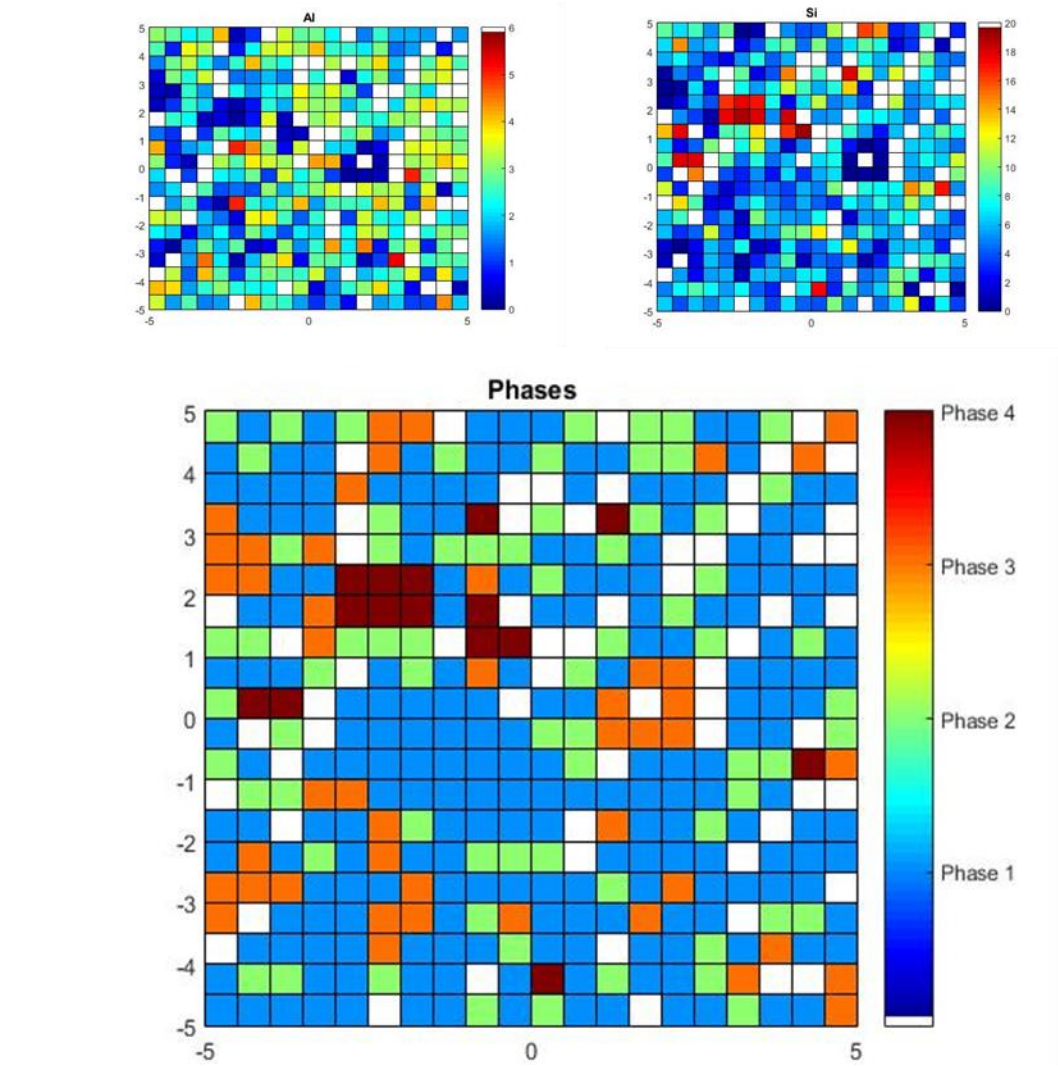

Figure C.4 – Color maps for aluminum, silicon, and indentation depth at X1-23°C for each phase detected.

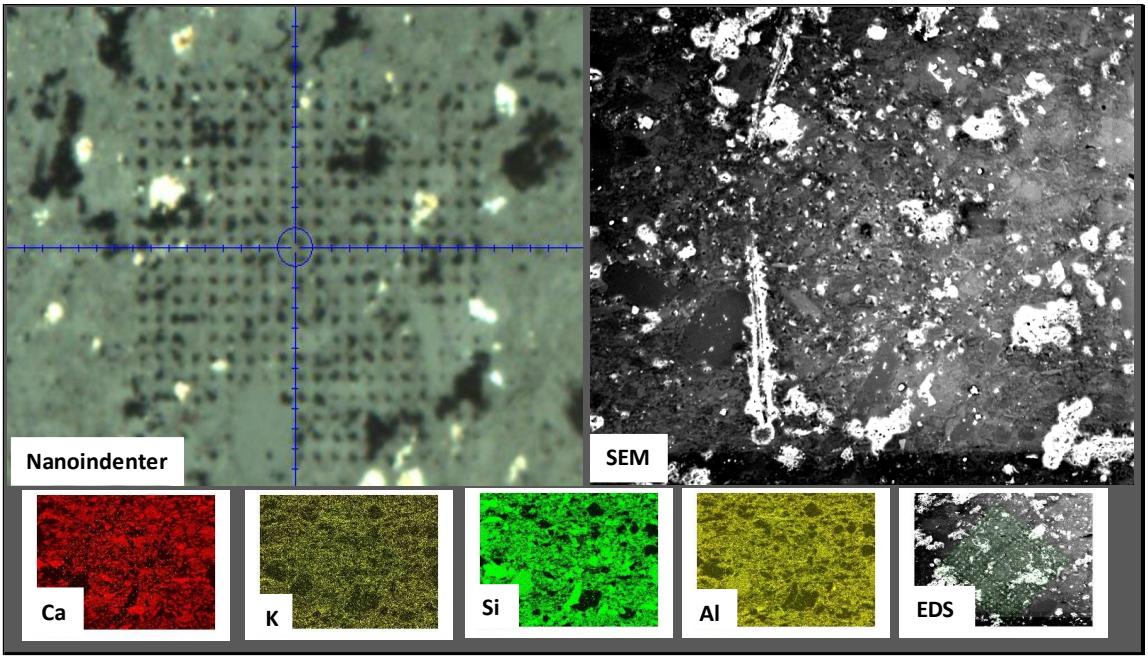

Figure C.5 – Nanoindentation grid and corresponding SEM, Calcium, Potassium, Silicon, Aluminum, and EDX maps for X1-70°C.

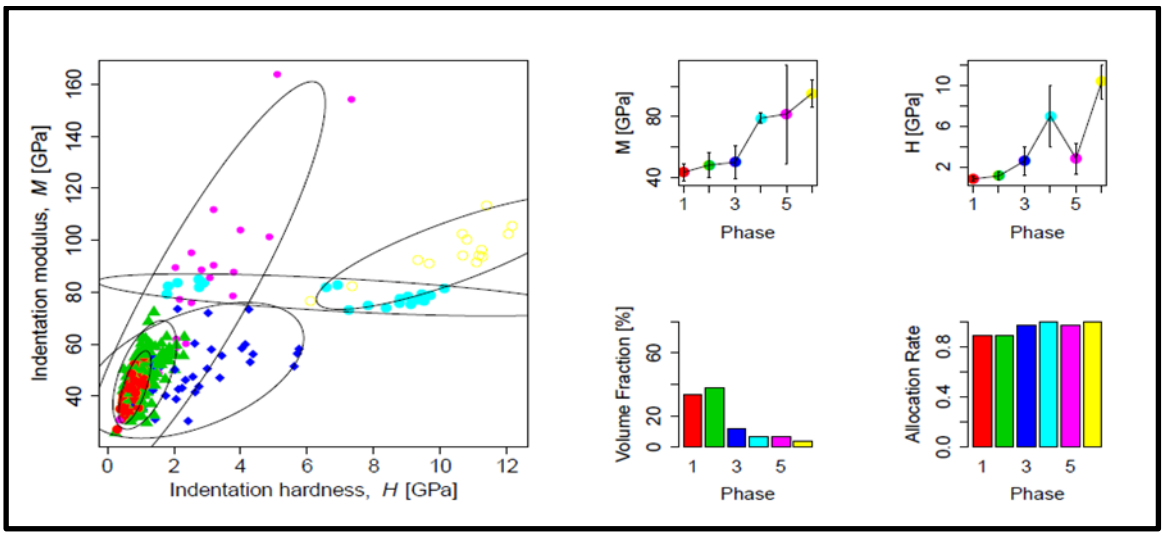

Figure C.6 – Clustering results for X1-70°C; indentation modulus vs. indentation hardness and modulus, hardness, volume fraction, and allocation rate for each phase detected.

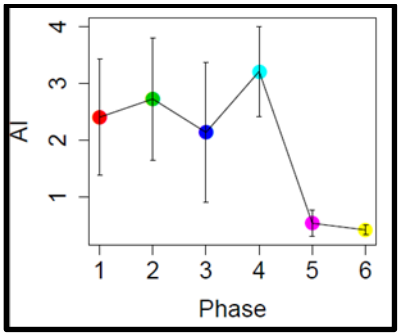

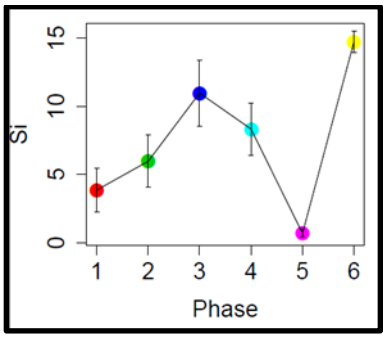

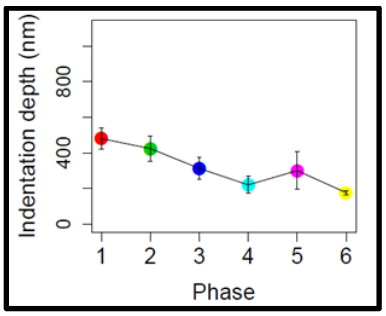

Figure C.7 – Clustering results for aluminum, silicon, and indentation depth at X1-70°C for each phase detected.

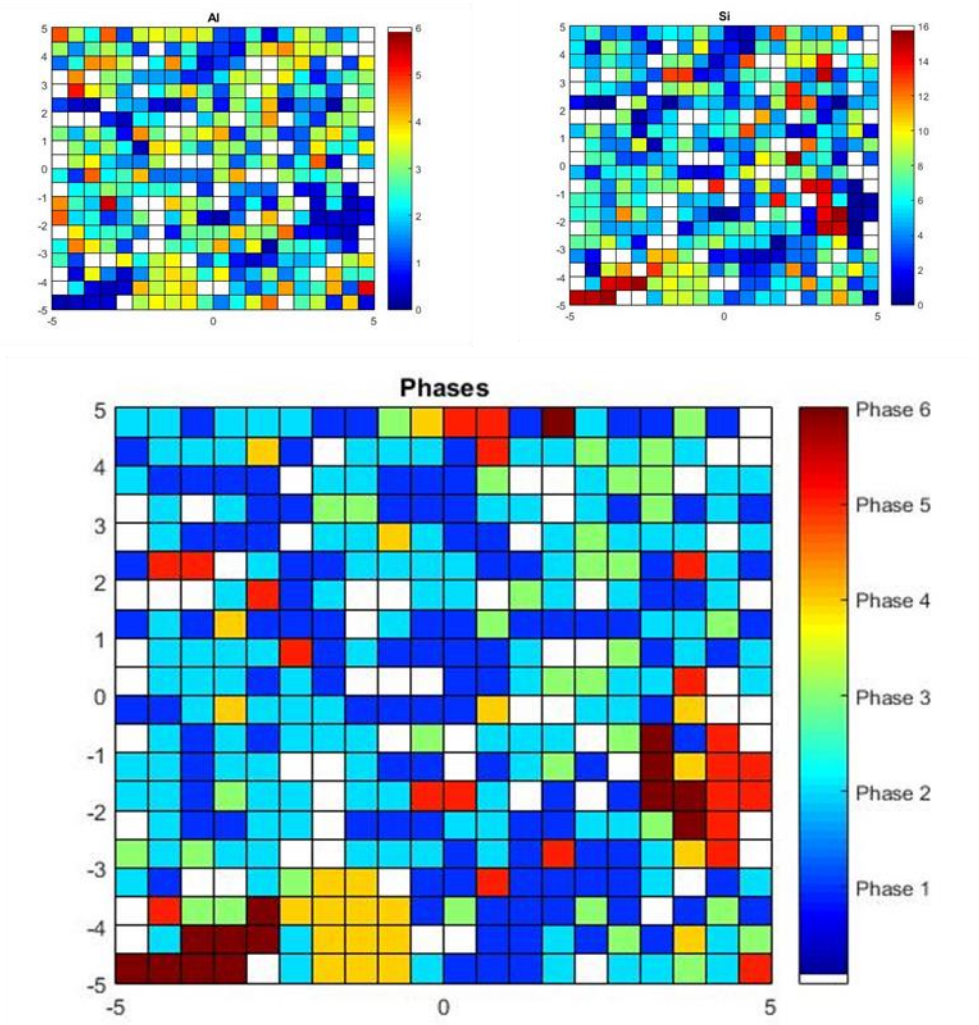

Figure C.8 – Color maps for aluminum, silicon, and indentation depth at X1-70°C for each phase detected.

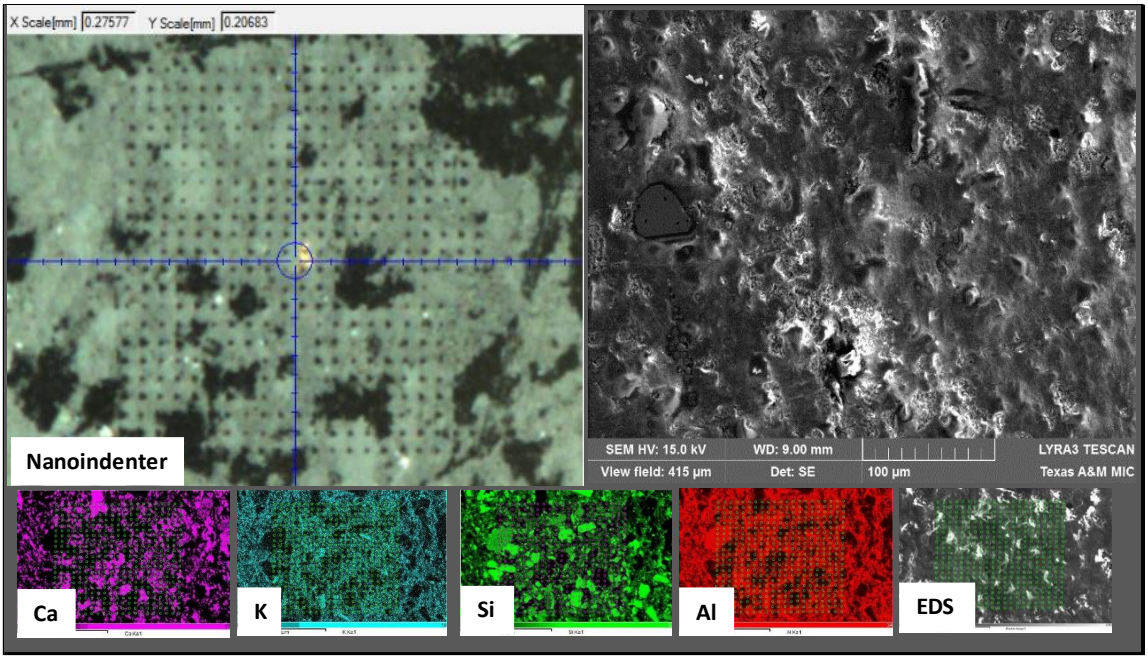

Figure C.9 – Nanoindentation grid and corresponding SEM, Calcium, Potassium, Silicon, Aluminum, and EDX maps for X1-250°C.

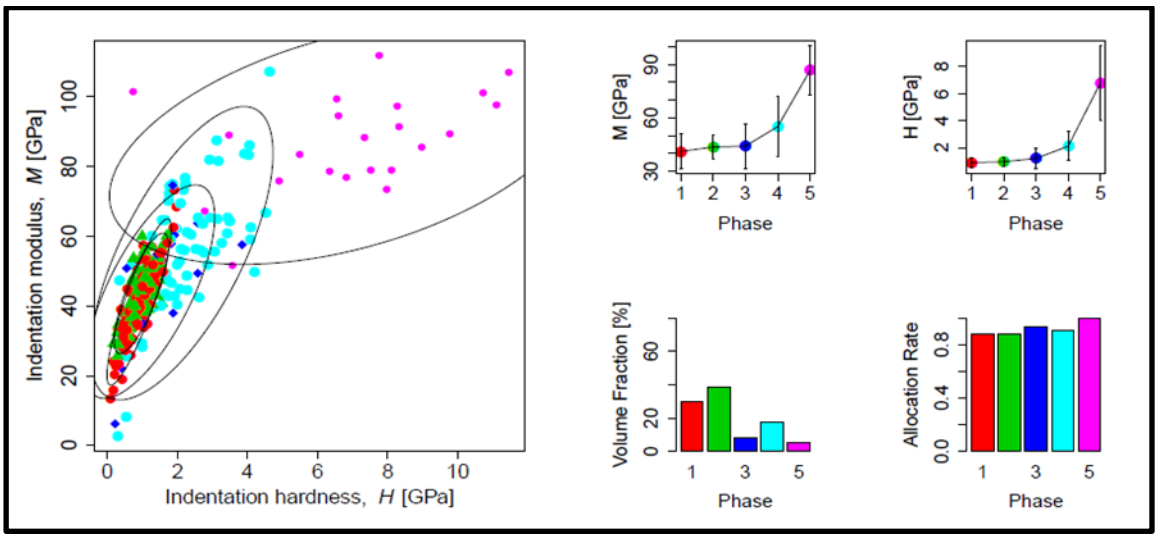

Figure C.10 – Clustering results for X1-250°C; indentation modulus vs. indentation hardness and modulus, hardness, volume fraction, and allocation rate for each phase detected.

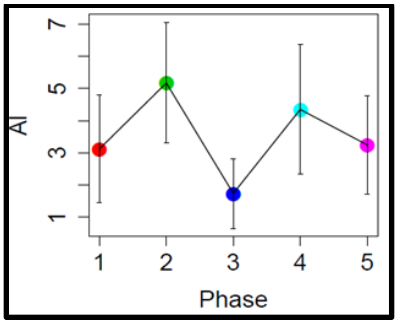

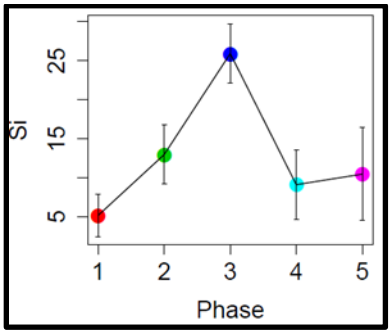

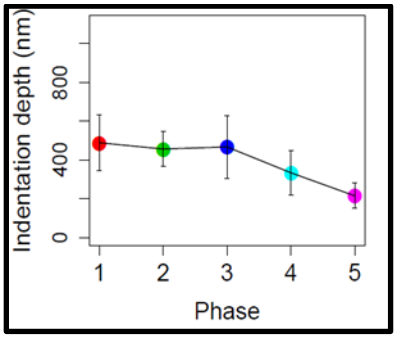

Figure C.11 – Clustering results for aluminum, silicon, and indentation depth at X1-250°C for each phase detected.

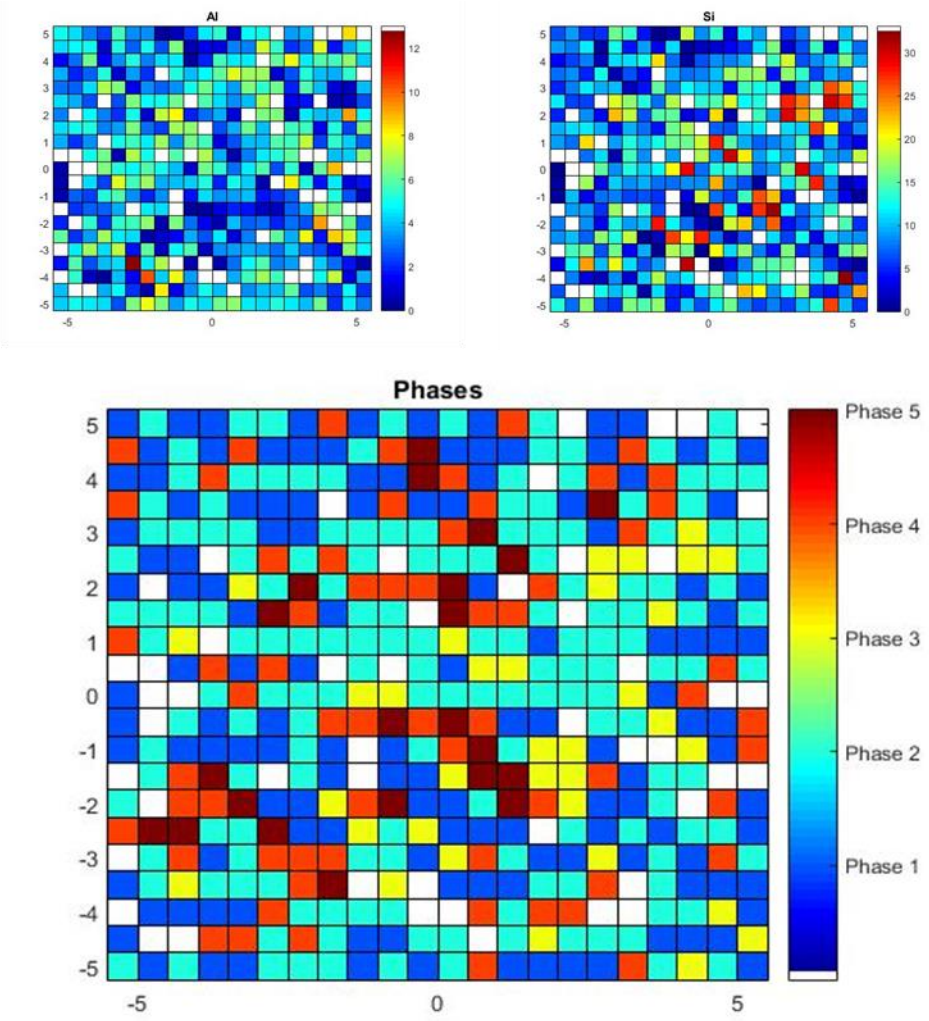

Figure C.12 – Color maps for aluminum, silicon, and indentation depth at X1-250°C for each phase detected.

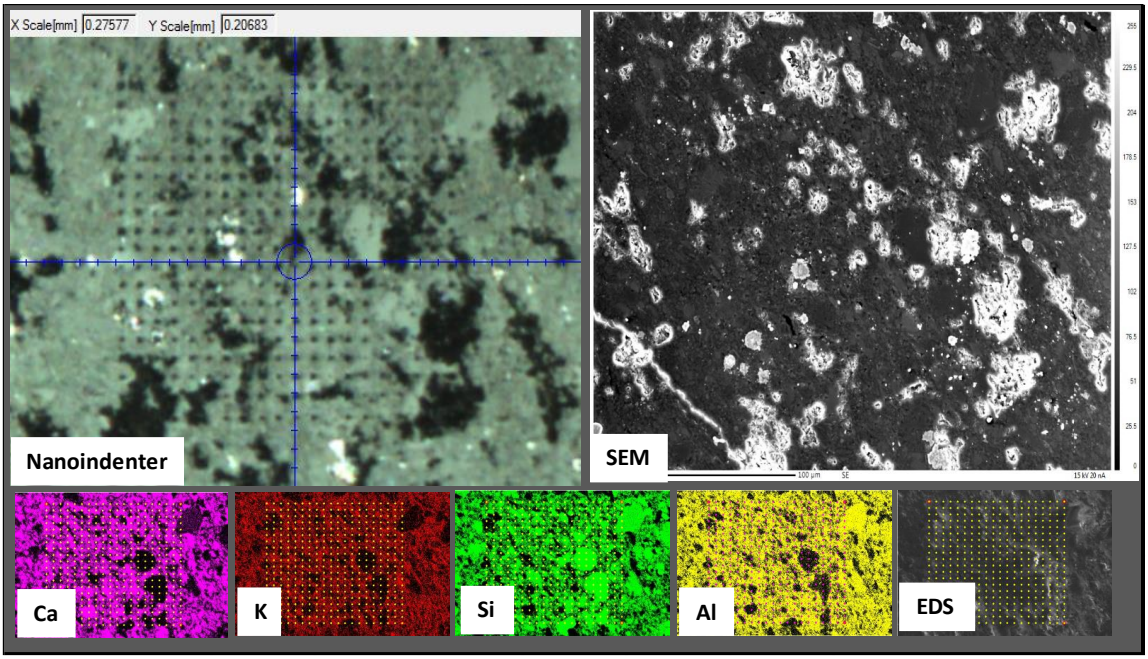

Figure C.13 – Nanoindentation grid and corresponding SEM, Calcium, Potassium, Silicon, Aluminum, and EDX maps for X1-350°C.

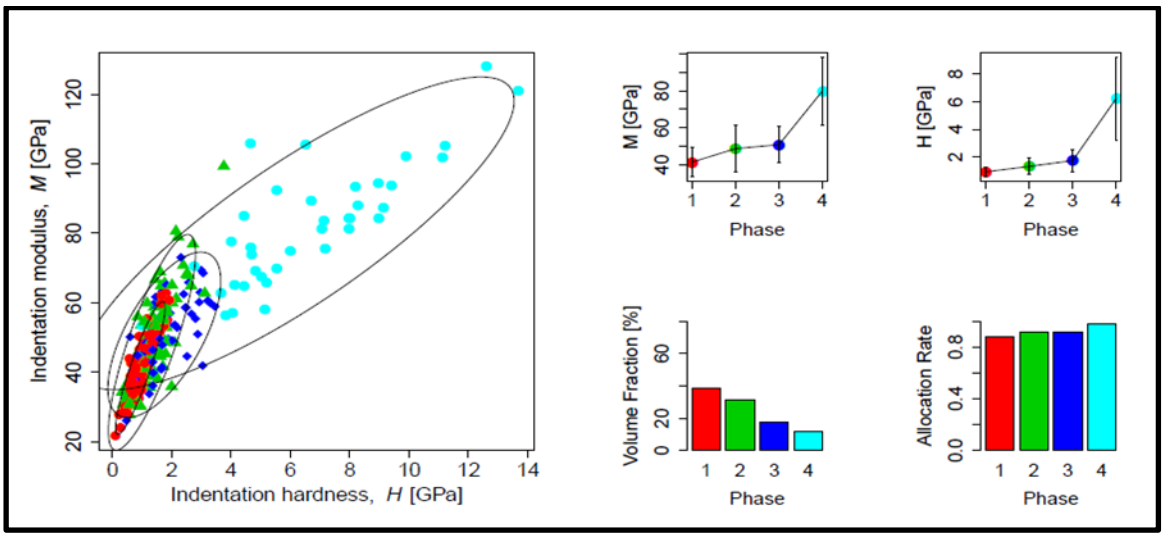

Figure C.14 – Clustering results for X1-350°C; indentation modulus vs. indentation hardness and modulus, hardness, volume fraction, and allocation rate for each phase detected.

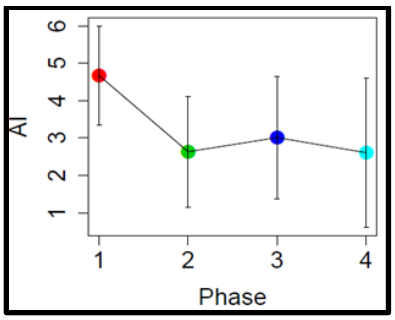

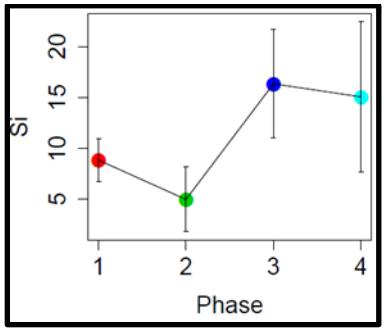

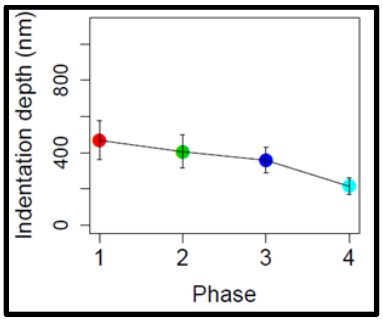

Figure C.15 – Clustering results for aluminum, silicon, and indentation depth at X1-350°C for each phase detected.

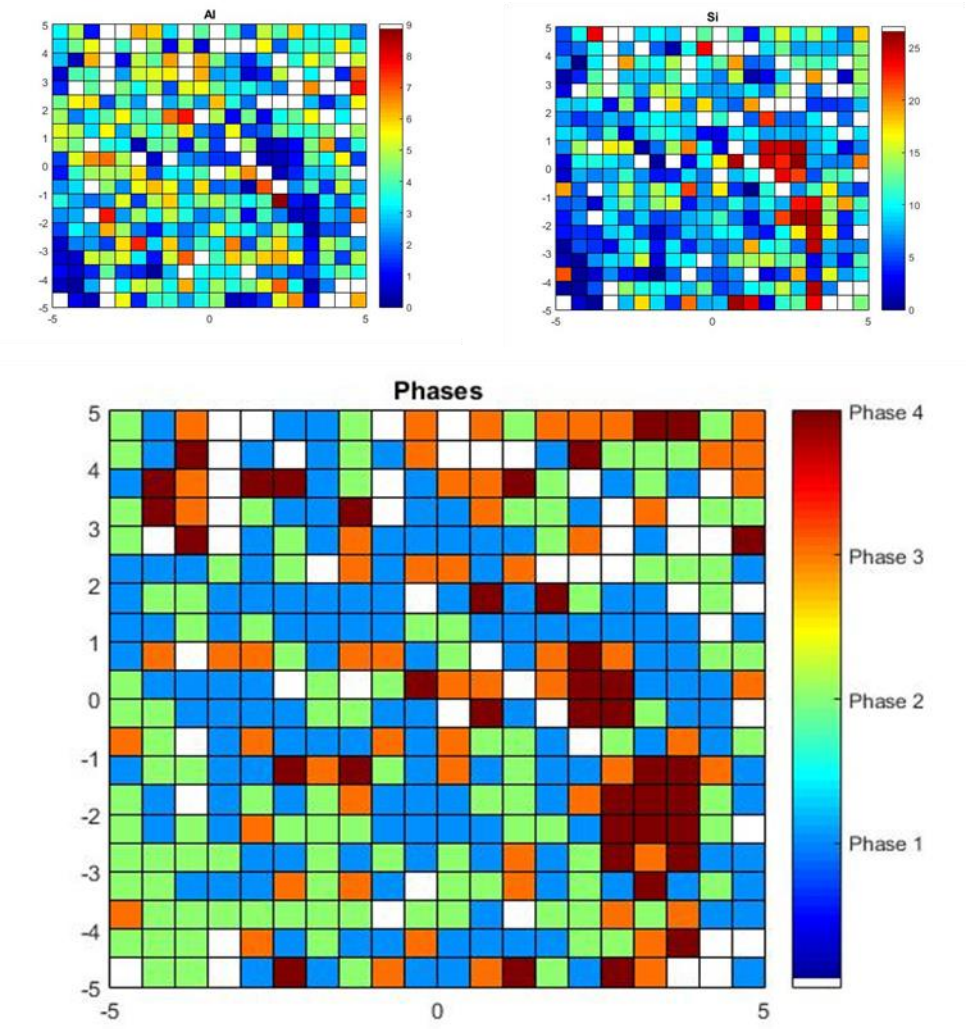

Figure C.16 – Color maps for aluminum, silicon, and indentation depth at X1-350°C for each phase detected.

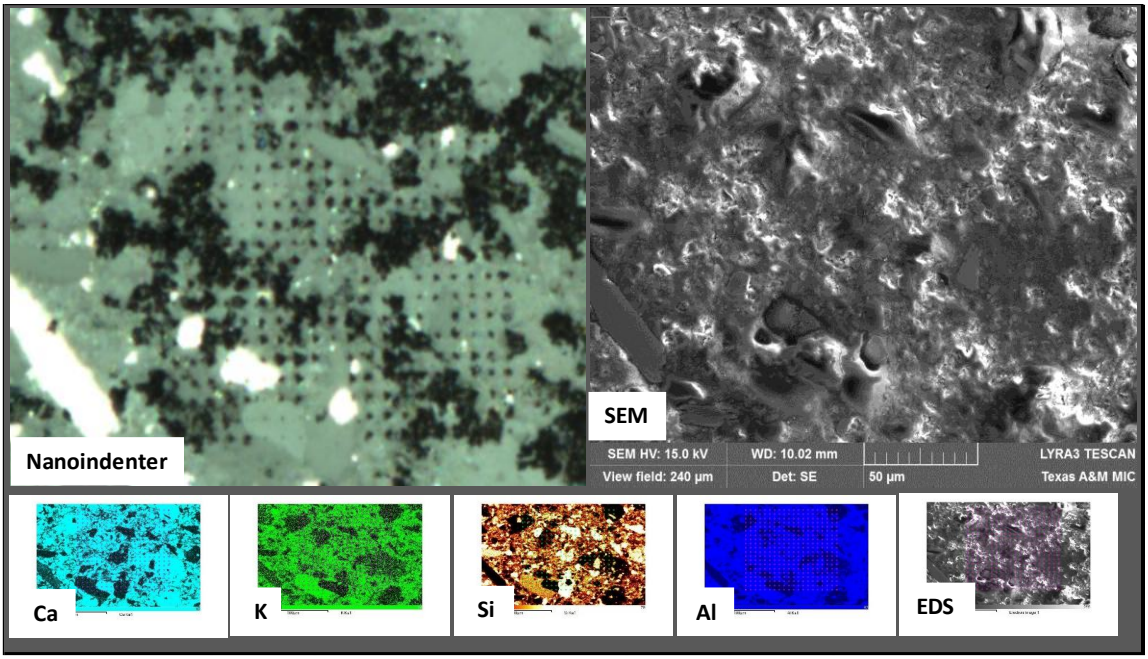

Figure C.17 – Nanoindentation grid and corresponding SEM, Calcium, Potassium, Silicon, Aluminum, and EDX maps for X3-23°C.

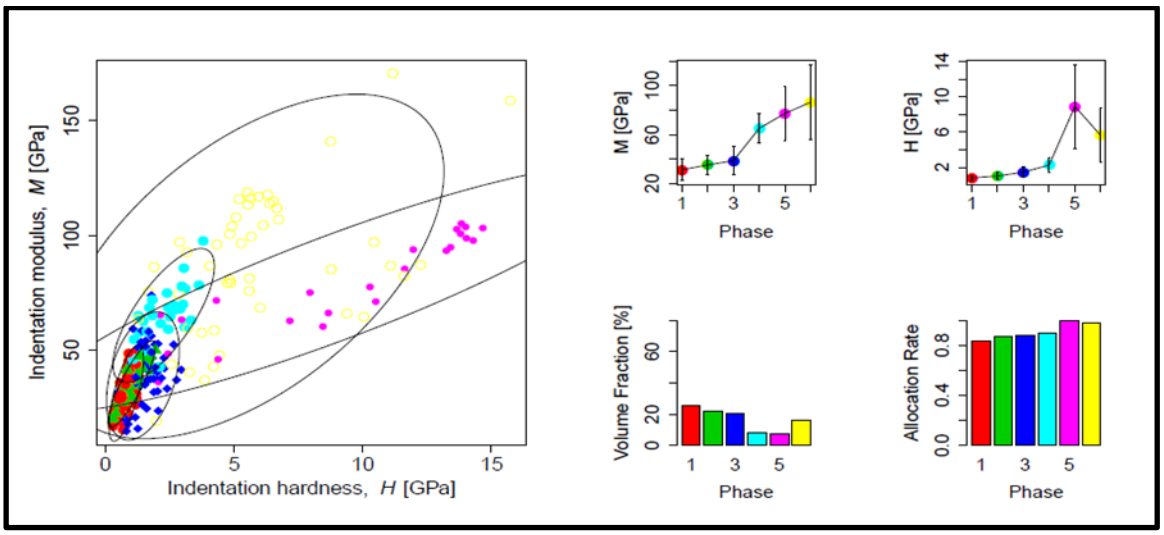

Figure C.18 – Clustering results for X3-23°C; indentation modulus vs. indentation hardness and modulus, hardness, volume fraction, and allocation rate for each phase detected.

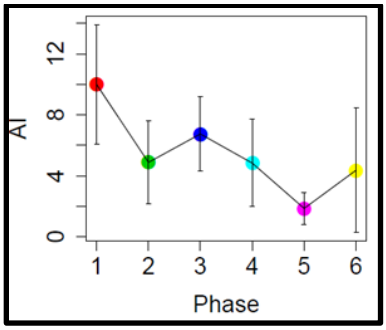

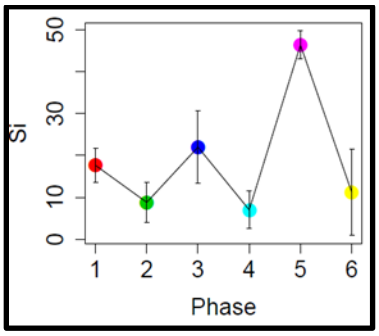

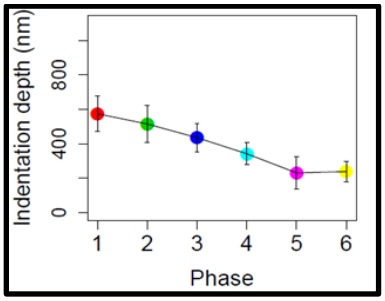

Figure C.19 – Clustering results for aluminum, silicon, and indentation depth at X3-23°C for each phase detected.

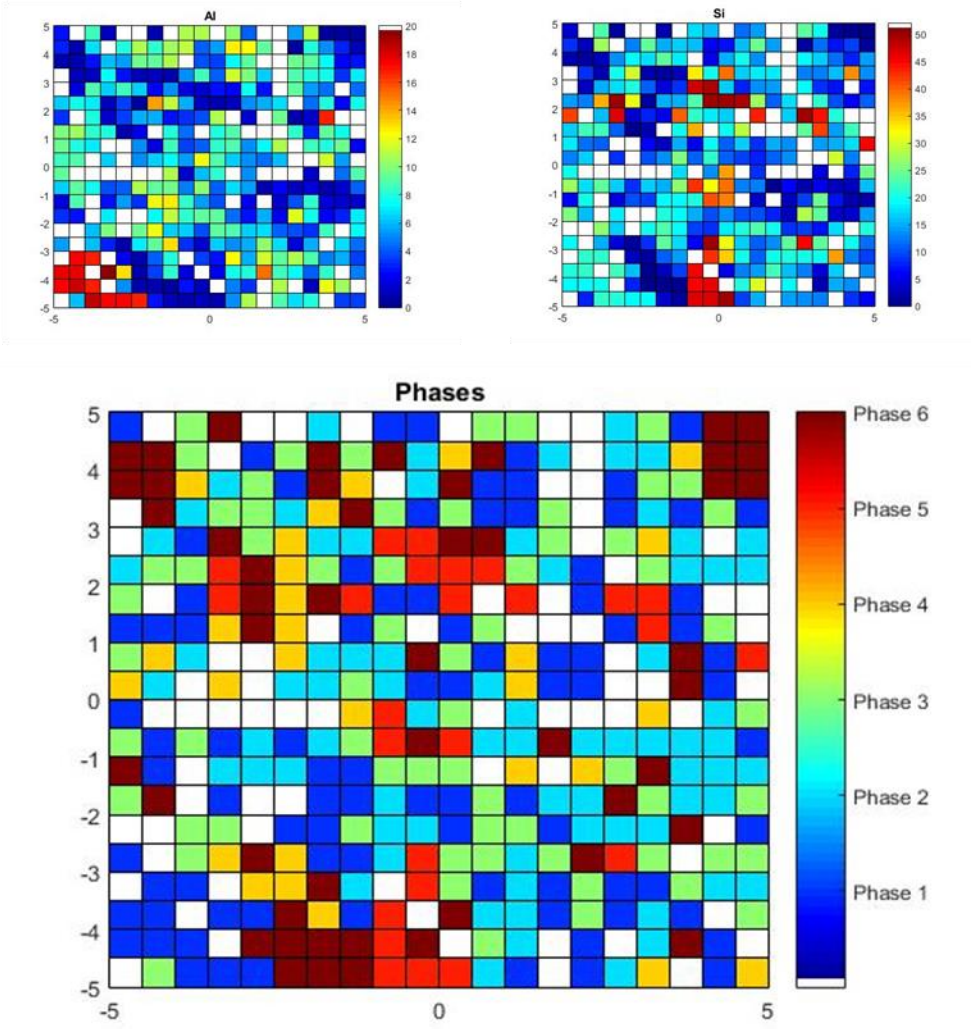

Figure C.20 – Color maps for aluminum, silicon, and indentation depth at X3-23°C for each phase detected.

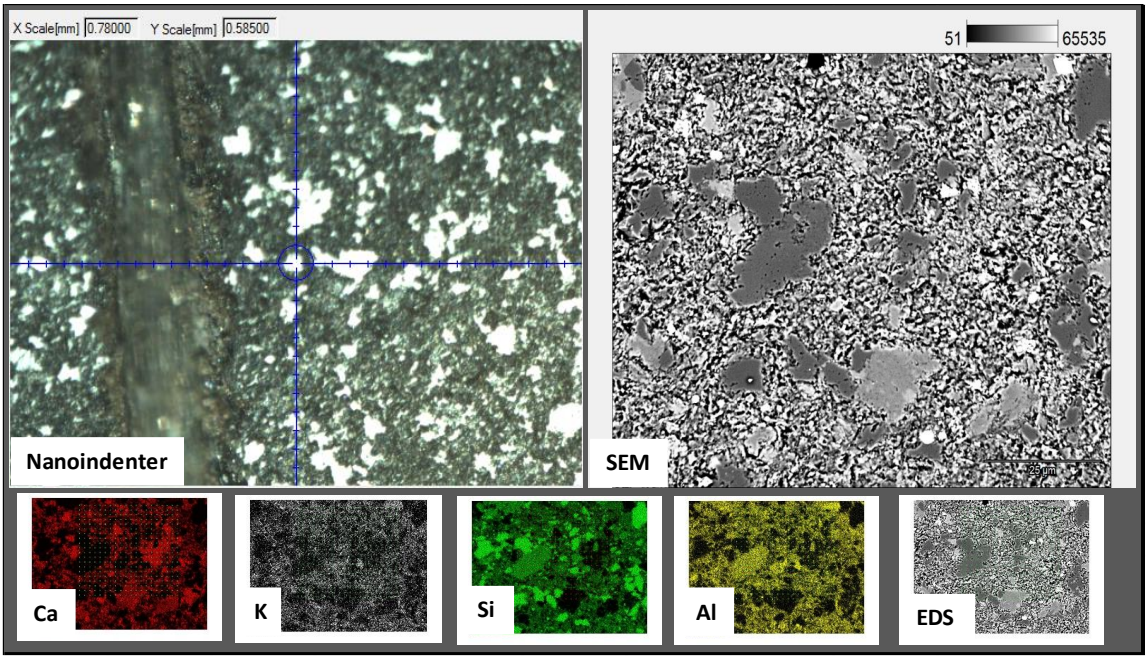

Figure C.21 – Nanoindentation grid and corresponding SEM, Calcium, Potassium, Silicon, Aluminum, and EDX maps for X3-250°C (1).

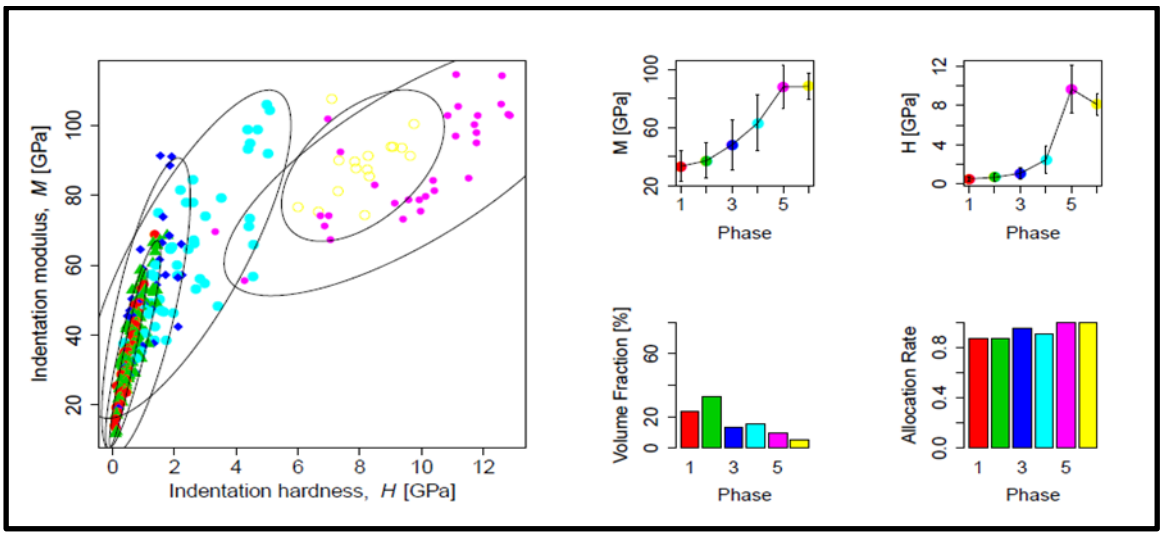

Figure C.22 – Clustering results for X3-250°C (1); indentation modulus vs. indentation hardness and modulus, hardness, volume fraction, and allocation rate for each phase detected.

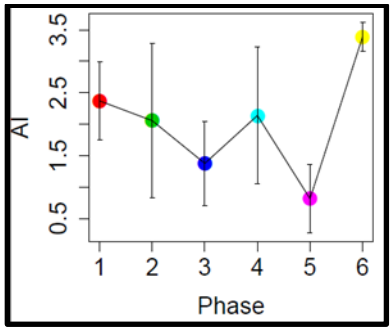

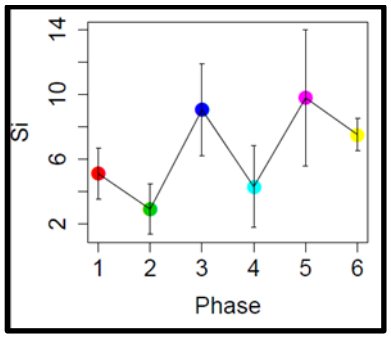

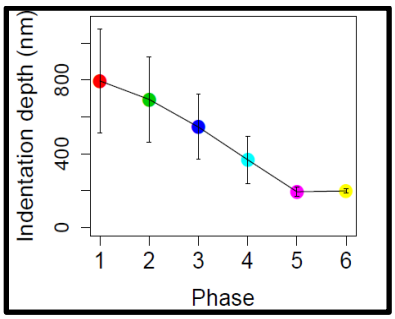

Figure C.23 – Nanoindentation grid and corresponding SEM, Calcium, Potassium, Silicon, Aluminum, and EDS maps for X3-250°C (1).

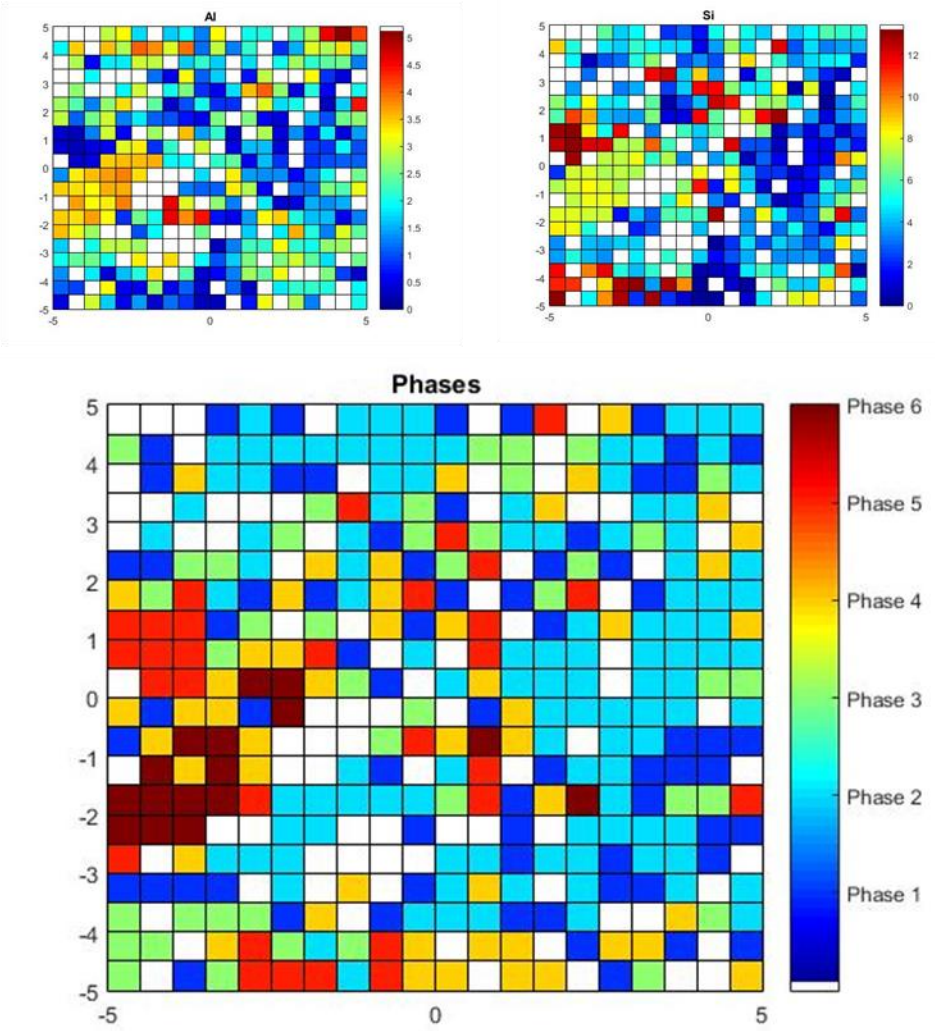

Figure C.24 – Color maps for aluminum, silicon, and indentation depth at X3-250°C (1) for each phase detected.

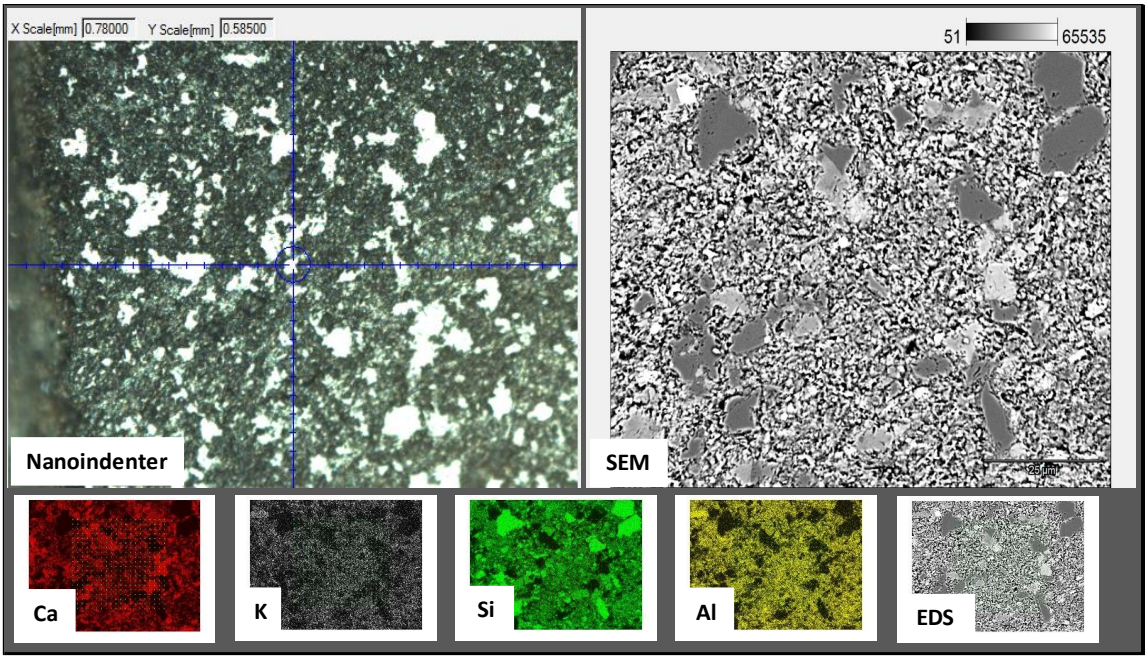

Figure C.25 – Nanoindentation grid and corresponding SEM, Calcium, Potassium, Silicon, Aluminum, and EDX maps for X3-250°C (2).

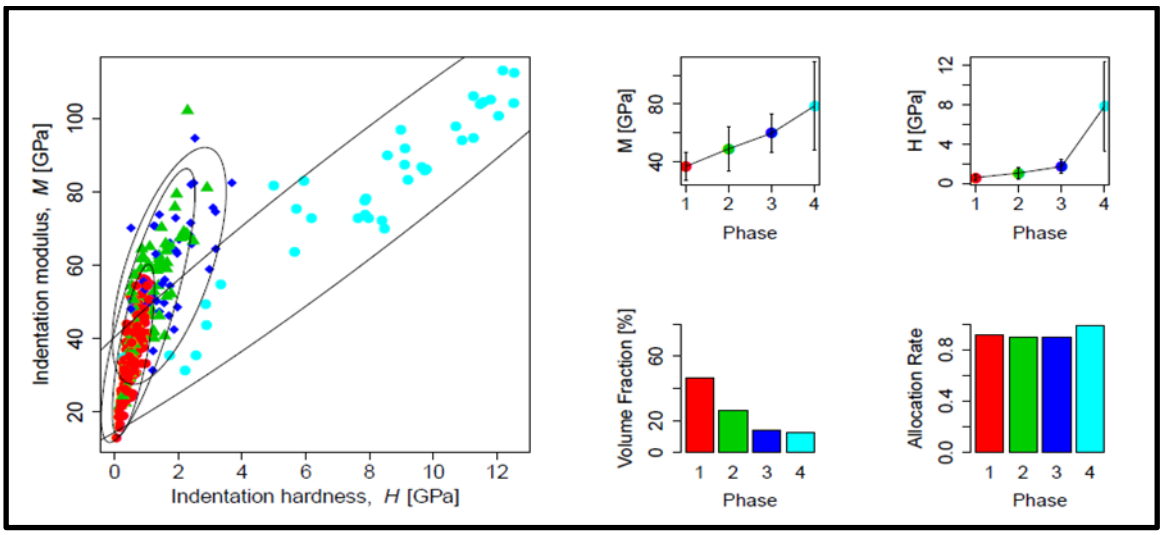

Figure C.26 – Clustering results for X3-250°C (2); indentation modulus vs. indentation hardness and modulus, hardness, volume fraction, and allocation rate for each phase detected.

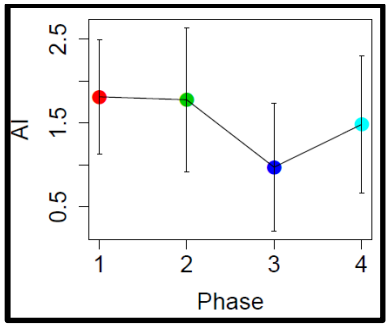

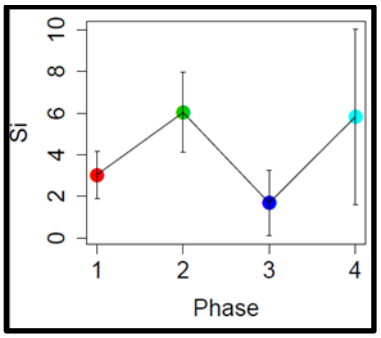

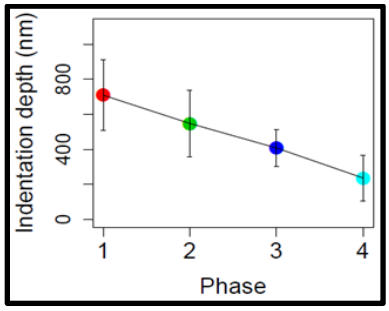

Figure C.27 – Nanoindentation grid and corresponding SEM, Calcium, Potassium, Silicon, Aluminum, and EDS maps for X3-250°C (2).

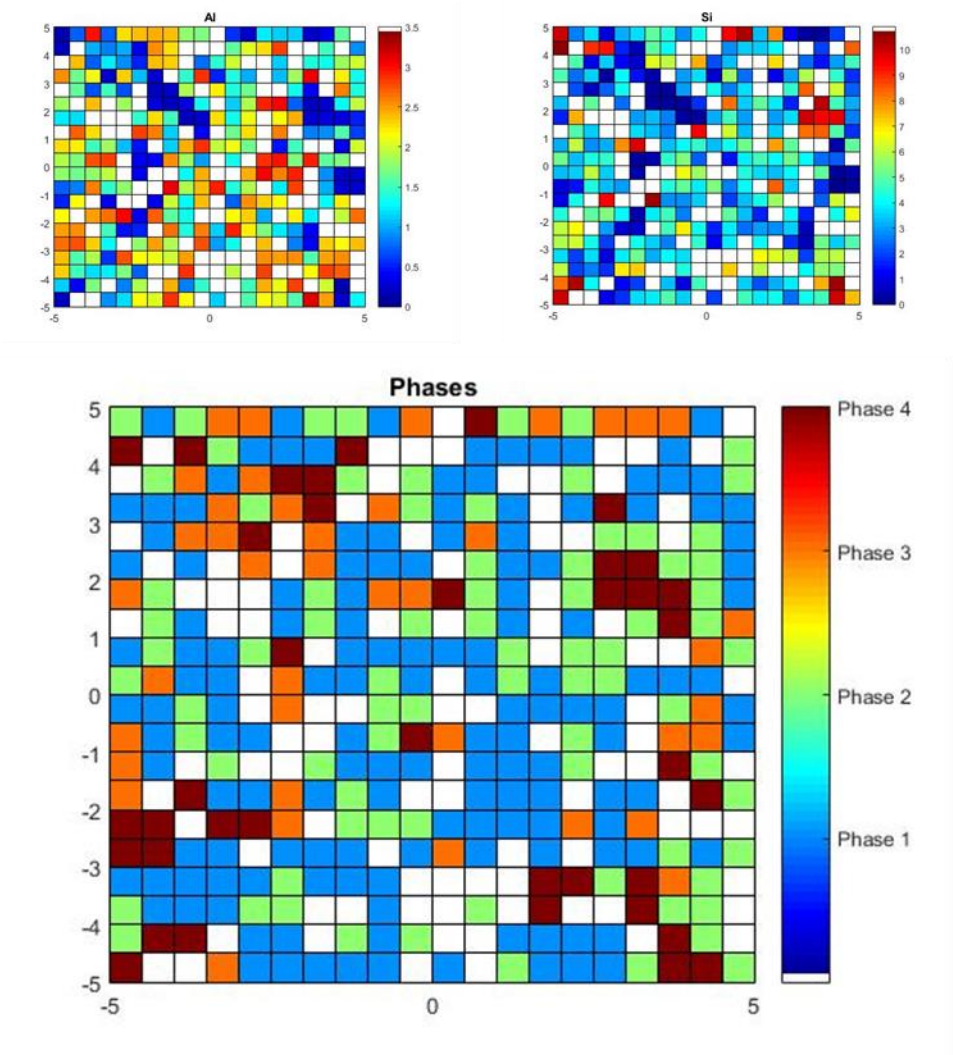

Figure C.28 – Color maps for aluminum, silicon, and indentation depth at X3-250°C (2) for each phase detected.

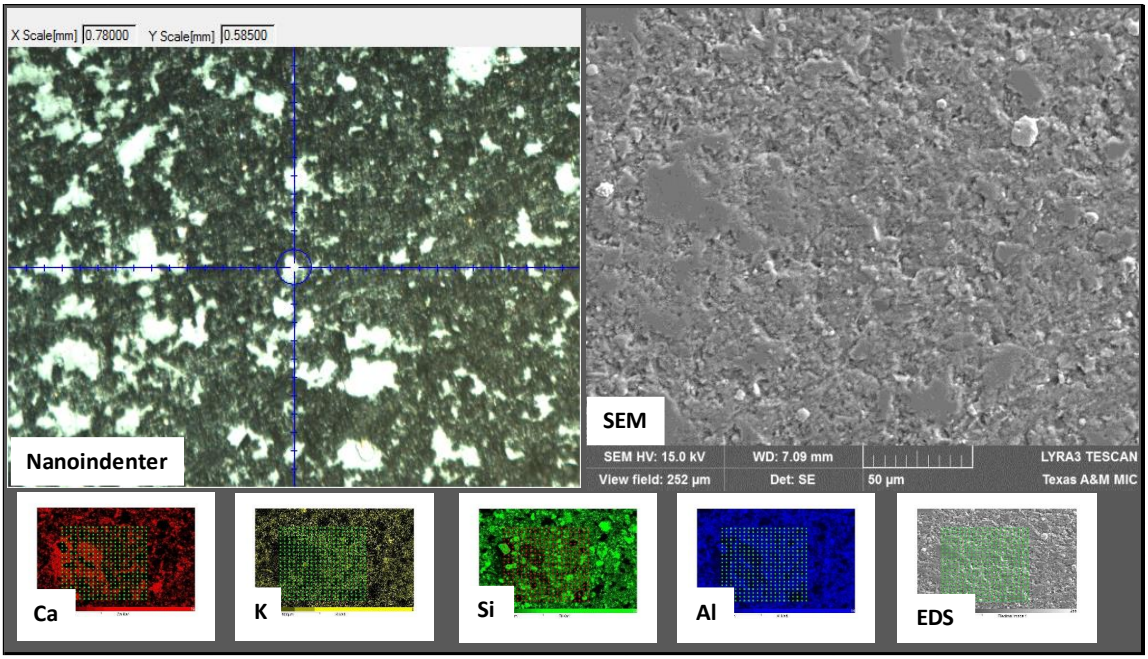

Figure C.29 – Nanoindentation grid and corresponding SEM, Calcium, Potassium, Silicon, Aluminum, and EDX maps for X3-350°C.

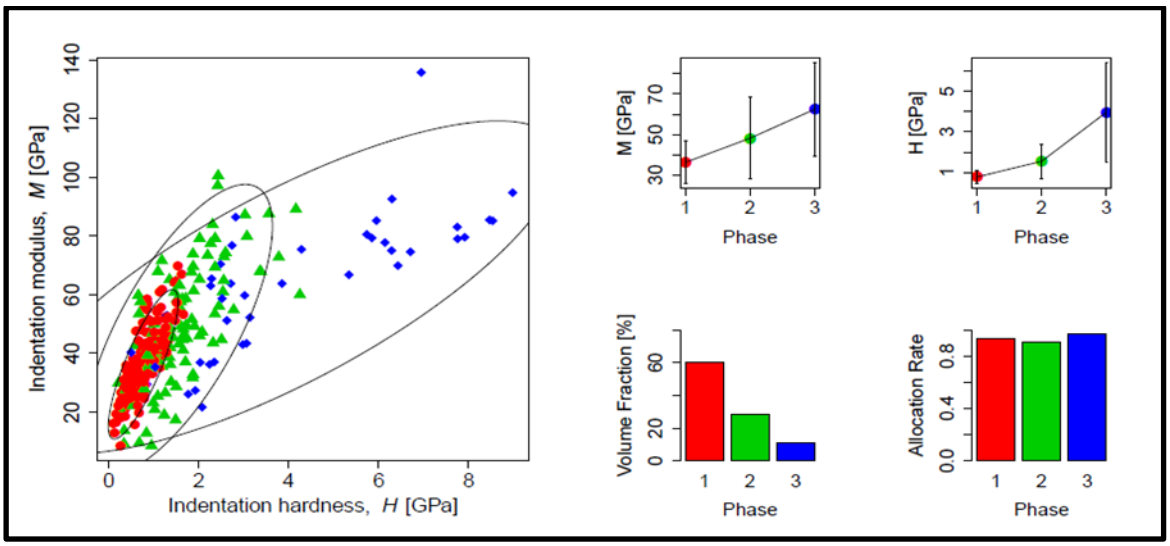

Figure C.30 – Clustering results for X3-350°C; indentation modulus vs. indentation hardness and modulus, hardness, volume fraction, and allocation rate for each phase detected.

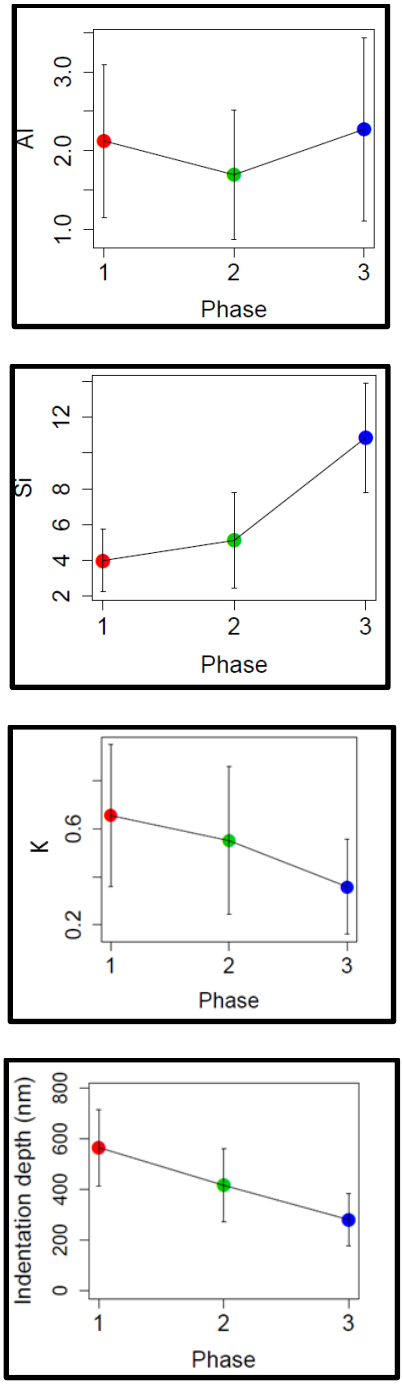

Figure C.31 – Clustering results for aluminum, silicon, potassium and indentation depth at X3-350°C for each phase detected.

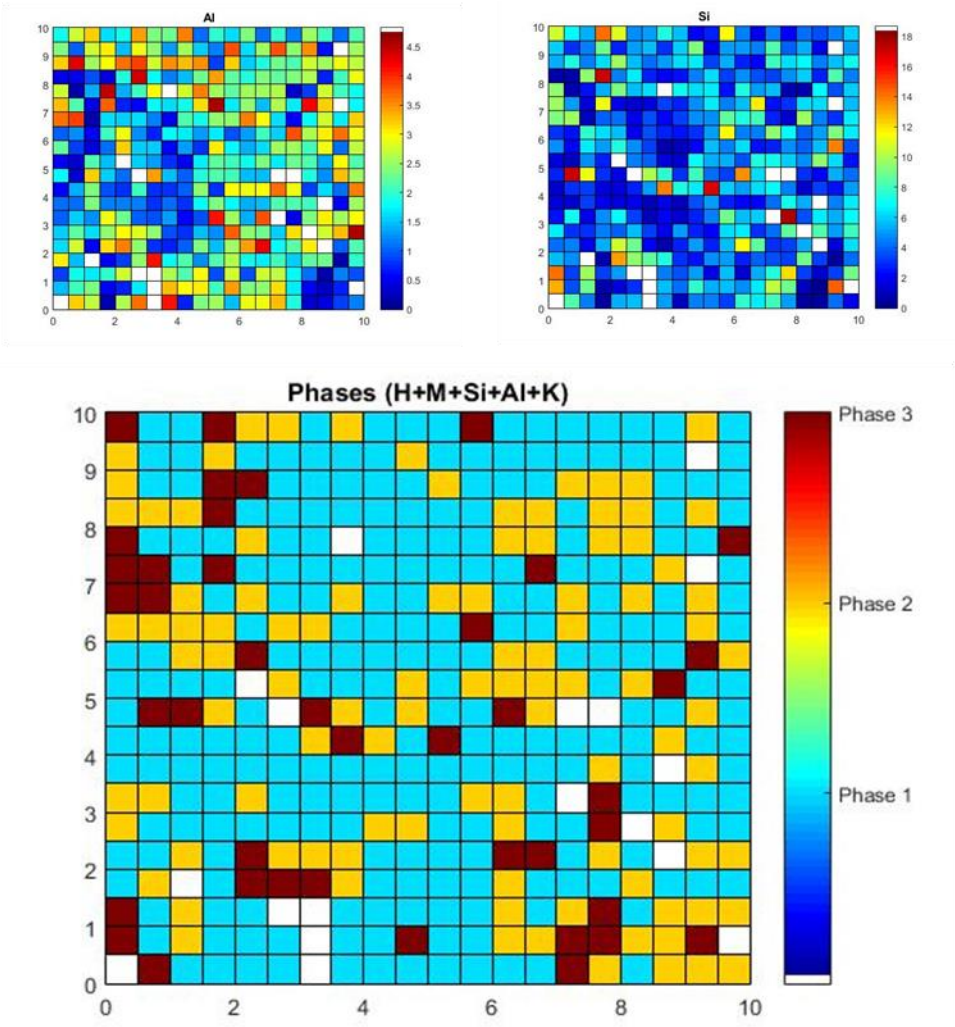

Figure C.32 – Color maps for aluminum, silicon, and indentation depth at X3-350°C for each phase detected.

APPENDIX D

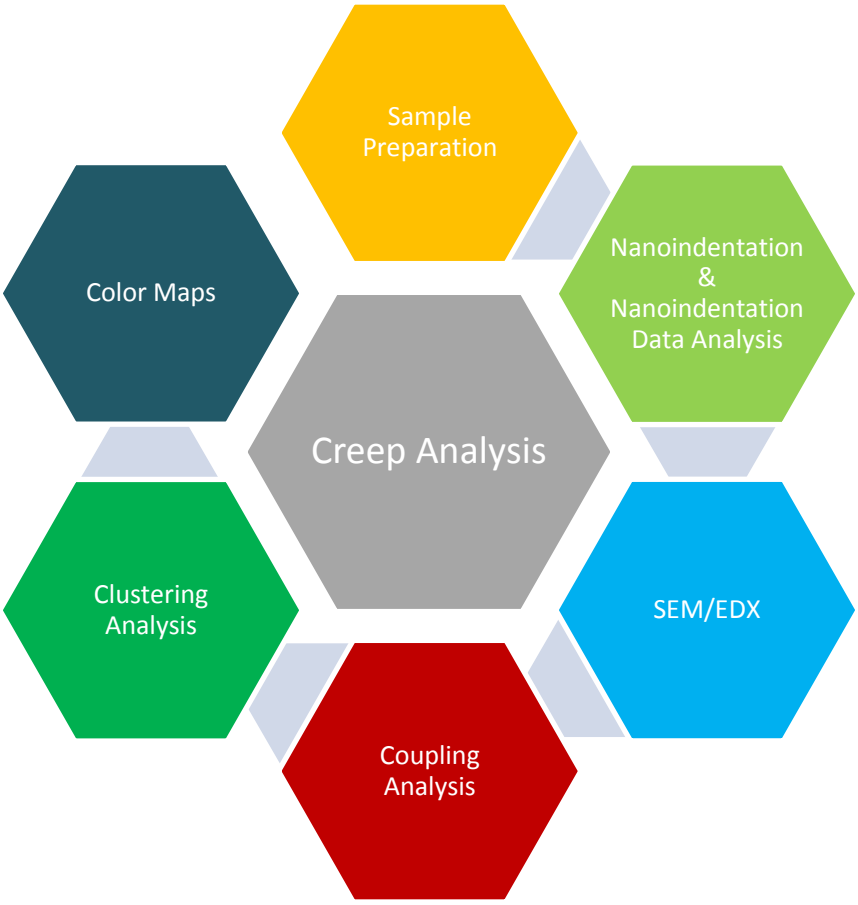

Figure D.1 – Analytical methodology outline to perform creep analysis using nanoindentation and SEM/EDX.

A guide to performing creep experimental analysis is provided below where each stage is explained in detail in the respective sections of this thesis. **Fig. D.1** is provided as an outline on the major stages needed to perform creep analysis using nanoindentation and SEM/EDX.

1. Sample preparation

a. Prepare samples in both the X1 (parallel) and X3 (perpendicular) directions.

b. Perform polishing procedure as listed in **Section 3.1**

2. Nanoindentation and Nanoindentation Data Analysis

a. Perform grid indentations using either a regular Berkovich tip (for room temperature experiments) or a high temperature Berkovich tip (for high temperature experiments)

b. Use the following load settings: 20x20 grid (or larger), 7μm spacing, 4.8mN loading force, loading segment of 10s, holding period of 10s (for normal indentations) and 200s (for creep indentations), and an unloading segment of 10s.

c. Using the reduced modulus, obtained the indentation modulus from **Eq. D.1**:

$$\frac{1}{E_r} = \frac{(1-v^2)}{E} + \frac{(1-{v_i}^2)}{E_i} \tag{D.1}$$

d. Using Matlab, perform a least-squares regression and fit the logarithmic function to the experimental data to obtain the two unknown parameters: characteristic time, τ, and contact creep modulus, C.

$$L(t) - \frac{1}{M} = \frac{\ln(\frac{t}{\tau}+1)}{C} \tag{D.2}$$

3. Scanning Electron Microscope/Energy X-Ray Dispersive Spectroscopy (SEM/EDX)

a. Obtain topographic images of the indented space (15kV/ working distance of 9mm)
b. Obtain elemental maps for Si, Al, Ca, and K until intensity values are high or the element map is easily differentiable
c. Using Matlab, obtain the average intensity around each indentation point (1μm radius) for each elemental map.

4. Clustering Analysis
    a. Using R-programming language and the MCLUST tool, input the mechanical (Modulus, Hardness, and Contact Creep Modulus) and the chemical intensity values (Silicon, Aluminum, and/or Potassium, Calcium) for analysis. The data will be output as different phases.
    b. Using the output results, determine the softest phase present in the sample. This will correspond to the porous clay/kerogen phase which can be determined by ensuring that the ratio between the Si:Al elemental intensities is 2:1.
5. Color maps
    a. Using Matlab with the PCOLOR function, create color maps of the phases outputted from the clustering analysis. Each space will correspond to one indentation point (e.g. 20x20 grid will have a pcolor plot of 400 squares).
    b. Compare the phase variation to the Silicon and Aluminum maps for similarities. A good correlation should exist if the coupling analysis was performed accurately.